

TECHNISCHE UNIVERSITÄT WIEN

DISSERTATION

Metastable effects in chalcogenide thin film photovoltaic devices

*Ausgeführt zum Zwecke des akademischen Grades einer
Doktorin der technischen Wissenschaften*

unter der Leitung von

Ao.Univ.Prof.Dr. Johann SUMMHAMMER

E141 Atominstitut

eingereicht an der Technischen Universität Wien

Fakultät für Physik

von

Sabrina JONES (geb. NOVALIN)

0425705

Müggelstraße 27, 10247 Berlin, Deutschland

Berlin, 12. Mai 2020

Unterschrift



Die approbierte gedruckte Originalversion dieser Dissertation ist an der TU Wien Bibliothek verfügbar.
The approved original version of this doctoral thesis is available in print at TU Wien Bibliothek.

Declaration of Authorship

I, Sabrina JONES, declare that this thesis titled, 'Metastable effects in chalcogenide thin film photovoltaic devices' and the work presented in it are my own. I confirm that:

- This work was done wholly or mainly while in candidature for a research degree at this University.
- Where any part of this thesis has previously been submitted for a degree or any other qualification at this University or any other institution, this has been clearly stated.
- Where I have consulted the published work of others, this is always clearly attributed.
- Where I have quoted from the work of others, the source is always given. With the exception of such quotations, this thesis is entirely my own work.
- I have acknowledged all main sources of help.
- Where the thesis is based on work done by myself jointly with others, I have made clear exactly what was done by others and what I have contributed myself.

Signed:

Date:



Die approbierte gedruckte Originalversion dieser Dissertation ist an der TU Wien Bibliothek verfügbar.
The approved original version of this doctoral thesis is available in print at TU Wien Bibliothek.

“I tore myself away from the safe comfort of certainties through my love for truth - and truth rewarded me.”

Simone de Beauvoir



Die approbierte gedruckte Originalversion dieser Dissertation ist an der TU Wien Bibliothek verfügbar.
The approved original version of this doctoral thesis is available in print at TU Wien Bibliothek.

Abstract

Faculty of Physics

Institute of Atomic and Subatomic Physics

Dissertation Technische Wissenschaften Physik

Metastable effects in chalcogenide thin film photovoltaic devices

by Sabrina JONES

supervised by Ao.Univ.Prof.Dr. Johann SUMMHAMMER

The aim of this thesis is to investigate light induced metastable effects occurring in chalcogenide photovoltaic cells and modules. Testing procedures for precise and reliable characterization of thin film photovoltaic devices have been a challenge for research laboratories, test facilities and manufacturers alike. Especially chalcogenide heterostructure solar cells, like CdTe and Cu(In,Ga)Se₂, exhibit light induced metastable effects by altering electrical parameters based on illumination history. International standards for device characterization do not account for metastable behavior and in literature, there is still ambiguity regarding occurrence and predominant cause of metastable behavior. By conducting light soaking and dark relaxation and consecutive measurements of the *IV* characteristic, metastable behavior at the Cu(In,Ga)Se₂ cell level and for commercial CdTe and Cu(In,Ga)Se₂ modules was examined. In Cu(In,Ga)Se₂ cells, altering metastable behavior could be attributed to varied spectral incident irradiation of white, blue and red light. Furthermore, the impact of the buffer layer material such as CdS, ZnSnO and Zn(O,S) on metastabilities and the influence of the buffer layer thickness could be established. A series of light soaking experiments was made with CdTe and Cu(In,Ga)Se₂ modules varying irradiance levels ranging from 50-1000 W/m^2 and bias states between open circuit and short circuit voltage. Differing metastable responses were observed. Lastly, a proposed testing procedure for module characterization was evaluated with Cu(In,Ga)Se₂ modules and recommendations for future test procedures given.



Die approbierte gedruckte Originalversion dieser Dissertation ist an der TU Wien Bibliothek verfügbar.
The approved original version of this doctoral thesis is available in print at TU Wien Bibliothek.

Abstract

Fakultät für Physik

Atominstytut

Dissertation der technischen Wissenschaften Physik

Metastable effects in chalcogenide thin film photovoltaic devices

von Sabrina JONES

betreut durch Ao.Univ.Prof.Dr. Johann SUMMHAMMER

Ziel dieser Arbeit ist die systematische Untersuchung von Licht induzierten metastabilen Effekten in chalcogeniden Photovoltaik Zellen und Modulen. Heutige Testverfahren zur präzisen und vergleichbaren Charakterisierung bilden Herausforderungen für wissenschaftliche Institute, Prüfeinrichtungen und Hersteller, da speziell die chalcogeniden Heterostrukturen wie CdTe und Cu(In,Ga)Se₂ Solarzellen metastabile Effekte in ihren elektrischen Parametern auf Basis der Beleuchtungshistorie aufweisen. Während internationale Standards für Zell und Modul Charakterisierung metastabile Effekte nicht berücksichtigt, findet man in der Literatur ebenfalls unterschiedliche Aussagen zu Auftreten und hauptsächlichen Ursachen des metastabilen Verhaltens. In dieser Arbeit wurden Cu(In,Ga)Se₂ Zellen sowie kommerzielle CdTe und Cu(In,Ga)Se₂ Module Beleuchtungs- und Dunkelphasen ausgesetzt. So konnte durch wiederholte IV Kennlinien Messungen das metastabile Verhalten bestimmt werden. In Cu(In,Ga)Se₂ Zellen wurde ein Zusammenhang zwischen den Metastabilitäten und der spektralen Verteilung der Beleuchtung aus weißem, blauen und rotem Licht, sowie des Pufferschicht Materials aus CdS, ZnSnO und Zn(O,S) und der Pufferschichtdicke hergestellt. CdTe und Cu(In,Ga)Se₂ Module wiesen unterschiedliches metastabiles Verhalten bei variierender Bestrahlungsstärke zwischen 50-1000 W/m² und Spannungszustand auf. Letztlich wurde ein Testverfahren anhand von Cu(In,Ga)Se₂ Modulen evaluiert und Empfehlungen für zukünftige Verfahren vorgeschlagen.



Die approbierte gedruckte Originalversion dieser Dissertation ist an der TU Wien Bibliothek verfügbar.
The approved original version of this doctoral thesis is available in print at TU Wien Bibliothek.

Acknowledgements

I am deeply thankful to the many people who kept me on the path of persistence in pursuing this work.

My parents and my brother, who kept reminding me of my thesis in all the moments other tasks seemed more important.

My husband Marcus Jones, who repeatedly invented new methods of motivating me to finish writing and staying focused.

My AIT supervisor, mentor and friend Marcus Rennhofer, who guided me through the physics of photovoltaics and always saw value in my work when I needed it.

My wonderfully helpful colleagues at AIT Roman Leidl, Thomas Krametz, Gusztáv Újvári, Karl Berger, Rita Ebner, Shokufeh Zamini, Michael Schwark, Bernhard Kubicek, Theo Dimopoulos and boss Wolfgang Hribernik.

My scientific idols and friends Pedro Salomé, Adam Hultqvist, Johan Lindahl, Piotr Szaniawski and Uwe Zimmermann who not only provided me with device samples, equipment tutorials and invaluable technical advice, but made my time at Uppsala University an unforgettable experience.

My scientific mentors at Uppsala University Marika Edoff and Tobias Törndahl who gave me the wonderful opportunity to join their research team and immerse myself in the depths of CIGS materials.

My thesis advisor Johann Summhammer, who must be one of the most patient people in the world waiting for me to finish my work, always being available and even accommodating to my work schedule, when I started working abroad.



Die approbierte gedruckte Originalversion dieser Dissertation ist an der TU Wien Bibliothek verfügbar.
The approved original version of this doctoral thesis is available in print at TU Wien Bibliothek.

Contents

Declaration of Authorship	iii
Abstract	vii
Acknowledgements	xi
Contents	xii
List of Figures	xvii
List of Tables	xix
Abbreviations	xxi
1 Introduction	1
2 Chalcogenides as Photovoltaic Materials	5
2.1 Basic solar cell concepts	5
2.1.1 p/n-homojunction	6
2.1.2 p/n-heterojunction	8
2.1.3 Electrical characteristics	9
2.1.4 Non-ideal cell mechanisms and losses	12
Recombination	13
Parasitic losses	13
2.2 Chalcogenides	14
2.3 Cu(In,Ga)Se ₂ solar cells	15
2.3.1 Cu(In,Ga)Se ₂ structure and composition	15
Absorber	16
Buffer layer	17
Window layer	17
2.3.2 Band diagram and space charge region	17
2.3.3 Defects	18
2.3.4 Metastabilities	19
Relaxed state	20
Red light effect	21

	Forward bias effect	22
	Blue light effect	23
	White light effect	23
	Reverse bias effect	23
2.3.5	Models for metastabilities	23
	DX center model	23
	Cu-migration model	24
	CdS photodoping model	24
	p+ layer model	25
	Amphoteric defect model	25
2.4	CdTe solar cells	26
2.4.1	CdTe structure and composition	27
	Window layer	28
	Buffer layer	28
	Absorber	29
2.4.2	Defects	29
2.4.3	Metastabilities	30
3	Verifying Metastable Effects	33
3.1	Cell characterization	34
3.1.1	Quantum efficiency	34
3.1.2	Current-voltage measurement	36
3.1.3	JV cell measurement setup	38
3.2	Module characterization according to IEC standards	40
3.2.1	I-V flasher	44
3.2.2	Static solar simulator	45
3.2.3	Electronic load	45
3.3	Record of module metastabilities	45
4	Metastable Effects in Cu(In,Ga)Se₂ Cells	47
	Preparation of samples	47
	Experiment overview	49
4.1	Influence of the buffer layer material	49
4.1.1	CdS, ZnSnO and Zn(O,S) buffer layers in CIGS cells: white light soaking under open circuit conditions	50
4.1.2	CdS, ZnSnO, Zn(O,S) buffer layers in CIGS cells: dark relaxation	51
4.1.3	CdS buffer layer in CIGS cells: white, red and blue light soaking	52
4.1.4	ZnSnO buffer layer in CIGS cells: white, red and blue light soaking	54
4.1.5	Zn(O,S) buffer layer CIGS cells: white, red and blue light soaking	56
4.1.6	CdS buffer layer CIGS cells: white light soaking under different circuit conditions	58
4.1.7	ZnSnO buffer layer CIGS cells: white light soaking under different circuit conditions	60
4.2	Metastability and buffer layer thicknesses	62
4.2.1	ZnSnO buffer layer thickness: white, blue and red light soaking affecting V_{oc}	62
4.2.2	ZnSnO buffer layer thickness: white, blue and red light soaking affecting the FF	65

4.3	CIGS cell reflectance spectroscopy	68
5	Metastable Effects in Modules	71
5.1	Relaxed state	71
5.2	CdTe modules	72
5.2.1	Forward bias treatment	73
5.2.2	CdTe low irradiance light soaking	74
5.2.3	50 W light soaking under different bias conditions	78
5.2.4	1000 W light soaking	80
5.3	CIGS modules	83
5.3.1	CIGS low irradiance light soaking	83
5.4	Comparison with a-Si modules	86
5.4.1	a-Si low irradiance light soaking	87
5.5	Stabilized and reliable CIGS characterization	89
5.5.1	The NREL characterization practice	89
5.5.2	Validation of NREL practice	91
6	Discussion of Results	95
6.1	Impact of bias and light	95
6.2	Impact of irradiance	97
6.3	Impact of illumination wavelength	98
	Red and blue light effect in CIGS	100
6.4	Summary	100
6.5	Implications for the characterization of modules	101
	Temperature	101
	Material composition	101
	Bias pre-treatment	102
	Light soaking pre-treatment	102
6.6	Further research questions	103
A	Experiment Documentation	105
B	Module Data Sheets	115
C	List of Publications	121
	Bibliography	123



Die approbierte gedruckte Originalversion dieser Dissertation ist an der TU Wien Bibliothek verfügbar.
The approved original version of this doctoral thesis is available in print at TU Wien Bibliothek.

List of Figures

1.1	Best research-cell efficiencies according to NREL	2
1.2	Champion module efficiencies according to NREL	2
2.1	p/n homojunction: electric field, potential and band diagram	6
2.2	p/n heterojunction	8
2.3	Solar cell quantum efficiency	10
2.4	JV characteristic	11
2.5	Equivalent circuit with series and shunt resistance	14
2.6	CIGS cell stack.	16
2.7	CIGS unit cell	16
2.8	CIGS band diagram	18
2.9	Kink in light <i>JV</i> curve	20
2.10	CdS photodoping model	25
2.11	CdTe band diagram	27
2.12	CdTe cell stack.	28
2.13	Demarcation energies for defect levels	30
2.14	Roll over and cross over anomalies in <i>JV</i> curves	31
3.1	Current losses in a quantum efficiency diagram	35
3.2	Quantum efficiency setup schematic	36
3.3	<i>JV</i> measurement electric circuit	37
3.4	<i>JV</i> measurement setup for solar cells	37
3.5	Uppsala University <i>JV</i> measurement setup	38
3.6	AIT <i>JV</i> measurement setup	39
3.7	ICVT measurement setup at Uppsala University	40
3.8	LED light source intensity spectrum for ICVT setup	41
3.9	IEC 61646 testing procedure overview	42
3.10	AIT flasher test stand	44
3.11	AIT static sun simulator	44
4.1	SIMS depth profile of CIGS layer	48
4.2	White light soaking for CdS, ZnSnO and Zn(O,S) buffer layer cells	50
4.3	Dark relaxation for CdS, ZnSnO and Zn(O,S) buffer layer cells	51
4.4	CdS cells white, blue and red light soaking	53
4.5	ZnSnO cells white, blue and red light soaking	54
4.6	Zn(O,S) cells white, blue and red light soaking	56
4.7	Zn(O,S) light soaking first 10 minutes	57
4.8	CdS cells light soaking under OC, MPP and SC conditions	58

4.9	ZnSnO cells light soaking under OC, MPP and SC conditions	61
4.10	TEM images of ZnSnO buffer layers.	62
4.11	ZnSnO buffer layer thickness series: V_{oc} behavior under LS	63
4.12	ZnSnO buffer layer thickness series: FF behavior under LS	66
4.13	Reflectance of CIGS cells before and after light soaking	68
5.1	CdTe modules: Electroluminescence images	73
5.2	Short circuit current treatment.	74
5.3	Improvement of CdTe IV characteristics.	75
5.4	CdTe 50W light soaking and dark soaking.	75
5.5	CdTe 50W light soaking further cell parameters.	76
5.6	CdTe light soaking under different bias conditions.	79
5.7	CdTe 1000W light soaking.	81
5.8	CdTe 1000W light soaking further cell parameters.	81
5.9	CIGS modules: Electroluminescence images	84
5.10	CIGS 50W light soaking and dark soaking.	85
5.11	Improvement of CIGS IV characteristics.	85
5.12	CIGS 50W light soaking further cell parameters.	86
5.13	a-Si modules: Electroluminescence images	88
5.14	a-Si 50W light soaking and dark soaking.	89
5.15	Mini-modules characterized according to NREL	92
5.16	Commercial CIGS modules characterized according to NREL	93
6.1	Light soaking dependent on incident energy	97
6.2	Buffer layer band gap in reference to solar spectrum	98
A.1	CIGS cell experiment overview	106
A.2	CdTe module experiment overview	107
A.3	CIGS module experiment overview	108
A.4	a-Si module experiment overview	109
A.5	CIGS test module experiment overview	110
A.6	NREL proposed CIGS measurement procedure, page 1	111
A.7	NREL proposed CIGS measurement procedure, page 2	112
A.8	NREL proposed CIGS measurement procedure, page 3	113
B.1	Data sheet: First Solar CdTe modules, page 1	116
B.2	Data sheet: First Solar CdTe modules, page 2	117
B.3	Data sheet: Würth Solar GeneCIS CIGS modules	118
B.4	Data sheet: Schott a-Si modules, page 1	119
B.5	Data sheet: Schott a-Si modules, page 2	120

List of Tables

2.1	Summary of observed metastable effects in CIGS solar cells	20
4.1	CIGS cell stack and layer thicknesses	48
4.2	Light soaking illumination intervals	49
4.3	Results: CdS, ZnSnO, Zn(O,S), white LS	51
4.4	Results: CdS, ZnSnO, Zn(O,S), dark relaxation	52
4.5	Results: CdS white, blue and red LS	52
4.6	Results: ZnSnO white, blue and red LS	55
4.7	Results: Zn(O,S) white, blue and red LS	57
4.8	Results: CdS cells light soaking under OC, MPP and SC conditions	59
4.9	Results: ZnSnO cells light soaking under OC, MPP and SC conditions	60
4.10	Results: ZnSnO buffer layer series V_{oc} under white, blue and red LS	64
4.11	Results: ZnSnO buffer layer series FF under white, blue and red LS	67
4.12	CdS, ZnSnO, Zn(O,S) white LS compared with reflectance	70
5.1	CdTe module parameters	72
5.2	Results: CdTe module under low irradiance light soaking	77
5.3	Results: CdTe light soaking under different bias conditions	79
5.4	Results: CdTe 1000W light soaking	82
5.5	CIGS module parameters	83
5.6	Results: CIGS module under low irradiance light soaking	87
5.7	a-Si module parameters	88
5.8	Results: a-Si module under low irradiance light soaking	90
5.9	Mini-module NREL tests	91
5.10	Commercial CIGS module NREL tests	92
6.1	Comparison of metastable CIGS behavior	99



Die approbierte gedruckte Originalversion dieser Dissertation ist an der TU Wien Bibliothek verfügbar.
The approved original version of this doctoral thesis is available in print at TU Wien Bibliothek.

Abbreviations

a-Si	amorphous Silicon
AIT	Austrian Institute of Technology
ALD	atomic layer deposition
CBD	chemical bath deposition
CBO	conduction band offset
CIGS	Copper Indium Gallium di-Selenide
CT	capacitance-temperature profiling
CVD	chemical vapor deposition
CV	capacitance-voltage profiling
DLTS	deep level transient spectroscopy
FF	fill factor
FLP	Fermi level pinning
HRW	high resistance window
IEA	International Energy Agency
IEC	International Electrotechnical Commission
LRW	low resistance window
mpp	maximum power point
NREL	National Renewable Energy Laboratory
oc	open circuit
PV	photovoltaic
sc	short circuit
SCR	space charge region
STC	standard test conditions



Die approbierte gedruckte Originalversion dieser Dissertation ist an der TU Wien Bibliothek verfügbar.
The approved original version of this doctoral thesis is available in print at TU Wien Bibliothek.

*Dedicated to my parents Senad and Patricia, for a childhood full of
curiosity and learning.*



Die approbierte gedruckte Originalversion dieser Dissertation ist an der TU Wien Bibliothek verfügbar.
The approved original version of this doctoral thesis is available in print at TU Wien Bibliothek.

Chapter 1

Introduction

With the rise of photovoltaics as a significant source for the global electrical energy hunger, a competition among different technologies for providing the necessary materials emerged. In this fast paced race, new technologies pop up and records are broken every year. At the beginning of this work, in 2010, the predominant technologies of monocrystalline and polycrystalline silicon solar cells have been resting at 25.0% and 20.4% efficiency respectively, for several years. The so-called second generation thin film technologies amorphous silicon, CdTe and Cu(In,Ga)Se₂ (CIGS) showed record efficiencies of 12.5%, 16.7% and 20.0% respectively.

By 2020, silicon HIT cells have reached 26.7%, monocrystalline silicon cells 26.1% and polycrystalline cells 23.3% efficiency. At the same time, CdTe cells have caught up to 22.1%, while CIGS have slightly surpassed polycrystalline Si and stand at 23.4% efficiency.

Aside from the efficiency race, other factors were driving the anticipated spread of thin film technologies. Manufacturing processes for thin film modules are fundamentally different from crystalline silicon cell production, which relies heavily on the energy intensive Si ingot and wafer production. Film deposition methods can be realized much faster and cheaper, potentially even in roll-to-roll processes. This spurred expectations about thin film technologies gaining significant market shares in the solar industry.

In 2010, the share of thin film technologies in the global annual production was around 13%.

In 2017, the annual production share amounted to 4.5%. [1]

What are the reasons, thin film technologies have not taken over the solar industry? For one reason, the average selling price of silicon wafers declined by almost 50% from 2007 to 2017 [2]. At the same time, controlling the process for large surface deposition turned out to be a challenge for thin film solar manufacturing. To date, the gap between record cell efficiencies and record module efficiencies is still larger for thin film

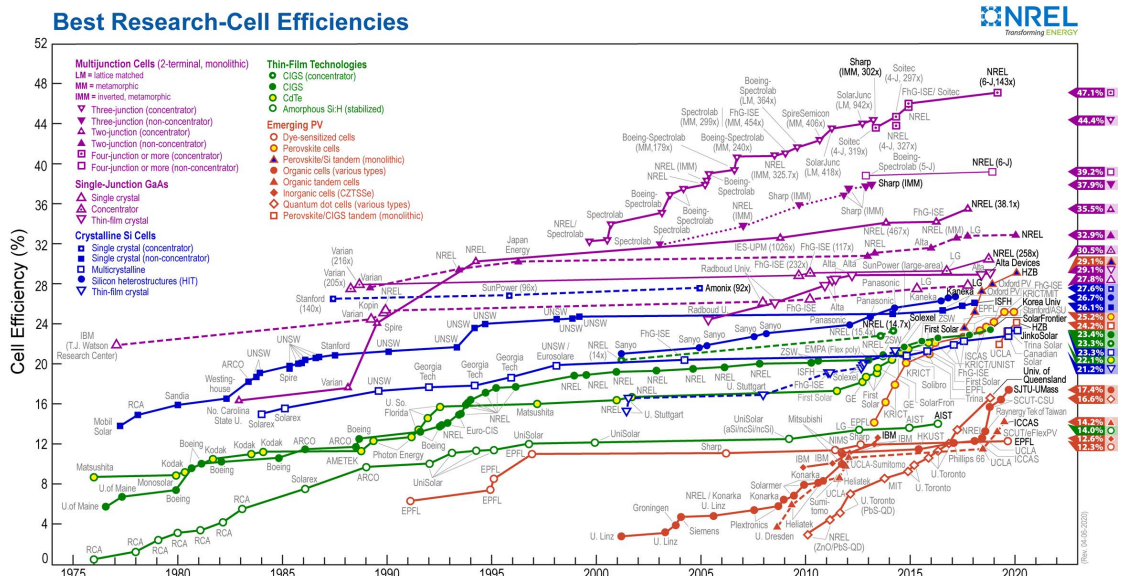


FIGURE 1.1: Best research cell efficiencies according to NREL, 2020. [3]

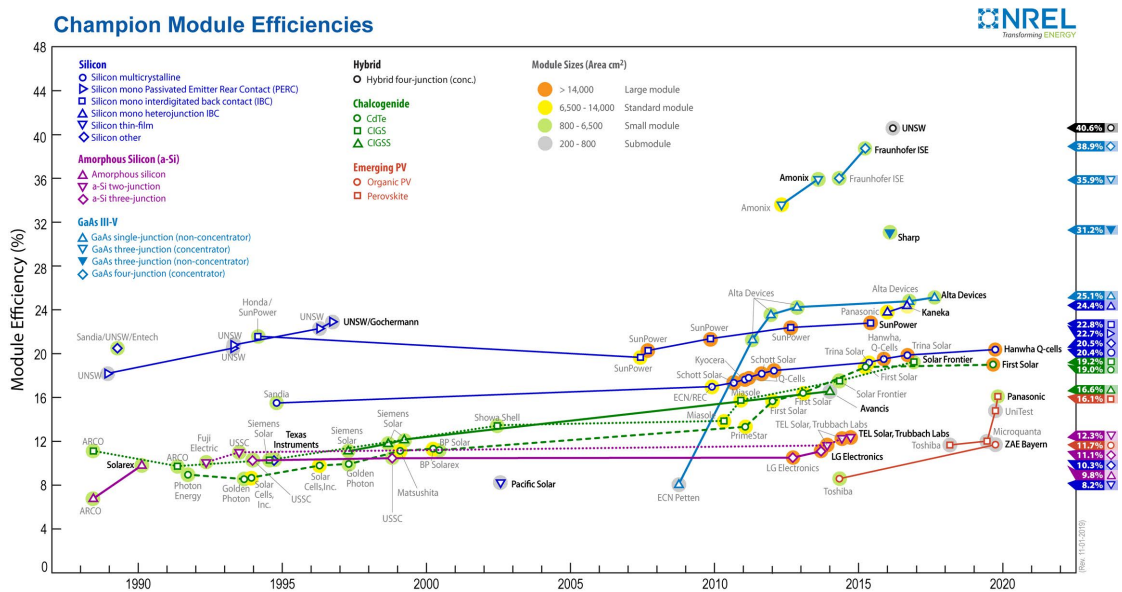


FIGURE 1.2: Champion module efficiencies according to NREL, 2019. [4]

chalcogenide technologies compared with silicon cell technologies, which can be extracted from figures 1.1 and 1.2. While silicon based solar technologies build on theoretically understood ab initio models and over 50 years of semiconductor industry experiences, chalcogenide semiconductor heterostructures like CdTe and CIGS have a lot less research legacy. More complex material compositions, thin layers down to several nanometers and structures prone to defects result in many effects, which are still not fully understood yet.

One class of these effects are called light induced metastabilities, which have primarily been observed in chalcogenide photovoltaic cells and modules. The term metastable was

coined for a number of effects, which show electrically improved or deteriorated parameters after light exposure. Metastable also means, that these effects are not permanent, but typically reverse, after a certain time of relaxation in the dark.

Because metastabilities change the electrical parameters of a photovoltaic device, once it is exposed to light, this poses a challenge for accurate and reliable device characterization. Currently, international standards for photovoltaic device characterization do not take into account metastabilities of chalcogenide PV devices. This has led to significant differences in electrical parameters determined in various round-robin tests for commercial modules among certified testing facilities. It is necessary to define a reliable and accurate yet practical test procedure for characterization of thin film devices.

In this work, metastabilities at the cell level and at the module level are examined. Heuristic metastability observations at the module level are put in context of observations at the cell level, which allow for more detailed characterization techniques and experiments.

This work aims at providing some guiding principles towards a sensible test procedure with regards to metastable effects in chalcogenide devices.

In chapter 2, the fundamentals of chalcogenides as heterostructures for photovoltaic devices and the current theoretical understanding of metastable effects in these photovoltaic materials are established. Chapter 3 describes the experimental methods behind verification of metastabilities of this work. In chapter 4, experimental results showing metastable behavior in $\text{Cu}(\text{In,Ga})\text{Se}_2$ cells are documented. Most of these experiments were conducted at the Ångström Solar Center of the Uppsala University in Sweden. In addition to metastable effects observed in cells, chapter 5 shows, how metastabilities are expressed in CdTe , $\text{Cu}(\text{In,Ga})\text{Se}_2$ and in comparison also in amorphous silicon commercial modules. At the end of the chapter, a proposed testing routine by the National Renewable Energy Laboratory is validated. Results and a future outlook are discussed in chapter 6.



Die approbierte gedruckte Originalversion dieser Dissertation ist an der TU Wien Bibliothek verfügbar.
The approved original version of this doctoral thesis is available in print at TU Wien Bibliothek.

Chapter 2

Chalcogenides as Photovoltaic Materials

This chapter establishes the theory behind copper indium gallium selenide (Cu(In,Ga)Se_2) and cadmium telluride (CdTe) photovoltaic materials. First, fundamental solar cell concepts are discussed starting from ideal cells and leading to chalcogenide relevant heterojunction concepts. After establishing general electrical characteristics for solar cells, details about chalcogenide solar cells are elaborated. The basic crystal structures, material compositions and characteristics as well as the photovoltaic device layout are discussed for each of the two materials Cu(In,Ga)Se_2 and CdTe . In order to understand mechanisms behind metastable effects, material defects and band diagrams will be examined. Based on this fundamental knowledge current theories about metastabilities in chalcogenides will be discussed.

Additionally, insights are given into testing and characterization methods, which are currently standardized by the IEC. Problems and consequences due to the inadequacy of certain procedures are pointed out.

2.1 Basic solar cell concepts

Solar cells transform photon energy into electrical energy by utilizing material characteristics of semiconductor diodes. An essential way to describe the electronic mechanisms in solar cells is to consider the band diagram model.

2.1.1 p/n-homojunction

Due to the spatial inhomogeneity of charge carriers in a system of two semiconductors with different doping agents, the electron (and hole) gradient dn/dx (dp/dx) across the junction leads to a diffusion current. The diffusion current can also be interpreted as a result from the difference in chemical potentials of these two semiconductor regions. Electrons (holes) diffuse into the p (n) region leading to a negative (positive) charge in the p (n) region leaving behind ionized donor and acceptor impurities which create an electric potential and field, and in consequence cause a drift current (figure 2.1(a)). The resulting distribution of charges in the area is expressed in the name space charge region (SCR) or depletion region. The space charge region $-x_p < x < x_n$ is an insulating region empty of mobile charge carriers and with a high electric field.

In thermodynamic equilibrium with no remaining gradient in electrochemical potential, the net electron current is zero and is described by

$$q n \mu_n \mathbf{E} = q D_n \frac{dn}{dx} \quad (2.1)$$

where the electron mobility and diffusion constant are denoted by μ_n and D_n respectively (equivalent for holes). Because the Fermi level is defined as the total electrochemical

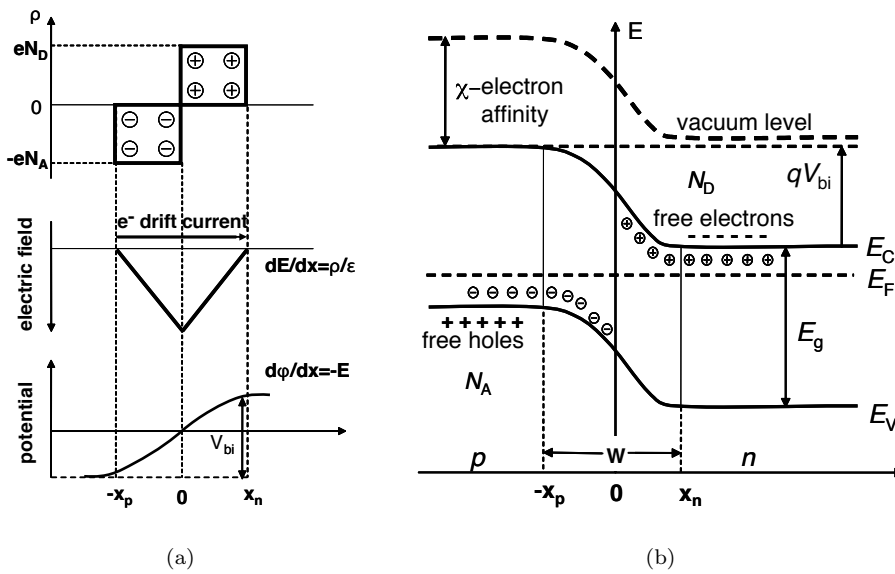


FIGURE 2.1: The charge density distribution created by diffusion results in a linear electric field across the p/n junction, with the field strongest at the interface of the p and n region causing a drift current (a). The change in the potential is expressed in a built in voltage V_{bi}

potential for electrons, it needs to be constant across both semiconductor regions. Since electron affinity and band gap are invariant in semiconductors this can only be achieved in band bending of the valence and conduction band.

The electric potential of the p/n junction is obtained from Poisson's equation. In the Schottky approximation the SCR is assumed to have sharp edges (rectangular shape in x). This simplifies the calculation of the potential, where it can be ignored that the potential gradient and the number of diffusing charges are interdependent.

The p/n junction can be divided into four areas according to figure 2.1. For $x < -x_p$ and $x > x_n$ the ionized donor and acceptor impurities are shielded by free charge carriers and hence the charge density ρ is zero in this neutral region. With no free charge carriers in the SCR $-x_p < x < x_n$, the overall charge density must be neutral.

$$N_A x_p = N_D x_n \quad (2.2)$$

This statement also shows that a difference in doping concentrations for acceptors and donors N_A and N_D extends the SCR further into the less doped area.

The electric potential ϕ can be obtained by integrating the one-dimensional Poisson's equation

$$\frac{d^2 \phi}{dx^2} = \frac{e \rho(x)}{\epsilon} \quad (2.3)$$

twice for the individual areas and with the respective permittivities ϵ for the semiconductor materials. With the boundary condition for the built in potential

$$V_{bi} = \phi(+\infty) - \phi(-\infty) \quad (2.4)$$

the width w of the space charge region can be determined [5].

$$w = x_p + x_n = \sqrt{\frac{2\epsilon(N_A + N_D)}{eN_A N_D} V_{bi}} \quad (2.5)$$

Now, the validity of the Schottky approximation can be verified. The potential energy of the charge must be significantly larger than its thermal energy and the width of SCR significantly larger than the Debye length $L_d = \sqrt{\epsilon kT / e^2 N_{A/D}}$, so that

$$(V_{bi} - V) \gg \frac{kT}{e}. \quad (2.6)$$

Therefore, the Schottky approximation is valid for typical built in voltages greater than 0.5 V and for temperatures smaller or equal than room temperature, if the applied bias voltage is not too large. For metastability investigations it is of interest to analyze the distribution of the built in voltage V_{bi} and the band bending across the p- and the n-region of the junction. Regarding figure 2.1, the potential ϕ_p of the p-region at the interface $x = 0$ can be determined after integrating Poisson's equation (equation 2.3) twice.

$$\phi_p(x = 0) = \frac{e}{\epsilon_p \epsilon_0} N_A x_p^2 \quad (2.7)$$

With $w = x_p + x_n$, charge neutrality (equation 2.2) and equation 2.5 the width x_p can be calculated and plugged into equation 2.7 the potential yields

$$\phi_p(x=0) = V_{bi} \frac{\varepsilon_n N_D}{\varepsilon_p N_A + \varepsilon_n N_D} \quad (2.8)$$

From this equation it becomes evident, that increasing the acceptor doping concentration N_A results in a decrease of the potential gradient and the band bending in the p-region. This principle works in an analog way with the donor doping concentration N_D for the potential in the n-region.

2.1.2 p/n-heterojunction

The homojunction discussed in the the last section is based on the characteristics of one material where charge carriers only differ in their chemical potential. In contrast, in p/n-heterojunction solar cells, different materials with different band gap energies E_g , electron affinities χ and Fermi levels form the junction.

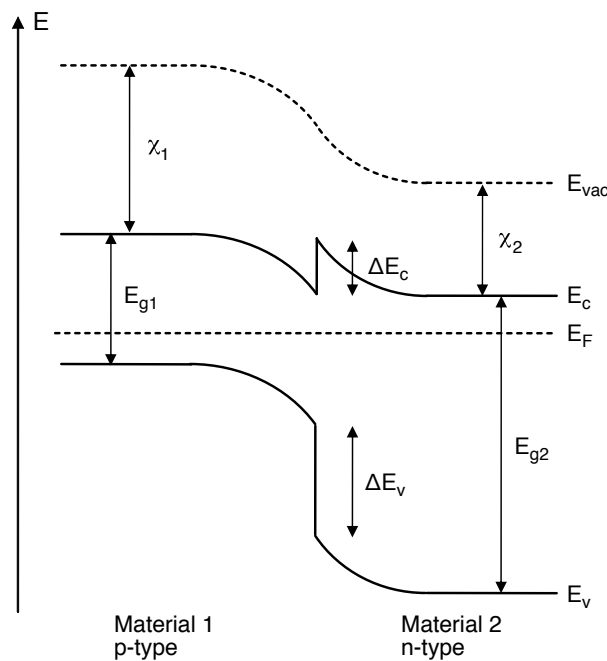


FIGURE 2.2: The band diagram of an ideal p/n heterojunction reveals a spike (ΔE_c) and a cliff (ΔE_v) at the interface of the conduction and valence band edges respectively.

In the band diagram, these characteristics are expressed in conduction and valence band discontinuities (figure 2.2). By aligning the Fermi levels for the two materials, the vacuum level will bend but be continuous. Since the electron affinity in semiconductors is defined as the energy necessary to excite an electron from the bottom conduction band level to vacuum level, it is a material constant that defines the distance between

conduction band level to vacuum level. Hence, the conduction and valence band edges will bend in the same way as the vacuum level and as a result the band edges on the p and n side will not be continuous. In the Anderson model [6] it is assumed that the conduction band offset (CBO) ΔE_c is equal to the difference in electron affinities.

$$\Delta E_c = q(\chi_2 - \chi_1) \quad (2.9)$$

Accordingly, the valence band offset (VBO) ΔE_v can be calculated as

$$\Delta E_v = E_{g1} + q\chi_1 - E_{g2} - q\chi_2. \quad (2.10)$$

In reality and due to a general mismatch in crystal lattice constants, crystal properties will be changed slightly at the interface because of the materials striving to minimize the total crystal energy. The interface region is also electrically and structurally influenced by the orientation of the material surfaces [7]. Crystal lattice constant mismatches also introduce dangling bonds and unoccupied states to the interface region, affecting the local charge distribution and hence the SCR width and band bending of the conduction and valence bands. Defects at the interface can also provide energy levels within in band gap, making them a potential pathway for leakage currents through the junction [8, 9]. In a simplified model, the Fermi level at an interface is only determined by the doping ratio of the two adjacent semiconductors. In addition however, interface charges can also influence the position of the Fermi level. These interface defect charges contribute to the charges required for creating thermodynamic equilibrium and equalizing the electrochemical potential. For devices with very high interface charge, the doping ratio between window and absorber can become irrelevant to the Fermi level position. This case is called Fermi level pinning (FLP).

2.1.3 Electrical characteristics

The maximum photocurrent generated by a solar cell is directly dependent on the number of incident photons, which create electron-hole pairs in the absorber. Through the quantum efficiency $QE(E)$ of a cell, the relation between the photocurrent density J_{sc} and the incident spectrum is given and is characteristic for various solar cell technologies and cell designs. Typical quantum efficiency curves for CIGS solar cells are displayed in figure 2.3. With $QE(E)$ as the probability of an incident photon of energy E resulting in a collected electron, J_{sc} becomes

$$J_{sc} = q \int b_s(E) QE(E) dE \quad (2.11)$$

with the electronic charge q and the number of photons per unit area, unit time and energy $E + dE$ as incident spectral photon flux density b_s . With the relation between

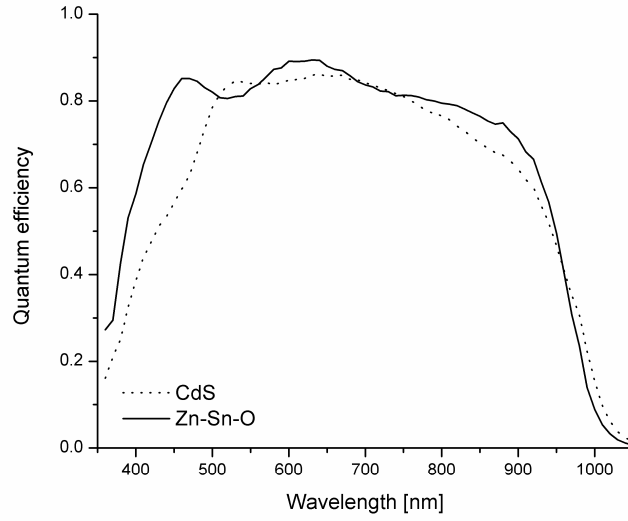


FIGURE 2.3: A highly efficient solar cell requires a high quantum efficiency covering a wide range of the solar spectrum. Here, the quantum efficiencies for two CIGS cells with CdS and Zn-Sn-O as buffer layers are shown.

energy E and wavelength λ defined by $E = hc/\lambda$, a convenient conversion between photon energies in eV and wavelengths in nm can be found in

$$E \text{ [eV]} = \frac{1240}{\lambda \text{ [nm]}}. \quad (2.12)$$

In a dark solar cell, the saturation current density J_0 is the sum of the drift current densities for electrons and holes

$$J_0 = q \left(\frac{D_n}{L_n} n_p + \frac{D_p}{L_p} p_n \right) \quad (2.13)$$

with the diffusion length for electrons L_n and the electron concentration in the p -quasi neutral region n_p . In thermal equilibrium the net current across the junction is zero, therefore the diffusion current is equal to the saturation current density $J_{diff}^0 = -J_0$. With an external bias V_e , however, the diffusion current becomes

$$J_{diff} = J_{diff}^0 \cdot e^{\frac{qV_e}{kT}}. \quad (2.14)$$

The diode equation (2.15) is the total current density across the dark p/n junction and a function of the external bias V_e and is

$$J_{diode}(V_e) = J_{diff} + J_0 = q \cdot \left(\frac{D_n}{L_n} n_p + \frac{D_p}{L_p} p_n \right) \cdot \left[e^{\frac{qV_e}{kT}} - 1 \right] \quad (2.15)$$

For an illuminated p/n junction, additional currents occur from generated electron hole pairs. With the generation rate per unit volume G , the additional currents add to the overall collected current density only if the generation happened within the diffusion length for minority carriers or in the SCR.

$$J_{light} = qGL_n + qGL_p + qGw \quad (2.16)$$

All other generated charge carriers recombine before being collected.

Generated electrons move from the p to the n region and therefore in the same direction as the drift currents. The diode equation under illumination becomes

$$J(V_e) = q \cdot \left(\frac{D_n}{L_n} n_p + \frac{D_p}{L_p} p_n \right) \cdot \left[e^{\frac{qV_e}{kT}} - 1 \right] - qG(L_n + L_p + w). \quad (2.17)$$

A plotted diode equation (figure 2.4) for a dark cell crosses the origin. In an ideal solar

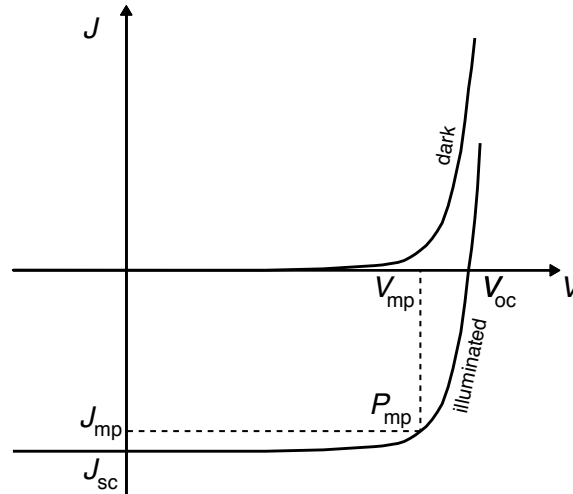


FIGURE 2.4: The current voltage characteristic reveals performance information about a solar cell. Key indicators are J_{sc} , V_{oc} , J_{mp} , V_{mp} and the fill factor FF .

cell, the illuminated curve is a parallel shift of the dark curve into the fourth quadrant, where a solar cell is operated to yield energy.

The short circuit current density J_{sc} at $V_e = 0$ is

$$J_{sc} = -J_{light} = -qG(L_n + L_p + w) \quad (2.18)$$

and the open circuit voltage V_{oc} at $J = 0$ can be written as

$$V_{oc} = \frac{kT}{q} \cdot \ln \left(\frac{J_{light}}{J_0} + 1 \right). \quad (2.19)$$

The operating point of a solar cell at maximum power P_{mp} defines the ideal current density J_{mp} and voltage V_{mp} for most efficient energy harvesting. The fill factor FF is a measure for how close the JV characteristic is to a rectangular shape and therefore is an indicator for solar cell performance.

$$FF = \frac{V_{mp} \cdot J_{mp}}{V_{oc} \cdot J_{sc}} \quad (2.20)$$

The overall efficiency η of a solar cell is defined as the fraction of power density delivered at the maximum power point P_{max} by the incident illumination power density P_s .

$$\eta = \frac{P_{max}}{P_s} = \frac{V_{mp} \cdot J_{mp}}{P_s}. \quad (2.21)$$

Since V_{oc} and J_{sc} are functions of temperature, a cell's performance is also dependent on temperature. For J_{sc} the effect is positive: atomic distances in the crystal increase with T and result in a reduced band gap E_g . This leads to more photons fulfilling the requirement $E > E_g$ which increases J_{sc} , however, the effect is rather small. For V_{oc} , on the other hand, the temperature effect is approximated by

$$\frac{dV_{oc}}{dT} \approx \frac{k}{q} \ln\left(\frac{I_{sc}}{B}\right) = \frac{1}{T} \left(V_{oc} - \frac{E_g}{q} \right) \quad (2.22)$$

with a temperature independent constant B . This term is always negative because $qV_{oc} < E_g$ and has a significant effect on V_{oc} and hence on the overall cell performance.

2.1.4 Non-ideal cell mechanisms and losses

Generally, loss mechanisms can be split up in three different categories. First, there are recombination losses limiting the V_{oc} of a device. Second are parasitic losses such as series and shunt resistances and voltage-dependent current collection mainly reducing the fill factor, but also affecting J_{sc} and V_{oc} . Last, there are optical losses preventing the generation of electron-hole pairs and hence limiting J_{sc} [10].

Thin film solar cells, including Cu(In,Ga)Se₂ and CdTe devices, oftentimes exhibit different behavior from standard well-behaved crystalline Si (c-Si) cells. While higher absorption coefficients due to a direct band gap can lead to higher currents, imperfect crystallinity and large numbers of defects cause shallow and deep defect levels and bands within the band gap and enhance recombination. The heterojunction introduces additional defect states to the interfaces, resulting in more recombination [10].

Recombination The V_{oc} is largely dependent on the probability of charge carrier recombination. There are several types of recombination mechanisms with varying probabilities for different areas within the cell and different cell types and materials.

For radiative recombination, an electron from the conduction band combines with a hole in the valance band and in effect releases a photon of an energy close to the band gap [11]. This recombination path is more prominent in direct semiconductors such as chalcogenides, rather than in indirect semiconductors, where it is usually neglected.

Shockley-Read-Hall (SRH) recombination is a two-stage process, where an electron relaxes from the conduction band to the valence band via an intra-band gap defect level (trap). This defect related recombination dominates all recombination mechanisms for state of the art chalcogenide solar cells [12]. The SRH recombination probability is largest for trap levels close to mid gap [11].

Auger recombination is the third, but least significant recombination process in chalcogenides, which only starts to dominate for high doping concentrations [12]. It involves three carriers: a conduction band electron and a valence band hole, which recombine and a second electron from either the conduction or the valence band, which absorbs the released energy from the recombined electron-hole pair. The excited second electron afterwards relaxes thermally within the crystal.

Generally, low recombination rates positively influence the carrier lifetime τ in the solar cell and therefore directly impact the diffusion length L of carriers.

$$L = \sqrt{D\tau} \quad (2.23)$$

With higher lifetimes and longer diffusion lengths, more minority charge carriers can reach the SCR and can be collected, whereas poor lifetimes result in an increased dependence on the electric field rather than on diffusion for minority carriers. This can lead to a voltage-dependent collection of light-generated current.

Parasitic losses The electrical behavior of a solar cell is described in the simplest form by an equivalent circuit including a series resistance and a shunt resistance as in figure 2.5. In an approximation, the ideal diode behavior of a cell is expanded by a parasitic series resistance R_s representing ohmic losses for the charge carriers in the p and n region and a parasitic shunt resistance R_{sh} , which accounts for leakage currents through the cell, around the edges and between contacts [11]. For high cell efficiencies, small series resistances and large shunt resistances are required. In the JV curve (figure 2.4), a high R_s decreases the curve slope at V_{oc} , while a small R_{sh} decreases the slope at J_{sc} . Unfavorable series and shunt resistances thus result in a decreased fill factor.

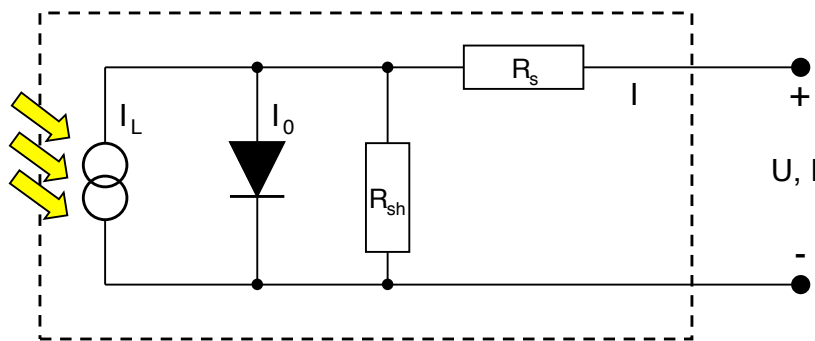


FIGURE 2.5: Equivalent circuit including series and shunt resistance.

A non-ideal diode equation takes into account an altered dependence of the dark current on V by an ideality factor A .

$$J = J_{sc} - J_0(e^{qV/AkT} - 1) \quad (2.24)$$

Typical values for A of well-behaved thin film devices lie between 1.3 and 2 and are dependent on the energies of deep defects acting as the dominant trap states [10].

2.2 Chalcogenides

Chemical and physical deposition techniques for large scale production basically enable the application of photovoltaic materials on large surface areas and at high throughput rates. This general advantage has driven the research and production of thin film solar cells to efficiencies on a par with polycrystalline silicon solar cells [13].

The two most efficient and commercially widespread thin film photovoltaic materials are based on $\text{Cu}(\text{In,Ga})\text{Se}_2$ and CdTe absorbers. These materials belong to the family of chalcogenides, which commonly includes sulfides, selenides and tellurides.

Chalcogenide materials look back on over 40 years of research for photovoltaic applications [14], however, there is still little knowledge about these materials in comparison to Si-based solar cells, where photovoltaic applications profit from decades of research in microelectronics.

In this chapter the key characteristics of CIGS and CdTe solar cells are summarized and serve as a basis for further discussions about metastability issues.

Chalcogenide solar cells are heterostructures formed by a metallic back contact, a semi-conducting absorber layer and a window layer emitter, which is transparent for most parts of the solar spectrum. CIGS and CdTe are direct band gap semiconductors, which makes them strong optical absorbers and allows for thin layers in the range of 1-3 μm . The absorber material in these solar cells is polycrystalline, however, grain dimensions

can extend across the entire absorber thickness.

Due to the polycrystalline structure the materials contain many intrinsic defects leading to traps and recombination centers, which drastically limit the diffusion length. For better carrier collection rates it has proven to be advantageous to replace the emitter with a wider band gap window layer, which minimizes front surface losses.

Although CIGS and CdTe are in principle available in both *p*- and *n*-type, heterojunction designs with *p*-type absorbers and *n*-type window layers have resulted in far better cell performances than the respective homojunctions [11].

2.3 Cu(In,Ga)Se₂ solar cells

The history of Cu(In,Ga)Se₂ (or simply CIGS) solar cells began in the 1970s when Bell Laboratory scientists created a 12% conversion efficiency CuInSe₂ cell [15]. Consequently, Cu(In,Ga)Se₂ cells were discovered and different deposition techniques explored with varying success (deposition-reaction, co-evaporation,...). Today, CIGS record cells have surpassed polycrystalline silicon cells and the material is the most advanced among all thin film technologies with a solar conversion efficiency of 20.8 % on a glass substrate [16] and 20.4 % on a flexible substrate [17] and a verified record of 20.9% by Solar Frontier [18]. Top efficiencies for commercially available modules currently range from 14-16%, still leaving a large gap between laboratory record cells and large scale applications.

With about 1.27 GW produced PV modules in 2013 CIGS technologies make up roughly 30% of thin film PV production, however, the overall market share has been declining in recent years and is now at 3%[19].

The following sections will elaborate on the physical principals and properties of CIGS solar cells, highlighting benefits and challenges of this material for solar cell applications.

2.3.1 Cu(In,Ga)Se₂ structure and composition

Cu(In,Ga)Se₂ is a semiconducting mineral in the group of chalcopyrites. It is a solid solution of the ternary compounds copper indium selenide CuInSe₂ and copper gallium selenide CuGaSe₂, both of which also function as photovoltaic materials [12].

A common CIGS solar cells stack consists of five layers and is illustrated in figure 2.6. A typical CIGS cell is grown in a substrate configuration with either glass or a flexible material like a metal or polyimide sheet as a substrate. After cleaning the substrate, typically a thin layer of 0.3-1 μm polycrystalline Mo serving as the ohmic back contact is deposited by sputtering. The *p*-type Cu(In,Ga)Se₂ absorber is then deposited on top

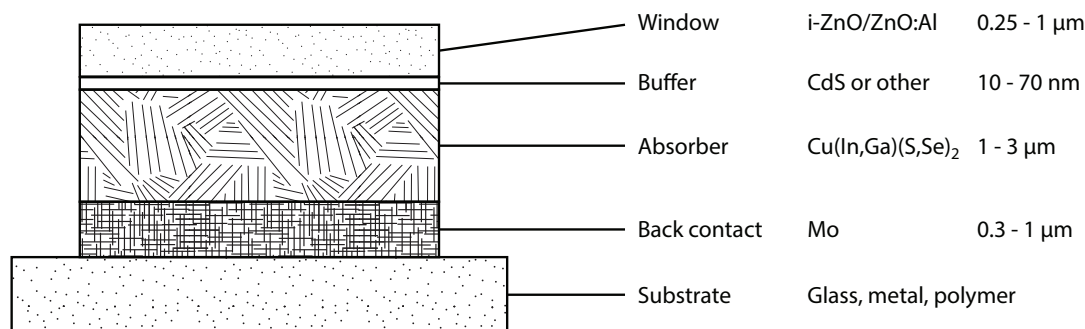


FIGURE 2.6: Layer structure of a typical Cu(In,Ga)Se₂ solar cell stack. The n-type optical window layers consisting of ZnO:Al, i-ZnO and a buffer layer are grown on top of the p-type CIGS absorber.

of the back contact with a thickness of 1-3 μm by processes like co-evaporation, CVD, ... The p/n junction of the heterostructure is usually completed with a 10-70 nm n -type CdS buffer layer applied by chemical bath deposition, a sputtered weakly n -type intrinsic ZnO layer (50-70 nm) and finally a sputtered heavily doped n -type ZnO layer.

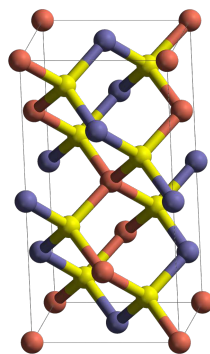


FIGURE 2.7: CIGS unit cell. Red = Cu, yellow = Se/S, blue = In/Ga [20].

Absorber The ratio of gallium and indium in Cu(In_{1-x},Ga_x)Se₂ can be varied in between either of the ternary compounds, which serves as a method to adjust the band gap of the semiconductor between 1 and 1.7 eV [21]. Also, some selenium atoms may be replaced by sulfur (Cu(In,Ga)(S,Se)₂), which is a preferred procedure for some deposition techniques.

The basic crystal structure of CIGS is shown in figure 2.7, where the blue spots can be occupied by either In or Ga atoms and the yellow spots by Se with some possible S replacements. Surprisingly, CIGS can function as a photovoltaic material in a wide range of off-stoichiometric compositions, making it a defect-rich material.

Growing Cu-poor CIGS creates native defects resulting in a naturally doped p -type absorber [14]. Using soda lime glass shows significant growth and device improvements due to the migration of Na-atoms from the glass into the active layers of the cell [22]. This can have a beneficial effect on grain sizes and the formation of the p/n junction

during the growth process resulting in an increased hole carrier density. Models proposed in literature suggest Na mitigating antisite In_{Cu} donor defects [23], introduction of Na_{In} antisite defects increasing the acceptor density [24] and Na compensating donor-like Se vacancy defects [25].

Buffer layer The buffer layer forms the contact between the absorber and the window layer. Ideally, the buffer layer is transparent for the relevant part of the solar spectrum, because it is assumed that charge carriers in the buffer layer are not collected and possibly recombine due to small carrier lifetime or interface recombination. It is considered a passivation layer for absorber surface states and acts as the electrical and optical transition layer between the p -type absorber and the n -type window [26]. A prominent material used for the buffer layer is CdS with a band gap of $E_g = 2.4 - 2.5 \text{ eV}$. Because of the low band-gap of CdS, the quantum efficiency of high energy photons is limited, leaving room for the development of alternative buffer layer materials [27]. Widening the band gap and eliminating the toxic material Cd from CIGS solar cells altogether poses a viable goal for the future.

Window layer The window layer serves as a transparent low resistant contact to the cell. In addition it acts as a diffusion barrier for chemical elements entering the junction and forms a high resistant layer to disable local contacts between absorber and window (shunts) [12]. ZnO is commonly used to complete the p/n junction due to its n -type conduction properties. A large band gap ($E_g = 3.3 \text{ eV}$) makes the window layer transparent to the visible part of the spectrum and enables absorption to mainly take place in the CIGS layer. Typically, a roughly 300 nm thick layer of low sheet resistance Al doped ZnO builds the low resistance window (LRW), with doping concentrations $> 10^{19} \text{ cm}^{-3}$. An about 100 nm thick layer of intrinsic (undoped) ZnO between the LRW and the buffer layer acts as the high resistance window (HRW) [12].

2.3.2 Band diagram and space charge region

Figure 2.8 shows the band diagram of a ZnO/CdS/CIGS heterojunction in thermal equilibrium. The buffer layer introduces a small positive CBO to the conduction band. At a first glance this barrier might not seem beneficial for electrons being drawn from the p -type absorber to the n -type contact by the electric field in the SCR. With a Fermi level E_F at the interface close to the conduction band, current losses due to recombination at the interface can be minimized [28]. In this inversion case, the n -type CdS layer is completely depleted and minority carriers from the absorber are majority carriers at the interface. Hence, they are not subject to significant recombination [5]. The

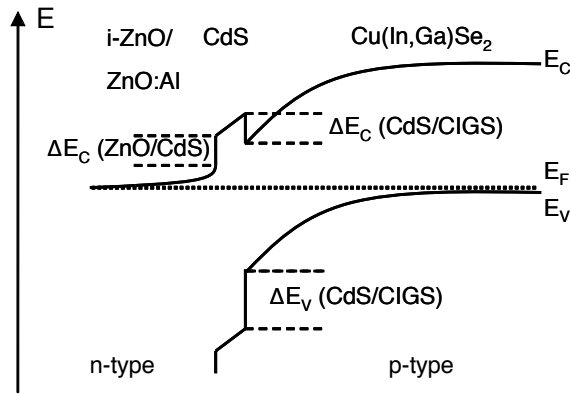


FIGURE 2.8: Band diagram of a ZnO/CdS/CIGS heterojunction. The band bending according to the respective electron affinities creates a spike ($\Delta E_c(\text{CdS/CIGS})$) and a cliff ($\Delta E_v(\text{CdS/CIGS})$) at the buffer layer/absorber interface and a cliff ($\Delta E_c(\text{ZnO/CdS})$ and $\Delta E_c(\text{ZnO/CdS})$) at the window/buffer interface.

electrical junction is now located entirely in the p -type absorber region and this effect can be enhanced by a positive CBO at the absorber/buffer interface. By modelling the charge transport and recombination, the effect of the CBO ΔE_c can be assessed. The most beneficial parameters are observed for $\Delta E_c < 0.5 \text{ eV}$, where the electrons are moved across the interface by a thermionic emission process [29]. If the CBO becomes negative, the theory [29] predicts, that the electrical junction is located closer to the material interface and recombination limits the V_{oc} . If the spike is too large, however, the collection of minority carriers from the absorber is obstructed, resulting in a reduced J_{sc} and FF .

2.3.3 Defects

As discussed in the previous section, in highly efficient solar cells, the CIGS absorber needs to exhibit p -type characteristics deep in the bulk, whereas an n -type inversion of the absorber is required close to the interface of the buffer layer [28, 30]. CIGS can be grown p -type under Cu-poor conditions, where the resulting native impurities act as dopants and make extrinsic doping unnecessary. In fact, active n -type doping creates a buried p/n junction, which significantly decreases the cell performance. The beneficial case of an above midgap Fermi level is instead created by the formation of a p/n junction with a matching set of a buffer layer and ZnO window layer [28].

While avoiding external doping offers technological advantages, relying on native impurities as dopants results in less controllable doping concentrations [31]. Shallow defects have energy levels close to one of the band edges, which makes them responsible for the doping of the crystal. For growing a strong p -type absorber, for instance, low formation

energies ΔH of shallow copper vacancies V_{Cu} and In_{Cu} defects are necessary. Low ΔH is a consequence of a weak Cu-*d*-Se-*p* bond and also inhibits the formation of a strong *n*-type region in the absorber [31]. Controlling Cu vacancies is therefore essential to achieving high efficiency CIGS cells. Because the formation energy of defects ΔH and the position of the Fermi level are generally mutually dependent on each other, controlling defect concentrations in the absorber can be a difficult task.

First principles calculations reveal that in off-stoichiometric, Cu-deficient CIGS, $\text{In}_{\text{Cu}}^{2+}$ donors and V_{Cu}^- acceptors can occur in large concentrations of several percent with an ideal concentration ratio of 1:2. Their electric activity, however, can be compensated by the formation of charge neutral $(\text{In}_{\text{Cu}} - 2V_{\text{Cu}})$ defect pairs due to their significant binding energy [32].

Deep defects, on the other hand, have energy levels close to the center of the band gap and are often associated with metastable effects in CIGS solar cells [31].

2.3.4 Metastabilities

This paragraph shall give a brief summary of past findings on metastabilities in CIGS solar cells and various models of explaining the effects.

CIGS solar cells can exhibit metastable behavior in their electrical parameters due to illumination or bias. A temporary increase or decrease of the open circuit voltage or the fill factor usually relaxes after illumination under dark storage conditions, which is why they are commonly referred to as metastabilities. Overviews of metastable effects and possible explanations are given by Scheer and Schock in [12] and by Eisenbarth in [33]. Early work on this matter describes a voltage and fill factor increase following light exposure and subsequent relaxation in the dark back to original values [34]. It was assumed that an external forward bias has the same effect on the cell as light soaking [34, 35]. The observed metastabilities on current-voltage (*IV*) characteristics later also became apparent by a number of other experimental results. A reversible rise in the junction capacitance after illumination was found by admittance measurements of CIGS cells [36] and by deep level transient spectroscopy (DLTS) [37]. Also, an increase in the space charge density was noticed in capacitance-voltage (CV) profiles [38, 39]. This supported the interpretation of persistent photoconductivity in CIGS absorber layers after illumination [40, 41] of pointing to an intrinsic feature of the polycrystalline CIGS material.

Later, it was found that illumination with either red, blue or white parts of the visible spectrum causes different responses in the cell behavior [42]. In [42] red light *JV* curves exhibit a kink (figure 2.9) in the fourth quadrant, which disappears after sufficient white light soaking.

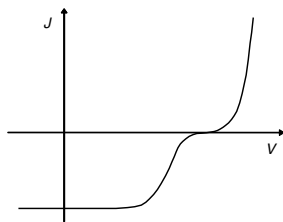


FIGURE 2.9: A kink in the light JV curve is a very pronounced form of voltage dependent photo current, caused by a barrier for the photo current. Different explanations for the origin of the barrier are given in [12].

The question whether metastable effects originate in the absorber layer or in the buffer layer was raised by [39] and is supported by observations of more pronounced metastable effects in CIGS devices with alternative non-CdS buffer layers [43, 44].

In table 2.1 a summary of observed metastable effects in CIGS films and solar cells is given according to Scheer and Schock [12].

Primary bias condition	Secondary bias condition	Primary parameter	References
Red light	$T \approx 300 K$	$C \uparrow$	[45]
		$\sigma \uparrow$	[46]
		$N_d \uparrow$	[39]
Blue light	$V_{oc}, T \approx 300 K$	$FF \uparrow$	[42]
White light	Open circuit	V_{oc}, FF, C, σ	[34, 36, 45]
Forward bias	Dark, $T \approx 300 K$	$V_{oc} \uparrow$	[34]
		$C \uparrow$	[47]
		$N_{d,p}$	[37, 48]
Reverse bias	Dark, $T \approx 300 K$	$C \uparrow$	[47]
		$FF \downarrow$	[49]
		$N_d \uparrow$	[50]

TABLE 2.1: Summary of observed metastabilities and their impact on electrical solar cell parameters in CIGS solar cells [12] with the solar cell capacitance (C) and conductivity (σ).

When talking about transient effects in CIGS solar cells, it is important to define a relaxed state, which is the starting point of any metastable change.

Relaxed state A CIGS solar cell, device or absorber which has been stored in the dark for several hours at elevated temperature ($330 K$) or for an even longer period at room temperature can be considered being in a relaxed state. Obviously, the relaxed state is difficult to analyze, because an illuminated JV characteristic or electrical bias will change the state of the device.

For field performance of devices, the relaxed state is not relevant, because the electrical

parameters during operation will be different from the relaxed state. However, the relaxed state can reveal viable information about CIGS cell behavior. Experimentally, the relaxed state is approximated by low temperature ($< 100\text{ K}$) and a measured JV curve under red light. Scheer and Schock [12] give a list of hypothetical characteristics, which should be found in the relaxed state of a CIGS device:

- A net acceptor concentration of $N_{A,a} = 10^{15}\text{ cm}^{-3}$ or lower in the CIGS absorber
- A V_{oc} below its optimum value in the order of 10 mV
- A low FF due to a voltage dependent photo current, potentially accompanied by a kink in the JV curve
- A cross over of the dark and light JV curves

Under these assumptions, a relaxed CIGS solar cell is far away from an ideal solar cell performance. Illumination or electrical bias can help by putting the cell in a metastable state, which might enhance electrical performance parameters. Unfortunately, CIGS solar cells exhibit strongly varying metastable behavior depending on stack design, material compositions and quality of films.

Red light effect Red sub band gap or near band gap illumination passes rather unaffected through the window and buffer layers due to their higher band gap energies and is mainly absorbed in the CIGS absorber layer. The red light soaking was observed to cause an increase in the lateral conductivity of CIGS films within the range of hours [41]. A slow decline to the initial value in a longer period of time is characteristic after switching off the illumination [36], which shows that CIGS films exhibit metastable persistent photoconductivity¹. Red light soaking causes an increase in mobility and an increase in the hole density [41]. The latter is also confirmed by a rise in the junction capacitance [51]. C-V profiling verified an increased net acceptor concentration $N_{A,a}$ after red light soaking, extending far into the absorber bulk and attributed to a Se-Cu divacancy complex [47], which will be described in the next section. These low temperature capacitance measurements [47] also show a temperature dependency in the metastable capacitance and conductivity increments, which suggests a required thermal activation. Cu-rich grown cells exhibit a smaller change in the space charge capacitance after red light illumination [52]. In these samples the density of Se vacancies is reduced in comparison to Cu-poor absorbers.

Scheer and Schock [12] summarize expected metastable behavior in the V_{oc} caused by an increase in the hole concentration upon red light soaking:

¹Persistent photoconductivity occurs in many semiconductor materials such as GaAs, CdS, MoSe₂ and ZnO [12] and describes the observed enhanced conductivity upon illumination.

- An increase in the absorber doping $N_{A,a}$ may lead to an increase in V_{oc} , for devices where efficiency is mainly constrained by recombination in the SCR. This is caused by a narrowing of the zone around $n = p$ and hence less recombination in the SCR.
- For cells where recombination in the quasi neutral region (QNR) is dominant, increased absorber doping can also result in a higher V_{oc} .
- In devices which do not show Fermi level pinning at the absorber/buffer interface but are still limited by interface recombination, V_{oc} will decrease with increasing $N_{A,a}$. This is caused by a decreased drop in the absorber potential with increasing $N_{A,a}$.
- For devices with Fermi level pinning, V_{oc} should be unaffected, because interface recombination is independent of $N_{A,a}$. If, however, interface recombination becomes complemented by tunnelling effects, V_{oc} is expected to drop with increasing $N_{A,a}$.

While most reported red light effects on CIGS observed an increase in V_{oc} , a decrease was also found [39]. Effects on the fill factor were reported as small and both enhancing [45] or decreasing [52].

The metastable state induced by red light starts to anneal above 300 K [12], which supports the common practise of dark storage for several hours in order to get to the relaxed state.

Forward bias effect Forward bias in the dark has a similar effect on CIGS devices as red light soaking does. An increase in the V_{oc} can be observed [34, 45] and the electrical capacitance rises as a result of an increased net acceptor concentration [47]. A hole trap at an energy of 0.26 eV found by deep-level transient spectroscopy (DLTS) showed to grow under forward bias [37] and was suspected to cause forward bias metastability. In modern cells, however, this trap level could not be found any more [49], while the forward bias effect was still present [47]. Therefore, this hole trap level is not considered a cause but rather a result of the forward bias metastability effect. Instead, a trap called N1 has been associated with metastable behavior. The trap activation energy varies and was found to shift to lower levels upon forward bias [53].

The forward bias effect is proposed by NREL as a procedure to activate modules prior to $I - V$ characterization instead of light soaking [54]. Because illumination under open circuit conditions automatically generates a forward bias in the junction, the forward bias effect was initially regarded as the cause of the metastable red light behavior. Also, the forward bias effect can be annealed at elevated temperatures back to the relaxed state. The current understanding, however, regards both types - red light and forward bias

- as the cause for an increased minority carrier concentration in the absorber material [12]. The availability of electrons in the absorber might be the common feature for both effects.

Blue light effect Light soaking of relaxed CIGS cells with blue light is associated with an increase in the fill factor, a reduced cross over between dark and light IV curves [12] and the removal of a red kink in the IV curve [33]. Also, a decrease in the junction capacitance has been observed [51]. Illumination with blue photons of an energy $h\nu > E_{g,buffer}$ suggests that the blue light metastability is triggered by photons absorbed in the buffer layer [42]. Time constants for relaxation seem to be different for blue light illumination with observed FF improvements persisting for a few minutes at room temperature [42].

In EBIC experiments the blue light effect can be reproduced with electrons irradiated at the cell's interface, where a barrier for the current in the relaxed state can be persistently removed [55].

White light effect Because white light contains both red and blue photons, often a combination of both metastable effects can be observed with V_{oc} and FF increase and persistent photoconductivity in the CIGS absorber. With an increase in the junction capacitance, it is argued that the red light effect dominates [12]. The available literature suggests that the white light soaking has a stronger effect on cells with Cd-free buffer layers.

Reverse bias effect Above 300 K at a voltage bias of $-1V$ a decrease in FF can typically be observed [50] along with an increase in the junction capacitance [38]. The question whether reverse bias brings a cell in metastable condition back to the relaxed state appears to be refuted by C-V measurements, where it is shown that the capacitance after reverse bias is larger than in the relaxed state [52].

2.3.5 Models for metastabilities

Several models have been developed in order to explain the metastable behavior of CIGS solar cells in its various aspects and shall be briefly introduced in the following paragraphs.

DX center model DX centers are deep levels in the absorber associated with donors. A well studied model of DX centers in AlGaAs describes a defect relaxation effect [56]

and serves as a physical explanation for CIGS metastabilities. Defects with strong electron-phonon coupling can undergo transitions from shallow to deep levels after electron capture and increase the net acceptor density [36, 37]. This might be an explanation for an increase in the space charge density and the persistent photoconductivity observed after light soaking or after forward bias influence. An increase in V_{oc} is then explained by a reduction in the SCR where Shockley-Read-Hall recombination is prevailing. Density functional theory (DFT) calculations revealed that defects such as In_{Cu} antisites show DX-type behavior with shallow-to-deep transitions upon charge carrier capture [57].

Cu-migration model For small E_n the formation enthalpy for V_{Cu} can become negative, resulting in spontaneous formation of copper vacancies



This has been shown theoretically [58] as well as experimentally [59]. The mobile Cu_i^+ ions drift away from the heterointerface under the influence of a reverse bias electric field with a diffusion constant of 10^{-13} to $10^{-10} \text{ cm}^2/\text{s}$, leaving behind V_{Cu}^- acceptors [60]. This leads to an increased negative space charge density near the interface region.

CdS photodoping model A cross over of dark and light JV curves is generally not observed in cells where all photons are absorbed in the CIGS bulk layer, however, it can be found in many CIGS devices. The cross over and the red kink in JV characteristics can be ascribed to a spike in the conduction band coupled with a low net doping concentration in the CdS buffer layer causing a photocurrent barrier [42, 61]. This barrier seems to disappear upon illumination with blue light and is explained in the CdS photodoping model as a modification in the occupation of deep states in the CdS buffer layer, illustrated in figure 2.10. A reduction in the barrier across the buffer layer can also relate to an increase in the FF upon illumination with blue light. Experimental observations of JV curve cross over and red kink in cells with different absorber and buffer compositions and thicknesses could be ascribed to the photodoping model [62, 63].

In contrast to the photodoping model, interpretations of admittance spectroscopy lead to a different conclusion. Admittance spectroscopy of CIGS cells reveal signatures, which correspond to defect states, however the exact spatial location of the defects cannot directly be measured. For many years the defect density level N1 was understood as a donor defect at the CdS/CIGS interface, which required Fermi level pinning at the heterointerface [64]. A pinning, however, would not allow for changes in the effective conduction band barrier upon increased CdS doping and therefore not be consistent

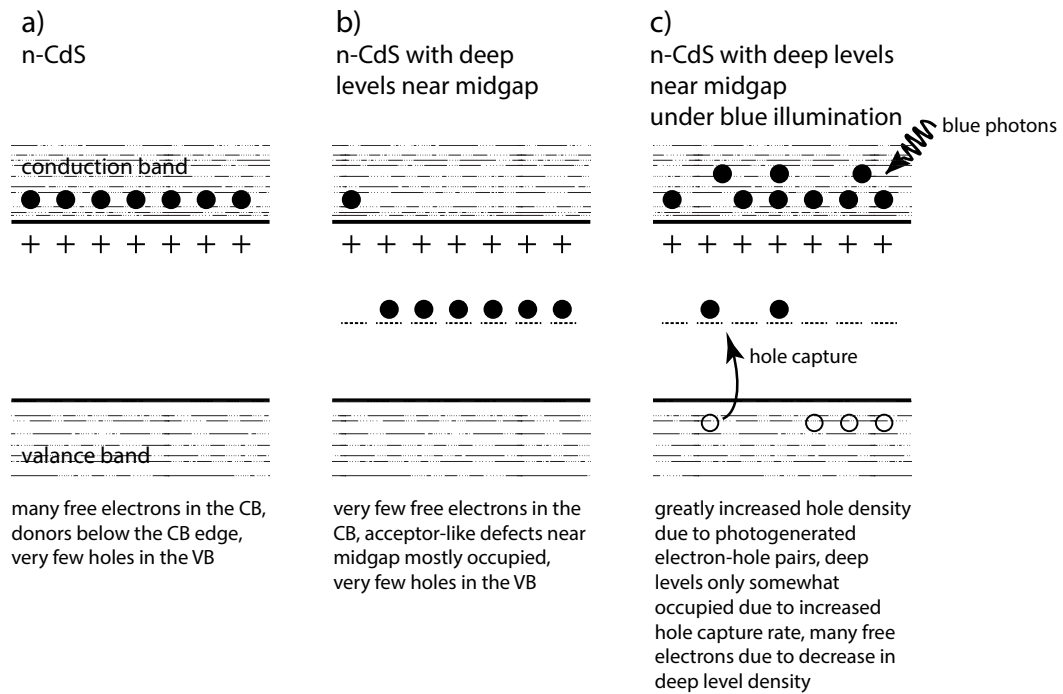


FIGURE 2.10: The CdS photodoping model explains how phenomena observed in JV characteristics (cross over, red kink) can be related to mid gap defects in the CdS buffer layer. [42].

with the CdS photo doping model [65]. In order to reconcile the two models, a p+ layer with deep acceptor levels was assumed to be present close to the heterointerface.

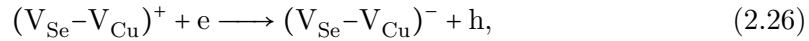
p+ layer model In this model a highly doped p-type region is assumed to be present in the absorber close to the interface. The accumulated acceptor concentrations in this region create a photocurrent barrier in the band, which relates to poor FF, but is subject to metastable changes after illumination [30]. The FF improvement, however, is linked to the net doping of the absorber region close to the interface rather than to the potential drop across the buffer layer [53]. Under blue light soaking, holes created in the buffer layer are assumed to get trapped by the close p+ layer, resulting in a reduced space charge density and a reduction in the photocurrent barrier. Experiments with reverse biasing cells exhibit a loss in FF, which can be explained by an increase in the p+ layer that leads to a higher photocurrent barrier [53].

Amphoteric defect model So far the most comprehensive model accounting for metastable red and blue illumination effects as well as the reverse bias effect was proposed by Lany and Zunger [66, 67]. The amphoteric defect² model suggests a Se-Cu divacancy

²The term amphoteric is derived from the Greek word meaning "both" and refers to defects, which can exhibit either donor or acceptor configuration and different charge states.

complex ($V_{Se} - V_{Cu}$) based on DFT calculations to be the source of metastable effects in CIGS solar cells. The ($V_{Se} - V_{Cu}$) complex was found to exist in two different structural configurations isolated by energy barriers. In CIS and CIGS with a low Ga concentration, the donor configuration with a charge state 0 and 1+ creates a shallow n-type donor level. In CGS and CIGS with a high Ga concentration, only the donor level with a charge state 1+ occurs. The acceptor configuration results for all CIGS compositions in either a shallow p-type acceptor level with charge states 0 and 1- or in very deep 2- and 3- acceptor states. The model predicts a highly p-type region in the absorber close to the buffer interface, similar to the p+ layer model [33].

Transitions between the donor and acceptor states involve the thermal activation of an energy barrier as well as simultaneous capture of electrons for donor-to-acceptor transitions and holes for acceptor-to-donor transitions. Therefore, excess carriers present upon illumination or bias result in a shifted equilibrium distribution of initial donor and acceptor states of the ($V_{Se} - V_{Cu}$) complex. Metastable states induced by red light or forward bias are thought as a change in extension and charge density of the p+ type region and occur as a donor-to-acceptor transition by the persistent capture of photoelectrons from red illumination following the defect reaction



and leading to persistent photoconductivity and an increase in the net p doping and device capacitance and a reduction in the width of the space charge region.

In contrast, the acceptor-to-donor transition is realized by the persistent capture of holes, which were originally photoexcited in the buffer layer upon blue illumination and swept into the CIGS absorber. The capture requires existing ($V_{Se} - V_{Cu}$) complexes in the acceptor configuration prior to blue illumination and follows



and as a result, the net acceptor concentration and the device capacitance decrease.

2.4 CdTe solar cells

The first cadmium telluride photovoltaic cell dates back to 1963 and was realized by a General Electric Research Laboratory [68]. Early promising efficiencies but unstable devices were succeeded by cells well above 10 % efficiency. Due to a very forgiving material, many different depositions techniques such as vapor transport deposition, electrodeposition, spray pyrolysis and screen printing lead to the advances in CdTe solar cells.

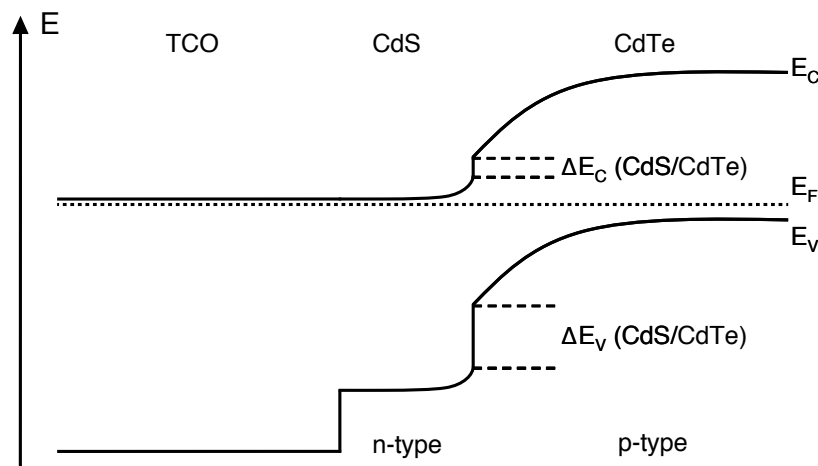


FIGURE 2.11: Band diagram of a CdTe/CdS heterojunction with conduction and valance band offsets. Unlike CIGS, CdTe junctions do not create a spike at the absorber/buffer interface.

The current CdTe world record cell is held by First Solar at a 21.0 % conversion efficiency, which has surpassed the record for polycrystalline Si cells [13]. Like for CIGS, the CdTe technology has difficulties closing the gap between record cell and commercial module efficiencies. Nevertheless, CdTe modules are manufactured on a GW/year scale and make up for more than half of the entire thin film PV market to day [1]. Commercial CdTe module production has demonstrated for several years the cost benefits thin film technologies can have over wafer-based photovoltaics, with a total production time for a CdTe module from simple glass to a PV module in two and a half hours [69]

The following sections will give a brief summary of the characteristic properties of CdTe solar cells, highlighting benefits and challenges of this material for solar cell applications.

2.4.1 CdTe structure and composition

The II-VI group semiconductor CdTe is an ideal material for photovoltaic applications with a very high optical absorption of $> 10^5 \text{ cm}^{-1}$ for visible light and a direct band gap of 1.44 eV, which is close to the optimum for photovoltaic energy conversion [70]. Figure 2.11 shows the band diagram of a CdTe/CdS heterojunction. The band gaps of the buffer layer and the window layer are 2.4 eV and 3.6 eV respectively. Like in CIGS, the direct CdTe semiconductor leads to a very thin active absorber layer of only a few μm being able to absorb more than 90 % of relevant above band gap photons.

CdTe devices are typically fabricated in a superstrate structure, where the layers are deposited on a glass substrate in the same order as light is passing through the device, starting with the front contact/window layer (figure 2.12). Interdiffusion between the

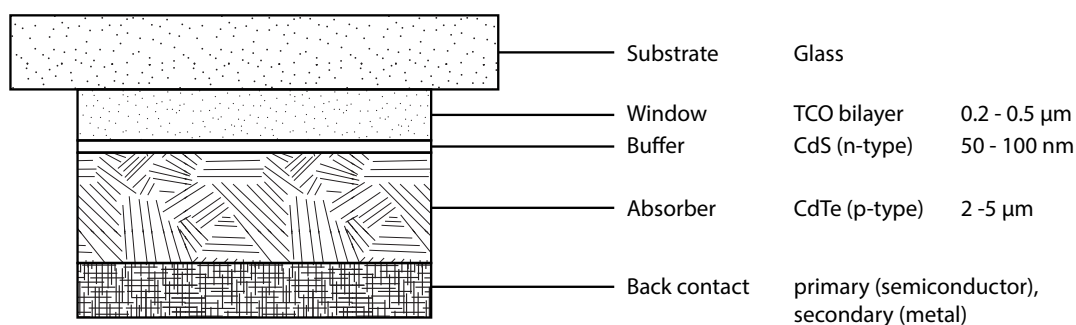


FIGURE 2.12: Layer structure of a CdTe solar cell stack. The cell is typically deposited in a superstrate configuration.

CdS buffer layer and the CdTe absorber due to the process sequence is believed to be among the reasons why the superstrate configuration outperforms the substrate configuration and hence is preferred. Most commonly, low iron soda lime glass or borosilicate glass serve as substrates for CdTe devices, however, polymer foils can also be used in the superstrate structure, where efficiencies above 11 % have been realized [71].

Window layer Depositing the window layer directly onto the substrate in the superstrate configuration has several advantages. Deposition temperatures are only dependent on the substrate and hence can technically be high in case of using glass. Generally speaking, a glass substrate also provides a very smooth surface, which facilitates creating degradation resistant layers. Besides these advantages, being the first layer deposited, the window layer has to survive subsequent process steps.

Most high efficiency CdTe solar cells rely on a bilayer window with a low and a high resistance part (LRW, HRW). Due to the band gap of the absorber, the window layer only needs to be transparent in the visible range up to 900 nm. The HRW serves the purpose to prevent shunts but positive impacts on V_{oc} and J_{sc} have also been reported [72] as well as an increased red light carrier collection [73].

Buffer layer Most efficient CdTe devices rely on a CdS buffer layer. It is photoelectrically mostly inactive, grows natively n-type and is used to increase the minority carrier lifetime by passivating surface states and reducing reflexion losses. However, the buffer layer also absorbs otherwise useful photons and it is generally assumed that carriers generated in the buffer layer recombine and cannot contribute to carrier collection. For practical reasons, the CdS layer is often deposited with the same technique as the CdTe absorber, however, chemical bath deposition or chemical vapor deposition of the buffer may yield better results [12].

The thickness of the layer needs to be delicately tuned, since very thin CdS layers $< 100\text{ nm}$ can lead to local shunts between the window and absorber, which is expressed in reduced values of V_{oc} and FF [73]. The overall benefits of a buffer layer are currently regarded in the passivation of surface states of the CdTe absorber and an advantageous band transition between window and absorber [12].

Absorber Although CdTe can technically also be doped n-type, common solar cell designs rely on the native p-type absorber. Due to a high formation enthalpy, CdTe is thermodynamically very stable with a melting temperature much higher than its individual constituents. Among the depositions processes suitable for the growth of efficient CdTe solar cells are physical vapor deposition (PVD), close space sublimation (CSS), vapor transport deposition, sputter deposition, electro deposition, metalorganic chemical vapor deposition (MOCVD), spray pyrolysis and screen printing. First Solar, Inc., the world's largest thin film PV manufacturer, relies on the vapor transport deposition process and currently holds the world record for CdTe solar cell efficiency [74].

Applying the above mentioned deposition techniques for thin film growth results in a polycrystalline structure with grain sizes in the range of around $1\ \mu\text{m}$. After deposition, the absorber is activated with a CdCl_2 treatment, which significantly enhances the performance parameters of the device. The CdCl_2 treatment helps the junction formation at the CdS/CdTe interface [75], facilitates recrystallization of small grains and passivates grain boundaries [76]. Consequently, electrical parameters (i.e. V_{oc} , J_{sc} and FF) improve significantly. Recently, MgCl_2 was proposed as a cheaper and environmentally friendly substitute for the toxic CdCl_2 activation step, bringing forth the same benefits to CdTe device performance [77].

2.4.2 Defects

A direct relation between defect densities and device performance has not been proven thus far [12], nevertheless, it is essential to understand defects for further technological improvements.

The position of the defect level in the band diagram determines the nature and effects of the defect. Levels within the band gap can roughly be classified into recombination centers, electron traps and hole traps. While electron trap levels lie close to the conduction band edge, hole trap levels are close to the valence band edge. Traps tend to re-emit a captured charge carrier back to its original state, midgap levels, however, are associated with recombination centers, where both trapped charges can be trapped and therefore are more likely to recombine than being re-emitted. Deep recombination centers therefore directly reduce the V_{oc} of a device.

The defect type is determined by the capture rate and to define a level between traps and recombination centers, a so-called demarcation level can be introduced [12]. For p-type semiconductors, defect levels between the hole quasi Fermi level E_{Fp} and the demarcation level act as recombination centers (figure 2.13) and vice versa in n-type semiconductors. Generally, it can be distinguished between intrinsic defects and defects

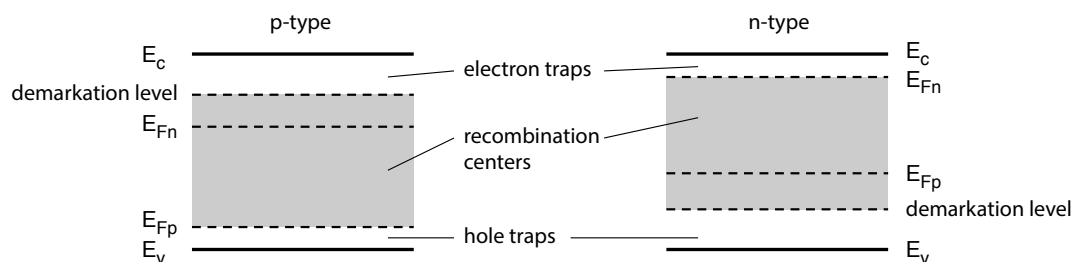


FIGURE 2.13: The demarcation energies show the dominant defect type at a certain energy level in the band gap. Midgap levels, or deep centers are associated with recombination centers, while defect levels close to the band edges are electron or hole traps which tend to re-emit the captured charged carrier again. The energy levels defining recombination centers is marked by the demarcation level and the quasi Fermi levels for holes E_{Fp} and electrons E_{Fn} in the p- and n-type semiconductor respectively [12].

from impurities. Intrinsic defects occur as interstitials, vacancies or antisites and at shallow energy levels they can be present as donors or acceptors. However, according to calculated defect levels in the CdTe band gap [78], most intrinsic defects lie below the demarcation level and are considered deep recombination centers.

Impurities, on the other hand, generally appear as shallow defects [78] where they can act as donors or acceptors.

The chlorine treatment alters the hole concentration in the absorber and changes the defect levels by introducing O, Cl and Cu atoms. More defects can generally be found in CdTe devices with no or insufficient chlorine treatment [79]. The healed defects mostly originate from grain boundaries, where problematic lattice mismatch results in high defect densities.

2.4.3 Metastabilities

Under non-equilibrium conditions such as illumination or bias, the occupation of deep defects can shift. Different capture cross sections for electrons and holes lead to a defect state occupancy in favor of one charge carrier type, which in turn influences the energy bands.

For example, if the capture cross section for holes in the absorber is significantly larger than for electrons $\sigma_p \gg \sigma_n$, more holes will be trapped in deep acceptor states upon illumination. As a result, the net negative charge close to the buffer interface will be

reduced, which also reduces the charge density in this region. The band diagram under illumination will therefore resemble one without deep defect states [12].

Deep acceptor defects in the buffer can also be altered by light. If the majority of these deep states is occupied, the region is negatively charged in equilibrium conditions. Under illumination, however, if $\sigma_p \gg \sigma_n$, the deep acceptor defects states are emptied due to a discharge by photo generated holes. Positively charged donors change the space charge in a way that the buffer space charge can partly compensate the absorber space charge, which leads to a reduction in the band bending of the buffer layer.

CdTe solar cells can be subject to anomalies in the behavior of the JV curve, which may

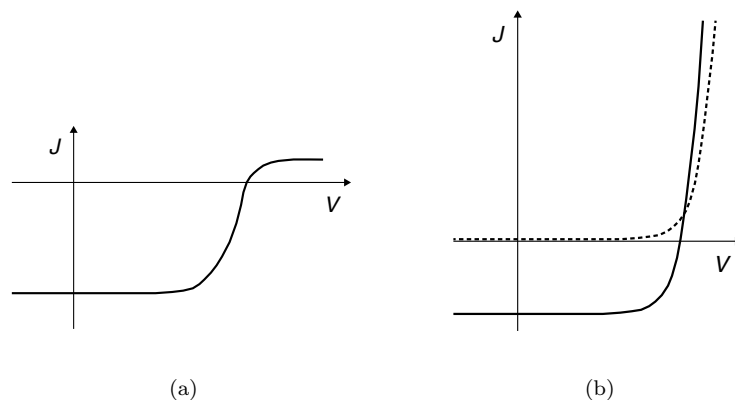


FIGURE 2.14: Roll over (a) and cross over (b) anomalies in JV curves of chalcogenide solar cells. A roll over shows the limitation of the diode current at forward bias, which is mostly due to a barrier for the diode current at the back contact. Cross over describes the intersection of dark and light JV curves at forward bias.

change after illumination or bias. In the roll over effect for a dark or a light JV curve (figure 2.14(a)), the current is limited at forward bias. This can generally be ascribed to a barrier for the diode current located at the back contact [80, 81] and has been observed in CdTe solar cells [82]. Roll over effects with currents not completely limited, but still some voltage dependence can also occur [83].

Another anomaly that can affect poorly efficient cells as well as high efficient devices is the cross over of the dark and the light JV curve [84], where the curves intersect at a high forward bias (figure 2.14(b)). The effect can be ascribed to an electron barrier at the conduction band edge in the interface region between absorber and buffer [85, 86]. This barrier can be reduced by blue illumination and hence photodoping of the buffer layer, resulting in a higher diode current under illumination [87]. Different occupations in deep acceptor states in the buffer layer can cause a shift of the electron barrier. However, also charged states in the interface region of buffer and absorber may influence the electron barrier.

If a roll over and a cross over are observed in the same device, the cross over might also be caused by recombination at the back contact [88]. This also results in a higher diode

current upon illumination.

Metastabilities affecting the V_{oc} of a CdTe solar cell have also been recorded in the literature. Typically, an increase between 2-6 % upon light soaking was noted [35, 89]. The increased V_{oc} regresses after storage in the dark. A V_{oc} increase may also be counteracted by stressing a cell through short circuiting or reverse biasing it.

Metastable effects can also manifest in the current with either an increase [90] or decrease [91, 92] upon illumination. A hysteresis in the JV curve depending on the voltage sweep direction can be observed and typically, cells with a low performance show a stronger expression of the effect [92]. This is also the case for permanently degraded cells and modules [89]. Proposed models for the current metastability include charged or discharged states of deep defects, which can cause a potential reduction in the absorber [92]. This way, both an increase or decrease in the the diode current could be explained. Metastabilities caused by charged defect states are reversible and reproducible [12], however, another class of metastable effects describes jumps in the JV characteristic, which are thought to stem from nonlinear shunt paths through the junction [90].

Chapter 3

Verifying Metastable Effects

There are several ways to approach the topic of metastabilities in chalcogenide solar cells. Obviously, defect characterization techniques applied in various illumination states of cells can give indications about the underlying mechanisms, which drive metastabilities. Several research groups have used admittance measurements such as capacitance-voltage (CV) profiling, admittance spectroscopy (AS) and deep level transient spectroscopy (DLTS) among others to learn about the defect characteristics of thin film PV devices. Admittance measurements rely on an applied ac-voltage and the subsequent current response from the cell. They utilize the capacitive characteristics of cells which originate from the cell geometry, the depletion region, voltage dependent diffusion, barriers (a second depletion region) and the charging and discharging of defect states. This works for processes in the cell where charge carriers are able to follow the frequency of the ac-signal, which is also dependent on temperature [93, 94].

While these defect analyzing techniques are very valuable for the fundamental understanding of metastabilities, they are not very applicable to encapsulated devices and modules of large size. The methods used in this work mainly rely on the analysis of the JV characteristic for both cells and modules, as well as measurements of quantum efficiency, photoluminescence and x-ray diffraction, which give the most insight on practical device behavior.

The following sections will elaborate on these methods, their functional application and interpretation pitfalls and go into detail about utilized measurement set-ups. Current guidelines for measurement practices and especially standards for module characterization will be reviewed and discussed.

3.1 Cell characterization

Compared to standard Si based cells, CdTe and CIGS thin film solar cells diverge in their device performance characteristics, which necessitates a closer assessment of performance measurements and analysis.

Despite major differences in composition, device structure and processing between CdTe and CIGS, these technologies have much in common regarding their performance behavior.

Starting with the sun as our energy source, the output of a solar cell needs to be compared to a standard power density spectrum of solar radiation. This standard is called the AM1.5 standard spectrum and corresponds to solar irradiation outside the earth's atmosphere (AM0) after passing through 1.5 times the air mass of the atmosphere. These AM1.5 conditions can be found at a solar zenith angle of 48.19° and the incident power on a flat surface is equivalent to 1000 W/m^2 or 100 mW/cm^2 .

3.1.1 Quantum efficiency

The QE measurement provides the basics for understanding the short circuit current of a solar cell by measuring the conversion efficiency spectrally resolved. Thereby, the QE is given as a dimensionless ratio of collected electrons per incident photons at a given wavelength. External QE does not take into account optical losses from reflection or transmission. By subtracting these losses, the internal QE, which is only due to the photogeneration and collection in the absorber, can be obtained. For crystalline Si cells it makes sense to define QE_{INT} as $\text{QE}/(1 - R)$, however, in thin film solar cells, this definition for QE_{INT} oftentimes needs to be adapted, since reflections can also occur at all layer surfaces, which cannot be quantified with a simple reflectance measurement.

Integrating the product of the quantum efficiency (figure 2.3) with the solar AM1.5 spectrum gives the short circuit current density J_{sc} , and typically it is a good verification of the QE measurement. This is especially the case for well behaved crystalline Si solar cells, however, thin film devices can show deviations when the carrier collection is dependent on the incident photon density and the spectrum [95]. Different from crystalline Si devices, optical losses can occur in the TCO layer or in the buffer layer, while electronic losses are mainly accounted for by recombinations in the absorber. Figure 3.1 schematically shows the respective loss areas in a QE graph, as analyzed in more detail in [10].

Care must be taken when the QE measurement is done under a voltage bias. Transport in chalcogenide cells is only restricted by the minority carriers in the p -type absorber

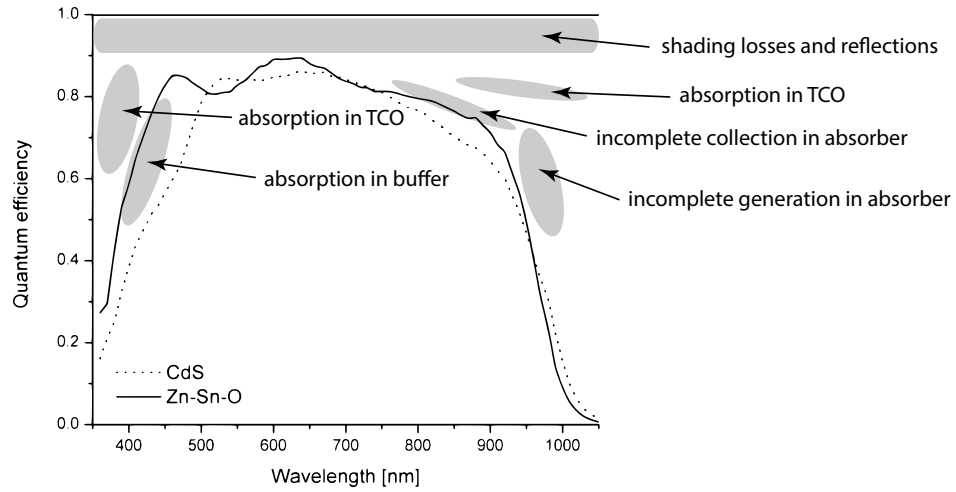


FIGURE 3.1: Optical and collection losses affect different spectral parts in the quantum efficiency curve. In this example two CIGS QE curves with different buffer layer materials are shown.

i.e. electrons. For these cells QE_{INT} can be approximated by

$$QE_{INT}(\lambda, V) \cong 1 - \frac{e^{-\alpha(\lambda)W(V)}}{\alpha(\lambda)L + 1} \quad (3.1)$$

with the absorption coefficient $\alpha(\lambda)$, the width of the space charge region $W(V)$ and the effective diffusion length L [96]. Because of the voltage dependency of $W(V)$, the quantum efficiency $QE_{INT}(\lambda, V)$ also relies on the applied bias.

A typical quantum efficiency setup utilizes a monochromatic light source to detect the response from the solar cell. Figure 3.2 shows a schematic setup for such a QE measurement. Light from a stable light source is chopped and put either through a monochromator or a filter wheel in order to get monochromatic light. For calibration the light is directed on a reference cell before the sample solar cell is tested. The resulting current output of the cell is further converted into a voltage signal and increased with a lock-in amplifier, which is triggered by the chopper wheel. Disturbances from temporal light fluctuations can be corrected with a monitor diode tracking the intensity during calibration and measurement. For cells with low current output or cells sensitive to illumination intensity, an additional bias light can be applied in addition to the monochromatic light on the test sample.

The QE measurements done in course of this work rely on setups using monochromators. Thereby, a high wavelength resolution and a broad spectral range can be achieved. Also, the area illuminated by monochromatic light is only a few millimeters in diameter, fitting entirely on a single solar cell in between any front contacts. Both, the QE setup at the Ångström Solar Center of Uppsala University and the setup at the Austrian Institute of technology work with these principles. A bias light for an increased output current can

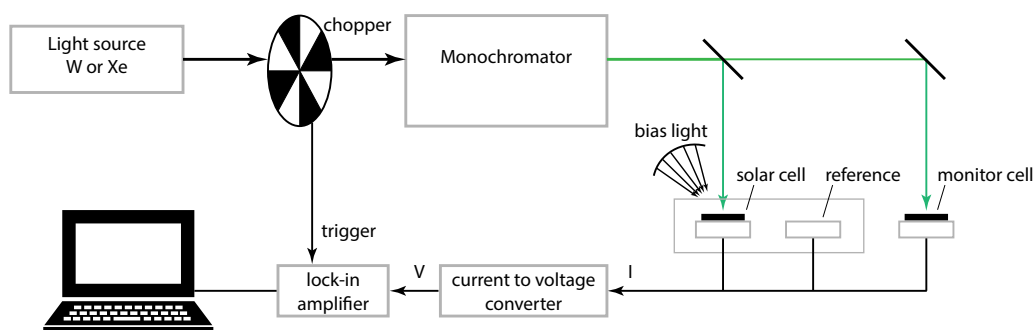


FIGURE 3.2: The setup for measuring the quantum efficiency of a solar cell relies on monochromatic light illuminating the test device and sensitive signal processing for detecting the small current changes due to illumination at different wavelengths.

be applied to the cell in both cases, however, it was not necessary for the investigated cells. Also, additional light soaking through the bias light was being avoided.

3.1.2 Current-voltage measurement

The JV analysis is the most common and a fairly easy solar cell characterization technique. Under standard reference conditions of 100 mW/cm^2 of AM1.5 illumination at a cell temperature of $25 \text{ }^\circ\text{C}$, the basic parameters V_{oc} , J_{sc} , FF and the efficiency η can be extracted from the JV characteristic. Definitions of FF and η are given in equations 2.20 and 2.21 in chapter 2.

A JV measurement setup typically comprises a natural or artificial light source, a mounting structure for the device under test (DUT), temperature sensors and control, an external load or power supply for applying a voltage or current to the cell and a device to record the current or voltage signal from the cell. An electric circuit for a typical JV measurement setup is shown in figure 3.3. The solar cell is biased with a variable load while the current is measured using a four-point probe. This is necessary to eliminate measurement errors due to the voltage drop in the current-carrying electrode connection. An error like this would change the operating point in the JV characteristic. Thus, an additional pair of electrodes is used for a voltage measurement where practically no voltage drop occurs across the connection, because these electrodes carry very little current.

The international IEC standard 60904 [97] for photovoltaic devices defines the correct JV measurement which must be applied by certified test laboratories. In a JV measurement setup (figure 3.4) the illumination, temperature, electronic load and electronic measurement need to be controlled. A light source acting as a solar simulator must be

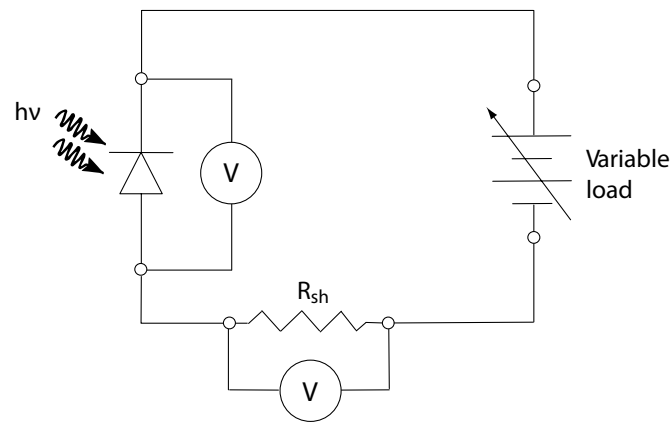


FIGURE 3.3: Circuit for a typical current-voltage measurement.

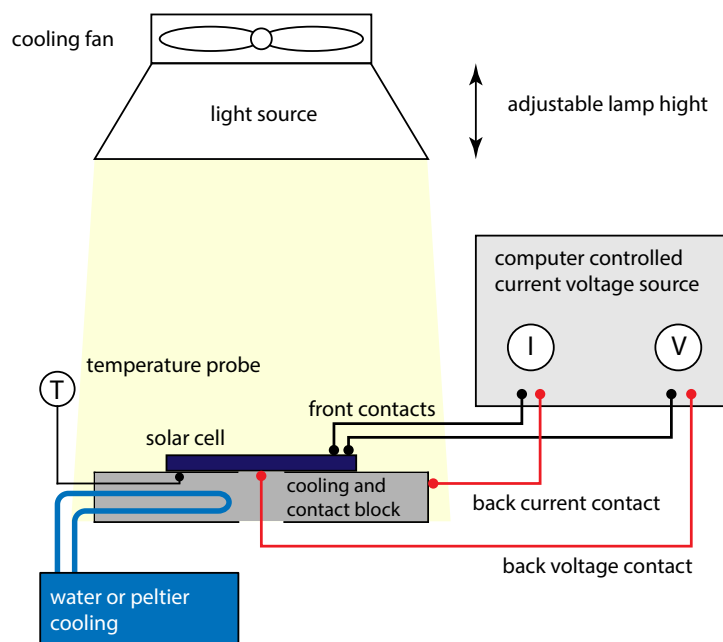


FIGURE 3.4: Typical measurement setup for solar cell JV characterization.

stable in spectrum and illumination intensity at least for the duration of the measurement sweep. The correct illumination can be adjusted by the lamp power or the distance to the test device. Additionally, a monitor cell is also sometimes used to keep track of timely fluctuations in the illumination.

Since many solar cell parameters are temperature dependent, temperature control of the device during characterization is a critical issue. For a standardized test the cell temperature must be kept at 25 °C.

For comparing solar cells the basic parameters V_{oc} , J_{sc} , FF and η proved to be very useful, however, more information regarding the quality and characteristics of a cell can

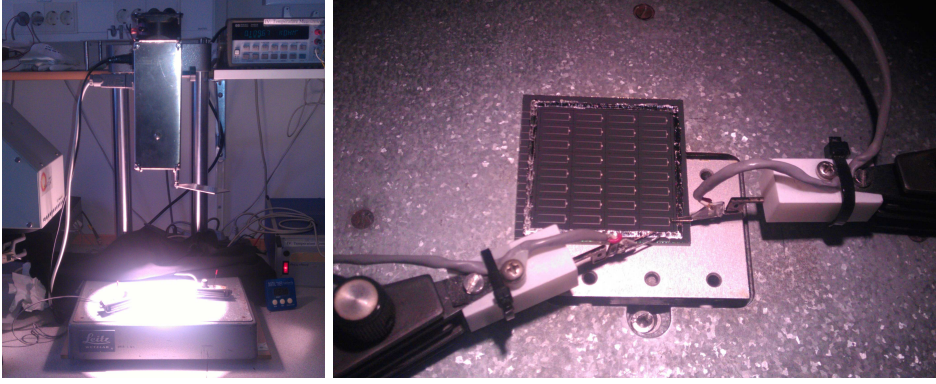


FIGURE 3.5: Measurement setup for JV characterization at Uppsala University.

be extracted from analyzing the entire JV curve. The difference from high efficiency c-Si or III-V solar cells regarding JV behavior becomes apparent under varying light intensity or temperature and can be ascribed to the prevalence of parasitic losses in thin film solar cells. Therefore, a description of thin film solar cells beyond the basic cell parameters entails the separation of recombination losses from other parasitic losses. The details of a JV analysis for thin film solar cells are elaborated by Hegedus and Shafarman in [10]. In their paper, they describe the JV characteristic with a diode equation

$$J = J_0 e^{\frac{q}{AkT}(V-RJ)} + GV - J_L \quad (3.2)$$

with the approximation of a largely voltage independent light-generated current J_L , series resistance R , shunt conductance G and the ideality factor A . The diode current J_0 is expressed as

$$J_0 = J_{00} e^{\left(-\frac{\Phi_b}{AkT}\right)} \quad (3.3)$$

with the factor J_{00} defining the prevalent recombination mechanism and the barrier height Φ_b .

In order to determine the dominating recombination mechanism expressed by A and J_0 , the thin film solar cell must be well-behaved in the measurement range. That is, it needs to be described completely by the basic diode model 3.2 with the parameters R , G , and J_L independent of voltage.

For analyzing whether the cell is well-behaved, a detailed procedure is explained in [10].

3.1.3 JV cell measurement setup

JV characterizations performed in the course of this work were measured at the Austrian Institute of Technology (AIT) in Vienna, Austria and at the Ångström Solar Center of the Uppsala University in Uppsala, Sweden. Both setups follow the principles of a typical JV test stand explained in the previous section and in figure 3.4.

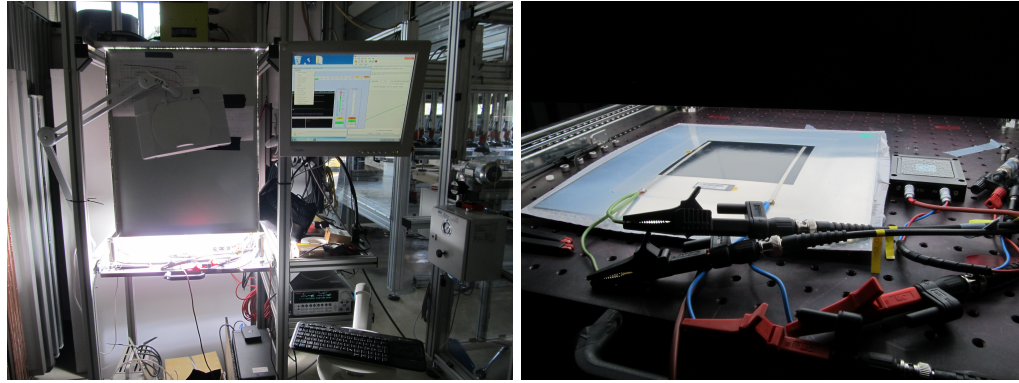


FIGURE 3.6: Measurement test stand for JV characterization at the Austrian Institute of Technology.

In the measurement setup in Uppsala (figure 3.5) a halogen lamp illuminates the test plane at 100 W/m^2 . The lamp height is adjustable and after a 30 minute lamp warm up the lamp height is set before each measurement session by comparing the output current of a reference cell. A shutter can be placed between the light source and the test plane in order to prevent the cell from heating up or from light soaking prior to a measurement.

In the test plane, the cell is placed onto a piezo electric cooler, which is controlled by a temperature probe underneath the cell. Different from figure 3.4, the electric contacts with two tips each both connect to the cell from the front and enable a 4-point measurement. The signal is then recorded by a data logger and processed by a computer application. Light and dark JV curves can be measured with this test setup.

The AIT setup is very similar to the Uppsala setup, however, a dimmable mercury lamp is used as a solar simulator. Dimming the lamp is the main mechanism for adjusting the output to provide a uniform and constant illumination in the test plane, while it does not affect the lamp spectrum significantly within a given dimming range. The cooling block for the cell, which stabilizes the cell temperature by water cooling, rests on the retractable test plane. Another cell for reference can be placed next to the device under test on the testplane to numerically adjust for lamp fluctuations in every measurement point. Contacting the cell from the back through the cooling block as well as with 4-point needles and other pin designs from the front allows for testing a wide variety of cell sizes and designs. Figure 3.6 shows the solar simulator for JV characterizations at the Austrian Institute of Technology, where light and dark JV curves can be measured.

For another set of JV characterizations, an ICVT test stand at Uppsala University was used. The test stand (figure 3.7) enables JV or CV measurements at different temperatures with the aid of a liquid nitrogen cooled cryostat. For the experiments conducted in the course of this work, JV measurements were conducted at room temperature only.

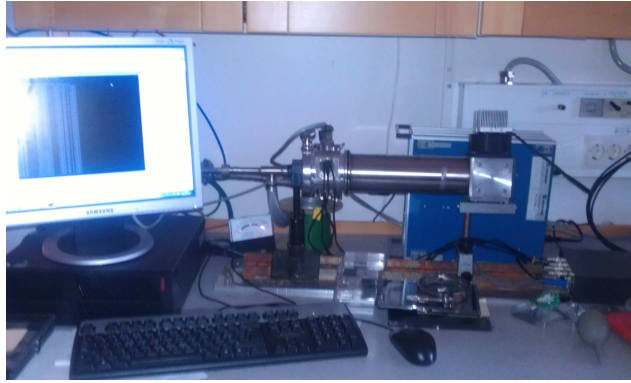


FIGURE 3.7: Measurement test stand with cryostat for ICVT characterization at the Ångström Solar Center in Uppsala.

Four different LED lights serve as light source for the solar simulator in the spectral ranges of red, green, blue and white. While light from single LEDs does not offer a spectrum close to that of sunlight, and hence does not qualify for standardized cell characterization, it can yield valuable insights when investigating light soaking effects exhibited by the cells. Figure 3.8 shows the spectrum of the LED light sources in the ICVT setup in comparison with the AM1.5 solar spectrum.

3.2 Module characterization according to IEC standards

The need for accurate solar module characterization is industry and market driven, where on the one hand, a reliable power classification of solar devices is needed for PV system design and on the other hand it is required for realistic energy yield predictions, which are the ultimate basis for investment cost and return calculations. A few percent difference in power rating easily translate into significant amounts of money when considering multi-megawatt PV installations.

For this reason, testing procedures for solar modules have been agreed on in international standards. These allow certified laboratories to conduct measurements for power ratings which also include other device aspects such as safety and aging for instance. Throughout Europe and many other parts of the world, IEC standards are applied and define design qualification and type approval for crystalline silicon PV modules (61215)[98] and for thin-film PV modules (61646)[99] among many other aspects.

Characterizing photovoltaic modules follows the same principles as characterizing individual cells, however, the handling of modules requires special testing equipment.

Testing PV modules mainly focuses on measuring the basic parameters V_{oc} , I_{sc} , and

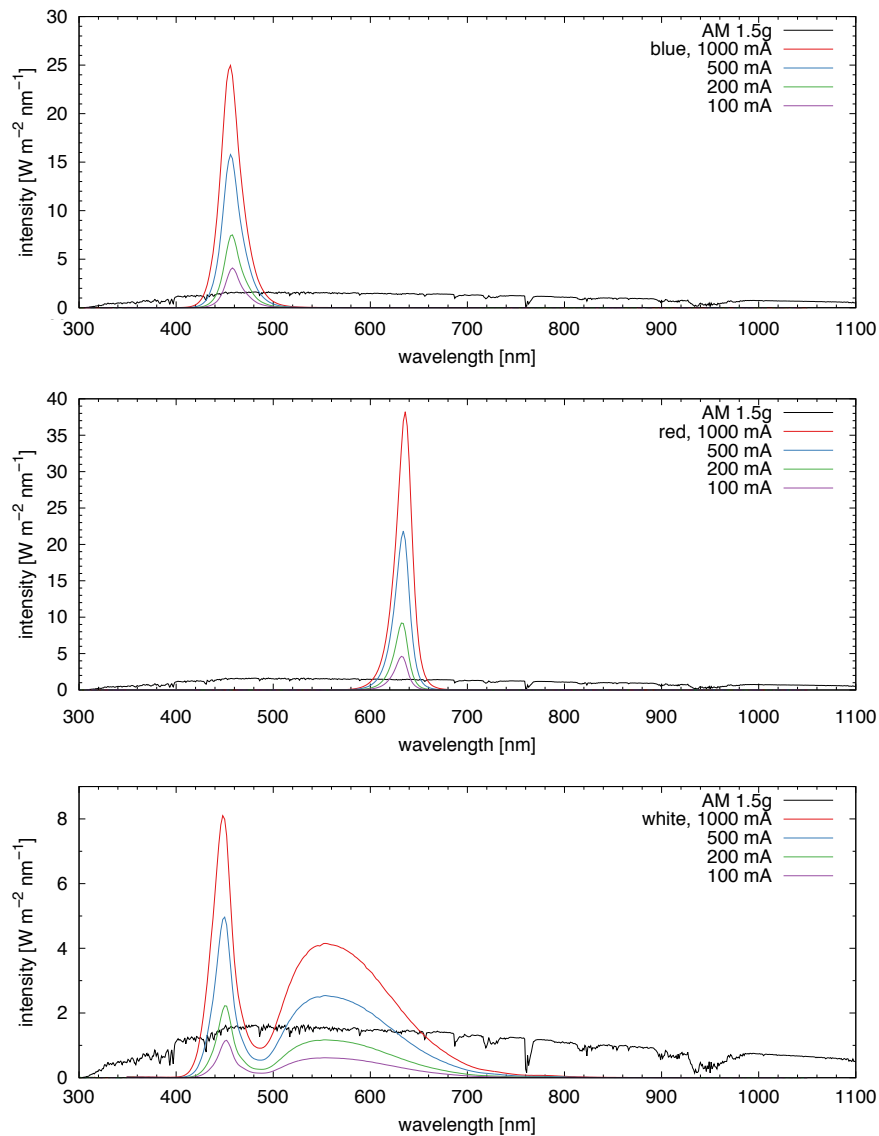


FIGURE 3.8: Intensity spectrum of blue, red and white LED light sources in the ICVT measurement setup in comparison to the AM1.5 solar spectrum. The intensity is shown for different lamp power settings with 1000 mA lamp current being equivalent to 100%.

voltage and current output at the maximum power point V_{mp} , I_{mp} ¹, which are needed to calculate FF, η and the maximum power output P_{mp} . The value in analyzing electrical module parameters lies in statements about the overall module quality and energy yield predictions, rather than in material characteristics. Fortunately, the same analysis method as in cell JV curve characterization can be applied to modules in a straight forward fashion.

Figure 3.9 gives an overview of the testing procedure following the international standard IEC 61646 for thin film PV modules. The procedure is finalized with a light soaking step

¹When referring to cells, oftentimes the quantity J for current density is used for material comparability, whereas modules are typically characterized by their total current output I , giving more practical information for applications. In this work, the notion J will be used for cells and I for modules.

Thin-film terrestrial photovoltaic (PV) modules - Design qualification and type approval

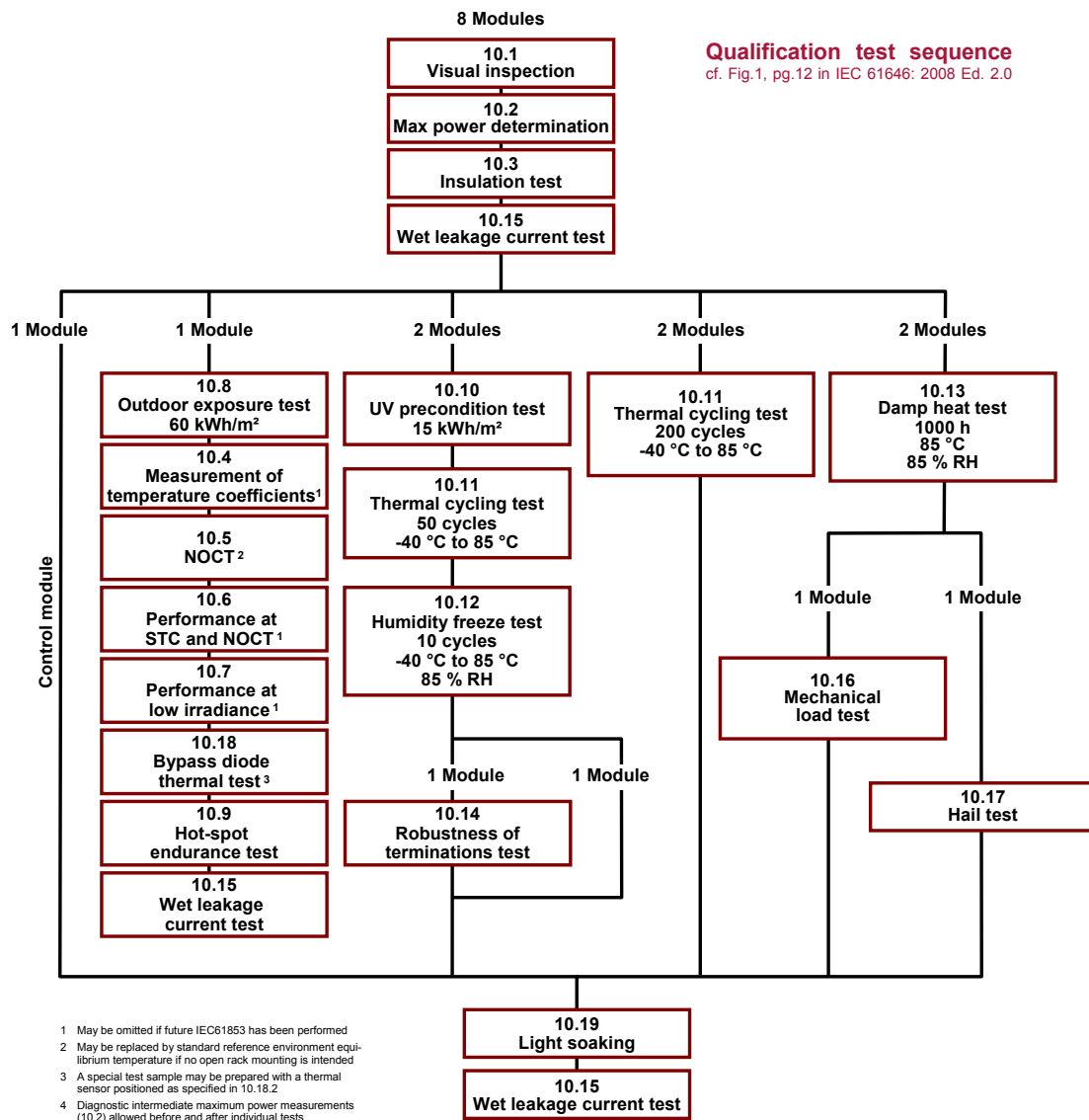


FIGURE 3.9: Overview of the IEC 61646 international standard for thin-film terrestrial PV modules - design and type approval.

with the purpose of stabilizing electrical characteristics of the module. During illumination the module is connected to a resistive load keeping it close to the maximum power point. Natural sunlight or a solar simulator of class CCC or higher can be used as light source. When using a solar simulator, the irradiation must be kept between 600 W/m^2 and 1000 W/m^2 at a module temperature of $50 \text{ }^\circ\text{C} \pm 10 \text{ }^\circ\text{C}$. If the maximum module power meets the criterion $(P_{max} - P_{min})/P_{average} < 2\%$ after two consecutive soaking periods of 43 kWh/m^2 accumulated irradiation energy, the module is considered to be electrically stabilized.

In the way it is stated, the standard is optimized to account for long-term illumination effects occurring in amorphous silicon modules. In the first hundred hours of illumination, a-Si:H modules exhibit a decline in performance, which can be explained by the Staebler-Wronski effect [5]. Not only do a-Si:H modules deteriorate in performance, they can recover to initial states after a heat treatment. In field installations parts of this effect has been observed during summer months, when modules typically operate at a much higher temperature [100]. Staebler and Wronski explain this effect with the break-up of hydrogenated dangling bonds in the silicon crystal by illumination and subsequent hydrogenation through thermal treatment [101].

However, the Staebler-Wronski effect, which sometimes is also referred to as "metastable effect" in literature, does not apply to chalcogenide solar cells. The electrical metastabilities dealt with in this work are of different origin (see chapter 2) and hence require different characterization handling for cells and modules.

Unfortunately, the IEC standard does not specify the exact duration of illumination and is not very precise by defining the spectrum as class C, which allows for $-60/+100\%$ of spectral mismatch in six relevant wavelength intervals according to IEC 60904-9 [102]. The most critical limitation of the IEC standards for chalcogenide PV module characterization, however, is the lack of a timeframe between light soaking treatments and subsequent performance measurements. These insufficiencies have led to varying performance characterizations of $\pm 6\%$ done at a round robin test with CIGS modules among Europe's leading PV test facilities.

The internationally certified PV testing facility at the Austrian Institute of Technology provides all necessary equipment to characterize modules according to these standards. Two of these test stands were also used for the experiments conducted in course of this work and shall be explained in a little more detail.

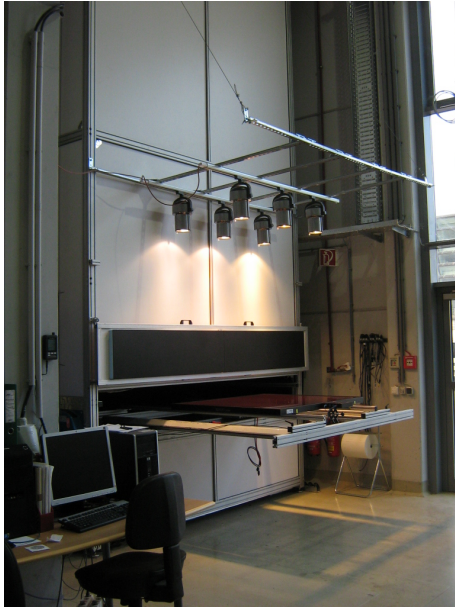


FIGURE 3.10: AIT flasher test stand. The flasher light is positioned above the module pane inside the flasher housing. Modules and the reference cell are placed on the sliding drawer. In front of the flasher, a light array is mounted for pre-treatment and light soaking.

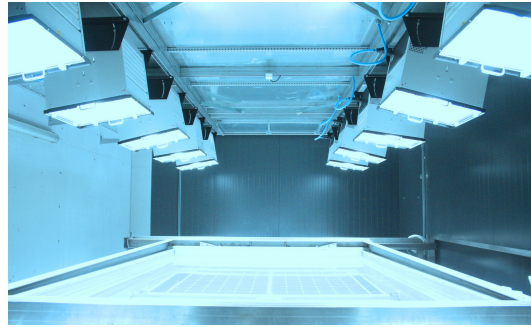


FIGURE 3.11: AIT static sun simulator.

3.2.1 I-V flasher

The flasher is a pulsed solar simulator with a pulse duration of a few milliseconds. It can be used for characterizing modules as well as cells. The flash intensity can be set to 1000 W/m^2 , altogether reaching a AAA class according to IEC standard 60904-9 [102], considering spectral match, spatial irradiance uniformity and temporal stability. For temperature control, the internal space of the test stand can be air conditioned to $25 \text{ }^\circ\text{C}$, providing the required environment for standardized module characterization.

The device under test is placed on a horizontal sliding drawer together with the reference cell. This makes handling fairly easy and enables quick switching between pre-treatment and characterization, as can be seen in figure 3.10. Depending on characterization requirements, the electronic load type can be chosen individually and connected to the cell or module in 4 points for a separate voltage and current signal.

On the outside of the flasher housing a low-light halogen lamp array is installed for pre-treatment purposes. Homogeneity in the module pane is realized within a range of $\pm 5\%$ at an irradiance of 50 W/m^2 , which was confirmed with a CM21 pyranometer.

3.2.2 Static solar simulator

Used primarily for stabilizing modules according to IEC 61646 [99], the static sun simulator at the AIT consists of a lamp array of ten halogen light sources creating a static illumination of up to 1000 W/m^2 with a class B spectrum [102] in the $3 \times 4 \text{ m}$ test pane. This test pane is separated from the lamp array by a glass plate ensuring temperature control for the modules and the reference cell in a range of $+10 \text{ }^\circ\text{C}$ and $+65 \text{ }^\circ\text{C}$.

This setup allows for in situ light soaking and characterization of modules, making it possible to observe the effect of illumination over time. Due to the size and warm up phases of the simulator, it is, however, not possible to change the irradiance between soaking and characterization periods.

3.2.3 Electronic load

For I-V characterizations, the cells and modules are connected to an electronic load. In most cases, a Pasan or Keithley electronic load was used for modules and small cells respectively. The I-V characteristic are measured by imposing a voltage ramp to the device under test while it is exposed to illumination (flash of $> 10 \text{ ms}$ or static light). The voltage was typically applied in forward direction.

The software of both electronic loads can correct the measured results for variances in irradiance and temperature.

3.3 Record of module metastabilities

Thus far, only a few studies have addressed the issue of short-term metastable effects in commercial chalcogenide photovoltaic modules. Gostein and Dunn contrast the differences in metastable effects between various thin film technologies including amorphous silicon [103, 104]. While phenomena occurring in a-Si modules can mainly be ascribed to the Staebler-Wronski effect, metastabilities in chalcogenides follow other mechanisms. The reviewed transient effects in CdTe modules range from performance shifts upon light exposure or forward bias within a time frame of a few hours to both efficiency improvements and losses after about 1000 hours of light exposure [89]. These differences in behavior are explained by variances in the fabrication processes. In CIGS modules, the findings are focused on a general improvement of devices efficiencies after light exposure, however, differences due to the light wavelength are noted. Also, inconsistencies in findings regarding both performance improvements and degradations due to light exposure are mentioned. For both chalcogenide technologies, elevated temperatures are noted to accelerate the metastable changes. The review [104] furthermore raises the necessity for

a preconditioning procedure prior to device characterization.

A study by NREL [105] explores current preconditioning procedures and presents experimental data for CdTe and CIGS under different light soaking conditions and forward bias. The importance of a short time between pretreatment light exposure and characterization is stressed.

Forward biasing as an alternative method to light soaking as a preconditioning procedure is put forward by NREL [54] and others [106], however, the equivalency of effects caused by forward bias compared to light exposure is not necessarily given and needs further investigation (see section 2.3.4).

Chapter 4

Metastable Effects in Cu(In,Ga)Se₂ Cells

Metastable behavior of CIGS cells is described in literature, however, the experimental observations are difficult to compare. The exact material structure regarding layer materials, thicknesses and quality defines the impact on the metastable behavior of the cells. Therefore it is almost impossible to derive the proper physical mechanisms in a universal way, especially from cells with different material properties.

This challenge was the motivation to create samples in a defined way with only few material changes for observing metastabilities. The cells were fabricated at Ångström Solar Center in an inline co-evaporation process according to the baseline procedure [107].

For this study, two different sets of comparison cells were made: a CdS/ZnSnO set from the first absorber batch and a CdS/Zn(O,S) set from the second absorber batch. Initially, they were planned all from the same absorber batch, however, the cells with the Zn(O,S) buffer layer from the first batch show low performance. In order to compare cells with high quality and efficiency, a second absorber batch was then made for the Zn(O,S) cells, together with a CdS reference sample.

Preparation of samples Soda-lime glass serves as substrate for the cells. The molybdenum back contact is deposited by DC sputtering before the CIGS absorber is grown. In an inline co-evaporation system at a deposition temperature of 520 °C, a ratio of $[Cu]/([Ga]+[In]) = 0.90$ and a built-in $[Ga]/([Ga]+[In])$ gradient from 0.25 at the front to 0.65 towards the back of the cell is established. The atomic concentrations across the layer can be found in figure 4.1. It shows a SIMS depth profile of a typical CIGS absorber prepared according to the Ångström Solar Center baseline process.

Layer	Deposition method	Typical thickness [nm]
Mo back contact	DC sputtering	350
CIGS absorber	Co-evaporation	1700
CdS buffer layer	Chemical bath deposition	50
ZnSnO buffer layer	Atomic layer deposition	13
Zn(O,S) buffer layer	Atomic layer deposition	20
i-ZnO	RF-sputtering	90
ZnO:Al front contact	RF-sputtering	350
Ni/Al/Ni grid	Evaporation	3000

TABLE 4.1: Structure of a CIGS cell stack prepared according to the baseline process at the Ångström Solar Center [107].

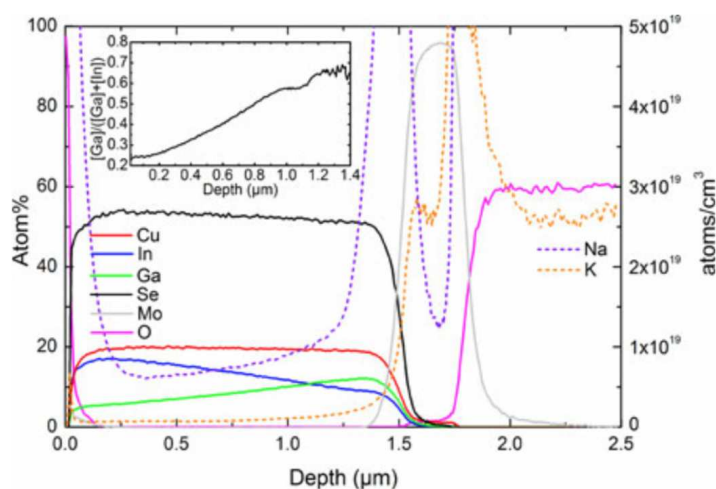


FIGURE 4.1: SIMS depth profile over an Ångström Solar Center baseline device. The profile covers the CIGS absorber layer, the back contact and part of the glass substrate. Na and K are labeled on the right axis, while Cu, In, Ga, Se, Mo, and O are referenced on the left axis. Used with kind permission of the authors of [107].

Shortly after the absorber buildup, the buffer layer is deposited. Cells from the same absorber batch were taken to apply two different kinds of buffer layers for metastability comparison. The standard samples got a CdS buffer layer of 50 nm, applied by chemical bath deposition (CBD). For the samples with the alternative¹ buffer layers were applied by atomic layer deposition (ALD). In the first absorber batch set, a Zn_{1-x}Sn_xO_y buffer layer was added. It has a thickness of 13±5 nm and a [Sn]/([Zn]+[Sn]) ratio of 0.15-0.20 [108]. In the second batch set, the buffer layer Zn(O,S) was applied by ALD according to the procedures of [109] and [110].

For all cells, the front contact is deposited with an RF sputtering system. First, a non-doped ZnO layer (i-ZnO) is sputtered onto the buffer layer, then the front contact is finished with a Al-doped ZnO layer (ZnO:Al).

¹Alternative buffer layers are considered cadmium-free layers in order to compose cells made from solely non-toxic materials.

Finally, a metal grid is applied by evaporation before the cells are separated into 0.5 cm² sizes using mechanical scribing. An overview of the CIGS cell stack including typical layer thicknesses are listed in table 4.1.

The metastable behavior of these cells is described in the following section 4.1. In the second part of the chapter, in section 4.2, another cell series is investigated. All cells in the second series have the same buffer layer material ZnSnO, but vary in the thickness of this buffer layer. Growth was controlled by the number of ALD cycles and yielded thicknesses of approximately 30-342 nm. A detailed description of the sample preparation and the material characterization is given in [108].

Experiment overview The initial cell characterization of the samples as well as all light soaking and dark relaxation runs for CIGS cells are listed in an overview in Appendix A.

For the changes between illumination times and JV sweeps, the in situ setup described in section 3.1.3 was very practical. Without moving the cell, an illumination period was interrupted only for the duration of the sweep, which lasted for approximately 5 seconds each time. After an initial characterization, the beginning of each light soaking cycle started with a 9 s illumination period, followed by 5 s sweep, then 9 s illumination,... After two minutes, the illumination period was increased to 35 s, then 5 s sweep, etc.... The illumination period was ultimately increased to 15 min. The increased spacing of the sweeps allowed for more data points in the beginning of illumination, when most of the changes occur.

Illumination interval	Duration (approx.)
9 s	2 min
35 s	9 min
5 min	2:30 h
15 min	> 6:00 h

TABLE 4.2: Light soaking illumination intervals in between *JV* characterizations.

4.1 Influence of the buffer layer material

The buffer layer is suspected to influence light soaking and metastable behavior of CIGS cells, which is elaborated in section 2.4.3. In this section the results from light soaking experiments for cells with the buffer layer materials CdS, ZnSnO and Zn(O,S) are shown. The cells were illuminated and characterized in situ with the ICVT test stand described in section 3.1.3 at a constant temperature of 300 K and an intensity of 1 sun equivalent

J_{sc} . Because some metastable changes occur quickly within the first few seconds, the illumination intervals are chosen to increase according to table 4.2.

4.1.1 CdS, ZnSnO and Zn(O,S) buffer layers in CIGS cells: white light soaking under open circuit conditions

Figure 4.2 shows the response of V_{oc} and FF to white light soaking of cells with CdS, ZnSnO and Zn(O,S) buffer layers respectively. While the CdS and Zn(O,S) cells perform much better in the initial state with a higher V_{oc} and FF , they are also more stable than the ZnSnO cell, which exhibits a massive V_{oc} drop of more than 14% (table 4.5). Only the CdS and ZnSnO cells show a spike of the FF in the first few seconds. In the CdS cell, the FF increases by 0.5% in the first 27 s. The JV measurements after that show a slight decrease resulting in a FF slightly below the initial measurement.

In the ZnSnO cell the observed FF spike is much higher and lasts longer. For the first 100 s, the FF increases by 4.3% before it starts dropping, but stays above the initial FF at the end of the light soaking period. Even though the J_{sc} is subject to small fluctuations caused by the light source in all light soaking experiments, the nature of the FF change cannot be attributed to J_{sc} or lamp inhomogeneities.

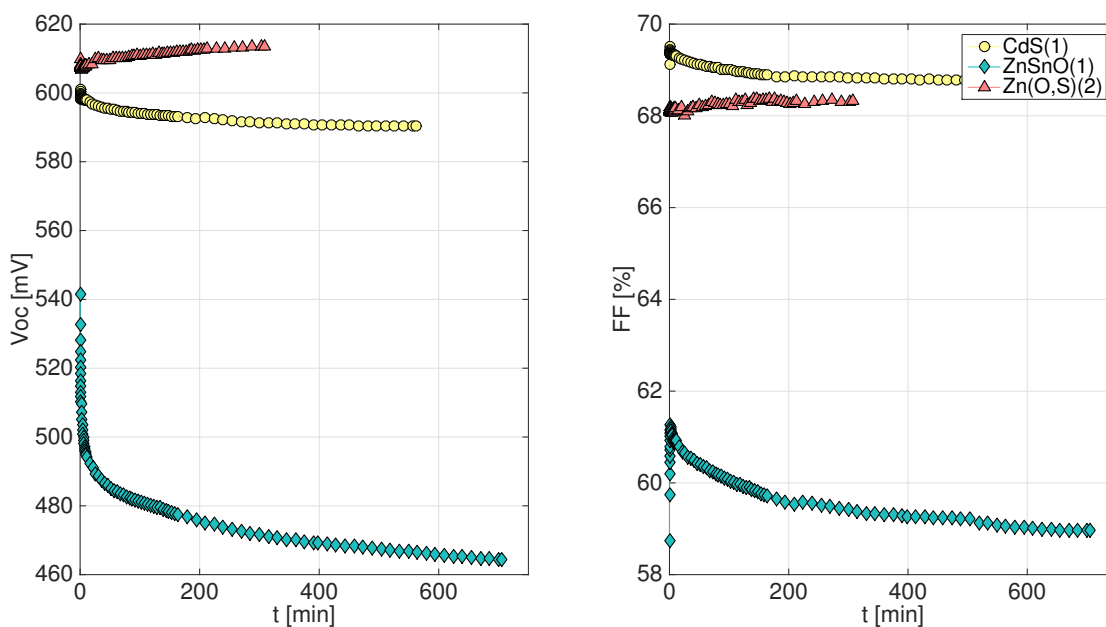


FIGURE 4.2: White light soaking for CIGS cells with CdS, ZnSnO and Zn(S,O) buffer layers. The number in brackets represents the absorber batch. During illumination, cells were kept under open circuit conditions.

Sample	CdS 9111-6313A1-01	ZnSnO 9098-1363A1-01	Zn(O,S) 9485C-07
illumination bias conditions		white light soaking open circuit	
duration [h:min]	9:21	11:45	5:08
initial V_{oc} [mV]	601.1	541.6	609.8
final V_{oc} [%]	98.2	85.8	100.6
initial FF [%]	69.1	58.7	68.1
final FF [%]	99.5	100.4	100.3

TABLE 4.3: Results: CdS, ZnSnO, Zn(O,S) buffer layers in CIGS cells, white light soaking. Final V_{oc} and FF percentages are relative to the respective initial values.

4.1.2 CdS, ZnSnO, Zn(O,S) buffer layers in CIGS cells: dark relaxation

Following the light soaking in the previous section, the cells were left inside the ICVT measurement device in darkness. Light- JV characterizations were performed after the same time intervals as described in table 4.2. The sweep duration of the measurement setup could not be reduced below approximately 1.5 s, in which time the cells were again exposed to light. Regardless, a relaxation behavior (figure 4.3) can be observed, which shows, that the previous light soaking resulted in a metastable effect. For the V_{oc} of the ZnSnO cell, the metastable effect appears to be reversible, even though the final V_{oc} value is well below the initial V_{oc} (table 4.4). The trend does not show a saturation after

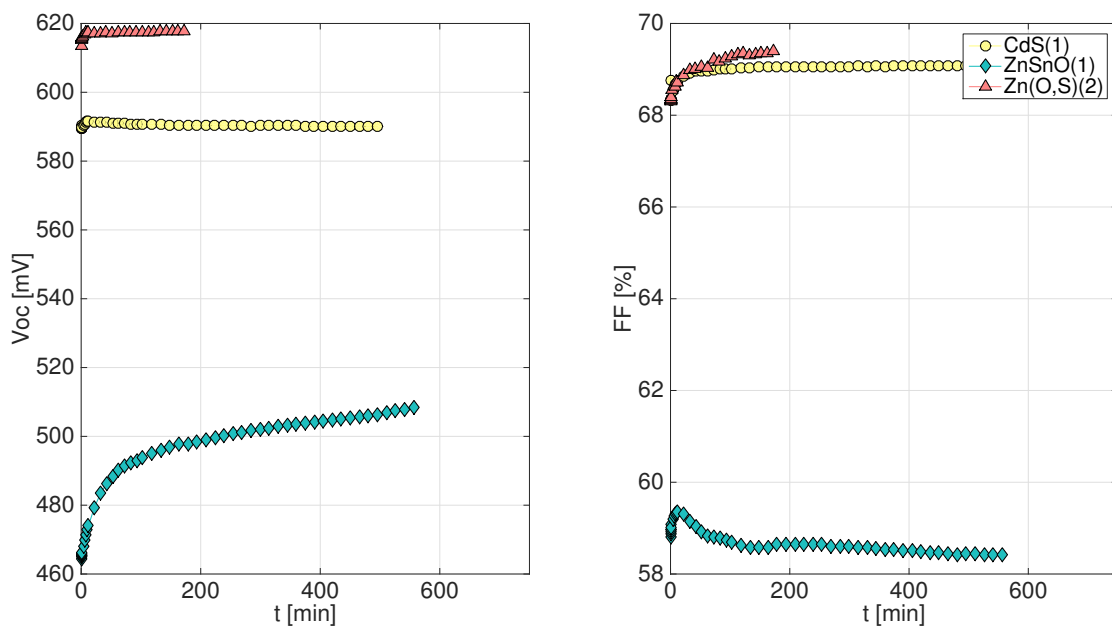


FIGURE 4.3: Dark relaxation for CIGS cells with CdS, ZnSnO and Zn(S,O) buffer layers. The number in brackets represents the absorber batch.

Sample	CdS 9111-6313A1-01	ZnSnO 9098-1363A1-01	Zn(O,S) 9485C-07
illumination		dark relaxation	
bias conditions		open circuit	
duration [h:min]	8:15	9:16	2:52
final V_{oc} [%]	98.2	93.9	101.3
final FF [%]	100.0	99.5	101.9

TABLE 4.4: Results: CdS, ZnSnO, Zn(O,S) dark relaxation, final V_{oc} and FF percentages are relative to the respective initial values before the light soaking period (table 4.5).

9:16 h, so it can be assumed that the V_{oc} will improve further. The FF of the ZnSnO cells starts off slightly above the initial value, increases for 12 minutes of dark relaxation before it starts dropping. At the final measurement, the FF lies at 99.5 % slightly below the initial value. It is possible, that the short sweep intervals for JV characterizations in the first minutes have an influence on the FF behavior.

For the CdS and the Zn(O,S) cells, the observations are a little bit less conclusive. The CdS cell V_{oc} remains rather constant throughout the dark relaxation, while the Zn(O,S) V_{oc} improves further in the first 8 minutes. Both cells improve in their FF . The CdS cell returns to the initial FF before light soaking, while the Zn(O,S) cell exceeds the initial FF by 1.9 %.

4.1.3 CdS buffer layer in CIGS cells: white, red and blue light soaking

In figure 4.4 light soaking behavior under different spectral wavelengths for CdS buffer layer cells can be seen. The spectral band of the used LED lights can be found in figure 3.8 in chapter 3. During red light soaking, the JV characteristics were also performed with red light. This was done in order to prevent any influence from the energetically

Sample	CdS 9111-6313A1-01	CdS 9267A-01	CdS 9267B-25
illumination	white LS	blue LS	red LS
bias conditions		open circuit	
duration [h:min]	9:21	05:07	5:08
initial V_{oc} [mV]	601.1	649.9	685.4
final V_{oc} [%]	98.2	98.7	98.7
initial FF [%]	69.1	68.7	72.5
final FF [%]	99.5	98.7	102.0

TABLE 4.5: Results: CdS buffer layer in CIGS cells, white, blue and red light soaking. Final V_{oc} and FF percentages are relative to the respective initial values.

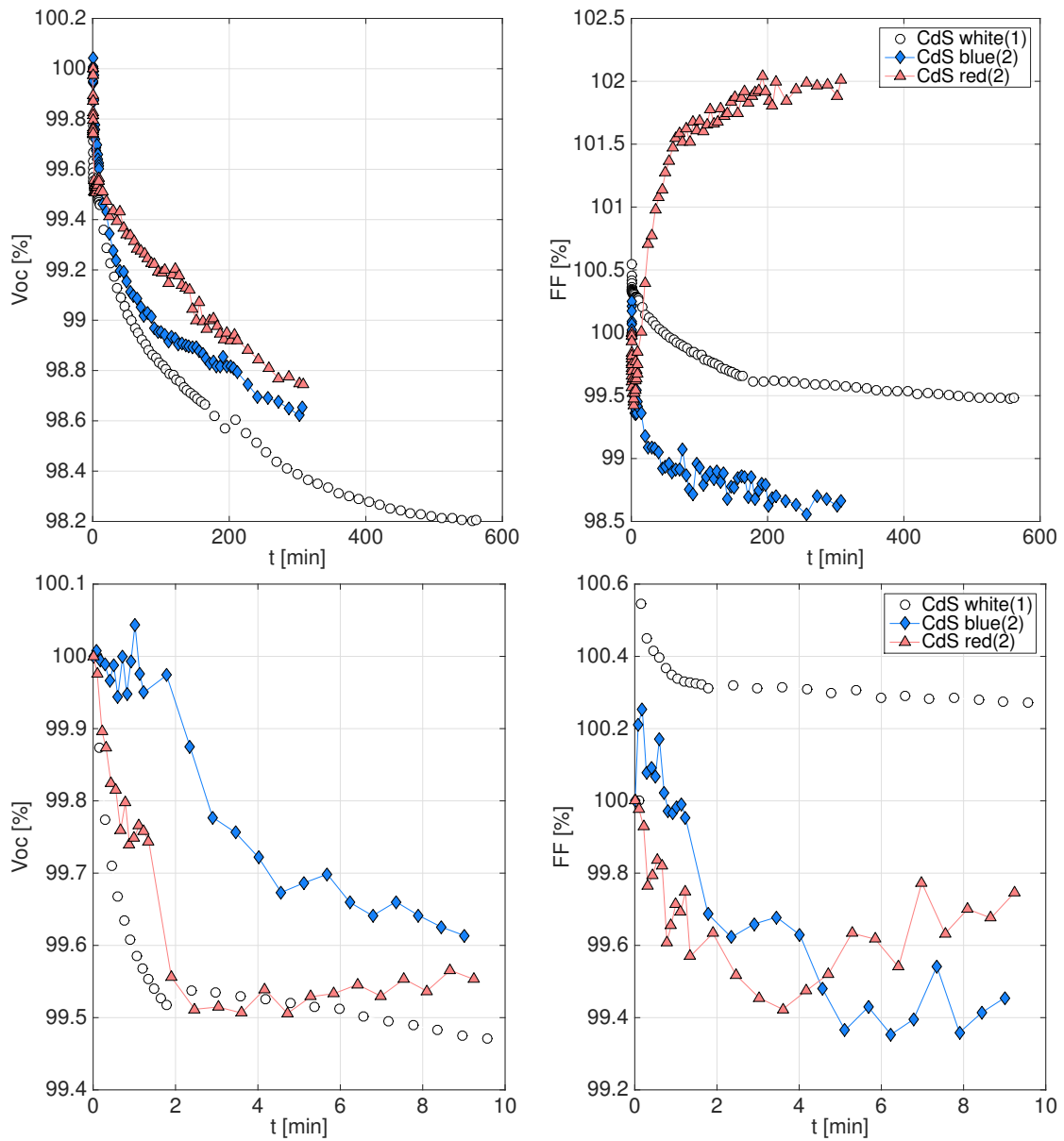


FIGURE 4.4: White, blue and red light soaking for CdS buffer layer cells. The bottom graphs show enlarged the first 10 minutes of the light soaking period. The number in brackets represents the absorber batch.

higher wavelengths.

Different spectral wavelengths do not seem to have a fundamentally different influence on the V_{oc} of the CdS cells. The V_{oc} drops for illumination with white, blue and red LEDs. While the magnitudes are slightly different, the overall loss is below 2 % for all measurements (table 4.5) and demonstrates again the stability of CdS buffer layer cells. The FF , however, shows a different picture. The white and blue lines exhibit the same downwards trend with different magnitudes, while the FF improves by 2 % after light soaking with red light. At a closer look at only the first 10 minutes of illumination in the bottom two figures 4.4 it becomes evident, that the cells behave very similar in

the beginning. This could be a hint of two competing effects with different time scales. Under red light soaking, a different mechanism is dominating in the longer time scale, than under white and blue light soaking.

4.1.4 ZnSnO buffer layer in CIGS cells: white, red and blue light soaking

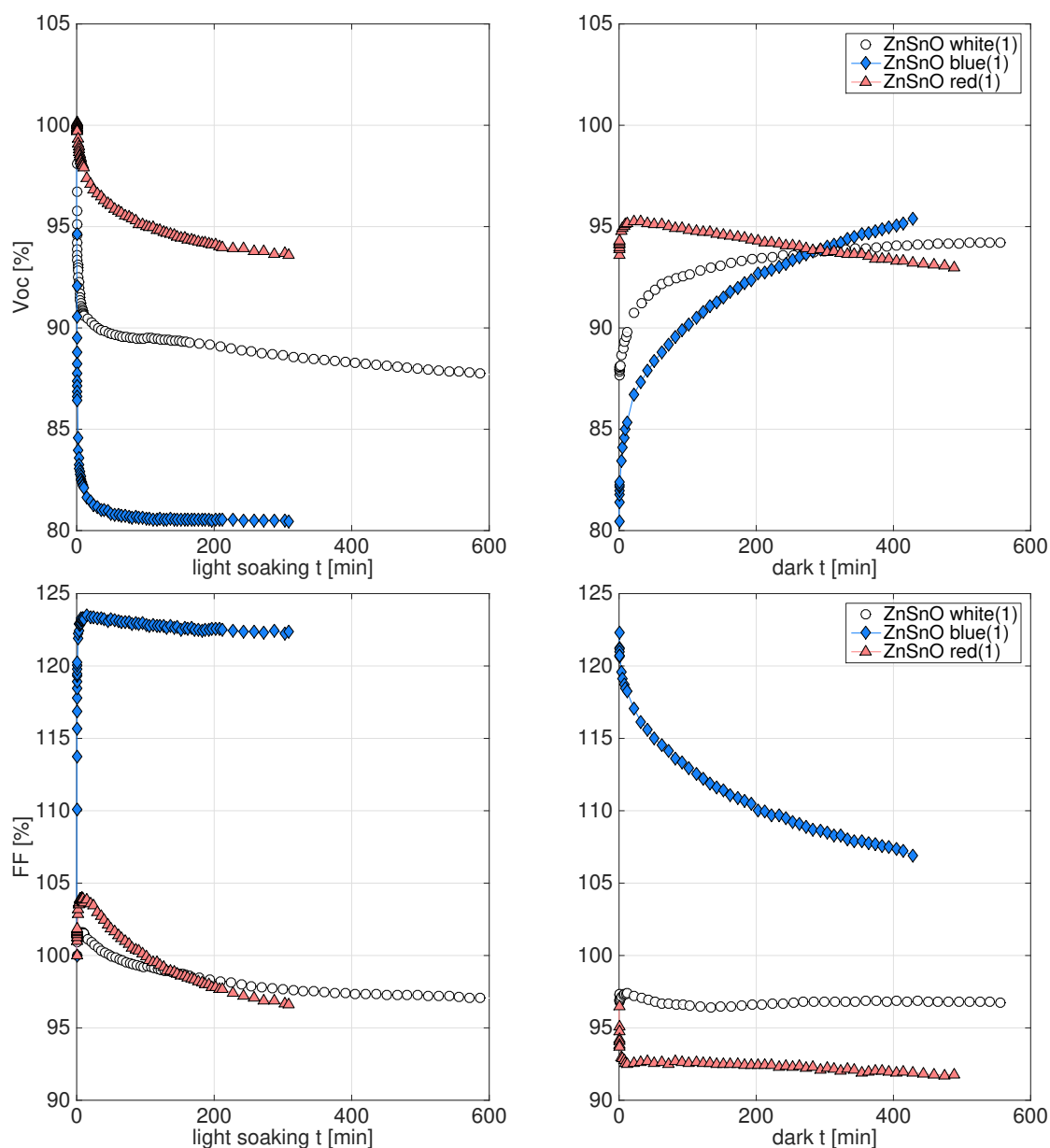


FIGURE 4.5: White, blue and red light soaking for ZnSnO buffer layer CIGS cells. The top plots show the V_{oc} under light soaking (left) and for the subsequent dark relaxation (right). The bottom plots show the FF for light soaking and dark relaxation. The number in brackets represents the absorber batch.

The ZnSnO buffer layer cells all stem from the same absorber batch, however, at the time of blue and red light soaking, the respective cell had already suffered from some

deterioration, given the very low initial FF .

As can be seen in figure 4.5 the V_{oc} drops for white, blue and red light soaking, with the largest and fastest decrease by 19.5 % under blue light and the smallest and slowest by 6.4 % under red light (compare table 4.6). For the first 21 minutes dark relaxation, all cells recover their V_{oc} at a fast rate. While the formerly blue and white illuminated cells keep improving, the red illuminated cell V_{oc} starts dropping again. It is noteworthy, that the JV characterizations for white and blue runs were done with a white LED, but for the red light soaking and dark relaxation, the red LED was also used as light source for the JV characterization. None of the cells recover their V_{oc} back to the initial value in the given dark relaxation time.

In the FF , all curves show an initial increase. The FF maximum for under white and red illumination is reached after 7-8 minutes, under blue illumination after 14 minutes. Afterwards the FF drops in all cases, however, under blue illumination it remains above 122 % of the initial value, while under white and red, the FF falls below the initial value.

After the light soaking period, the formerly white illuminated FF remains at that level. The blue and red, however, are subject to further loss. While the dark relaxation for the red curve leads to a sharp drop in the first 5 minutes, the blue curve follows a softer exponential decay, where the bottom is not reached after the dark relaxation time of 7:09 hours.

Sample	ZnSnO 9098-1363B2-29	ZnSnO 9098-1363B2-25	ZnSnO 9098-1363B2-25
illumination bias conditions	white LS	blue LS open circuit	red LS
duration [h:min]	10:21	05:08	5:08
initial V_{oc} [mV]	531.2	604.2	576.6
final V_{oc} [%]	87.6	80.5	93.6
initial FF [%]	61.5	46.3	39.4
max. FF [%]	101.6	123.5	104.0
final FF [%]	97.0	122.4	96.6
illumination	dark relaxation		
duration [h:min]	9:16	7:09	8:09
final V_{oc} [%]	94.2	95.4	93.0
final FF [%]	96.8	107.0	91.9

TABLE 4.6: Results: ZnSnO buffer layer CIGS cells, white, blue and red light soaking. Final V_{oc} and max. and final FF percentages are relative to the respective initial values before light soaking.

4.1.5 Zn(O,S) buffer layer CIGS cells: white, red and blue light soaking

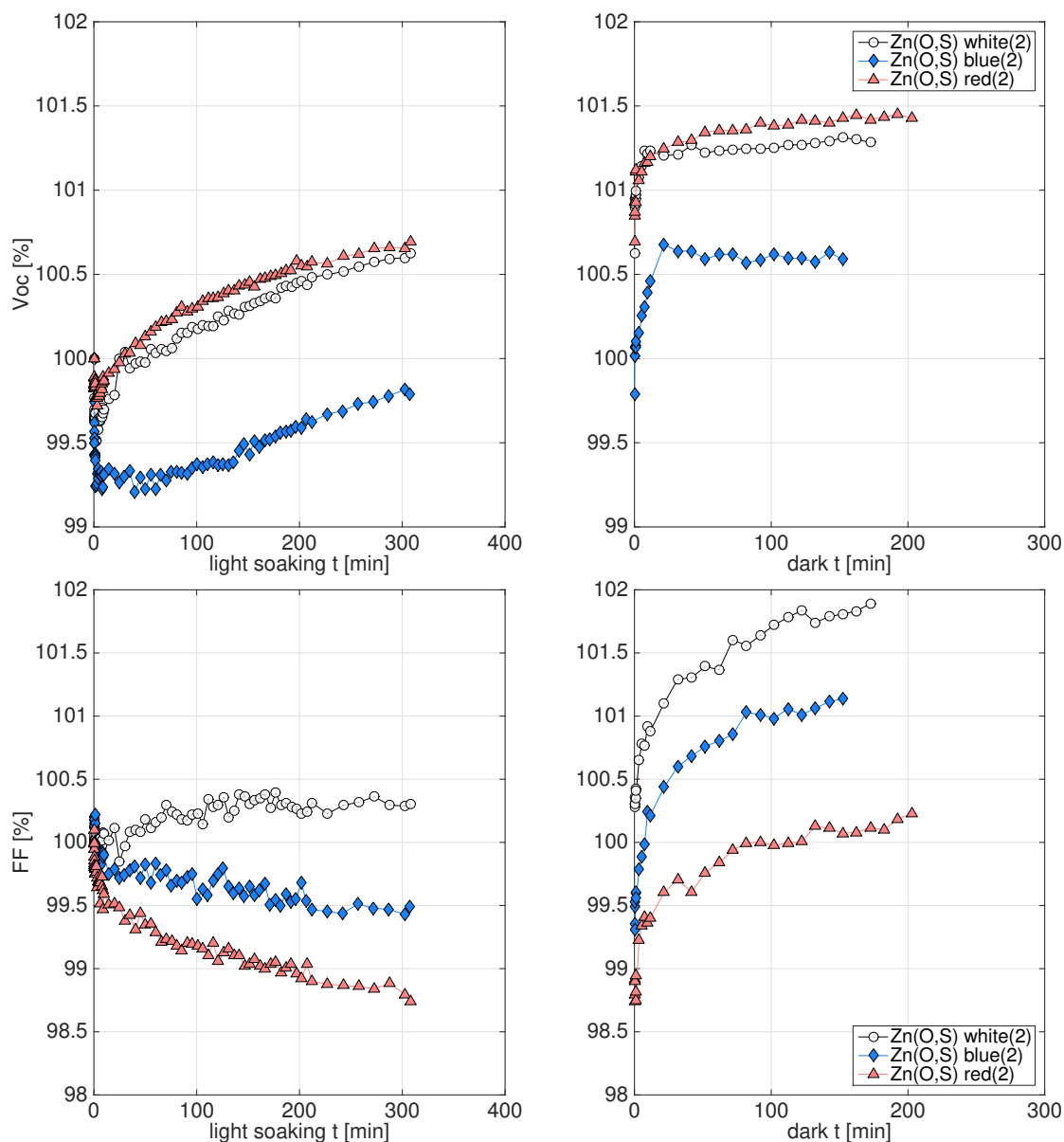


FIGURE 4.6: White, blue and red light soaking for Zn(O,S) buffer layer CIGS cells. The top plots show the V_{oc} under light soaking (left) and for the subsequent dark relaxation (right). The bottom plots show the FF for light soaking and dark relaxation. The number in brackets represents the absorber batch.

The Zn(O,S) buffer layer cells are of good quality (refer to table 4.7) and show again a different light soaking behavior for different colored light sources, different from the previous cell types. The top left plot in figure 4.6 shows an increase in the V_{oc} , with white and red light yielding the highest increase. However, a closer look at the first 10 minutes of illumination in figure 4.7 reveals, that all cells initially drop in V_{oc} . While the V_{oc} under blue light soaking does not reach the initial level after 5:08 hours of illumination,

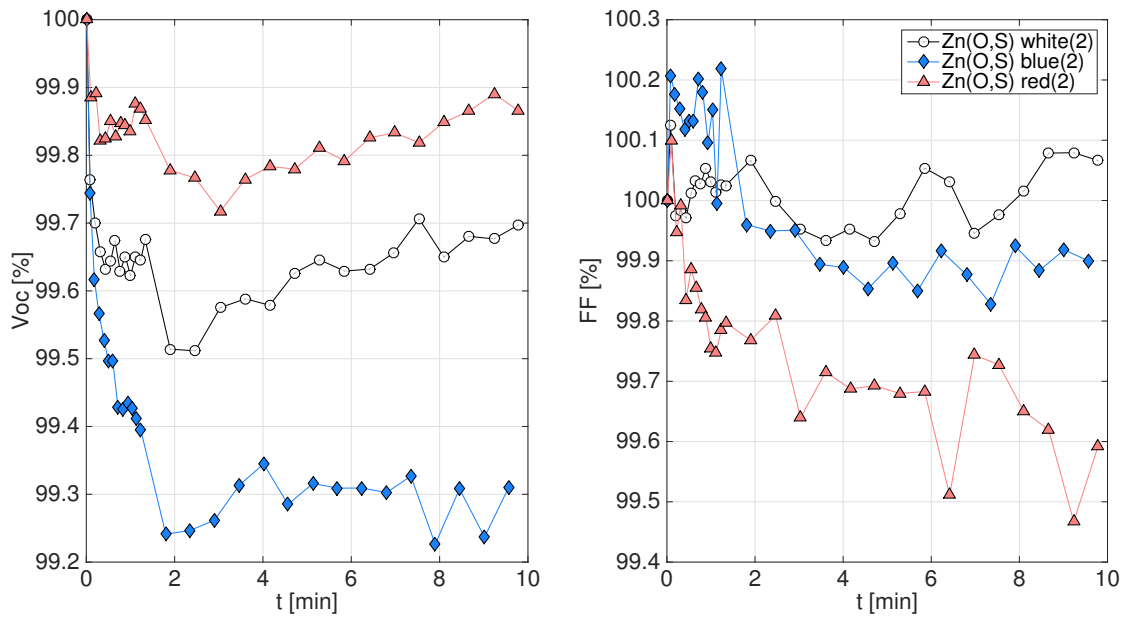


FIGURE 4.7: $\text{Zn}(\text{O,S})$ buffer layer CIGS cells white, blue and red light soaking for the first 10 min.

Sample	$\text{Zn}(\text{O,S})$ 9485C-07	$\text{Zn}(\text{O,S})$ 9485A-01	$\text{Zn}(\text{O,S})$ 9485B-25
illumination	white LS	blue LS	red LS
bias conditions	open circuit		
duration [h:min]	5:08	05:07	5:08
initial V_{oc} [mV]	609.8	604.0	623.0
final V_{oc} [%]	100.6	99.8	100.7
initial FF [%]	68.1	68.7	67.9
max. FF [%]	100.1	100.2	100.1
final FF [%]	100.3	99.5	98.7
illumination	dark relaxation		
duration [h:min]	2:52	2:32	3:23
final V_{oc} [%]	101.3	100.6	101.4
final FF [%]	101.9	101.1	100.2

TABLE 4.7: Results: $\text{Zn}(\text{O,S})$ buffer layer CIGS cells, white, blue and red light soaking. Final V_{oc} and max. and final FF percentages are relative to the respective initial values before light soaking.

the white and red illumination yields a V_{oc} increase of 0.6 % and 0.7 % respectively. The subsequent dark relaxation phase leads to further increases in the V_{oc} , lifting all V_{oc} above the initial value before light soaking.

The FF behavior shows a slight decrease after the first few seconds, where all cells at first experience a small FF increase (see figure 4.7). Under white and red light soaking, the FF rises in the first 6 seconds, before it drops, under blue light soaking the decline commences after the first minute of illumination. During dark relaxation, all cells exhibit

an increase, yielding a higher FF at the end of the measurement than the initial values before illumination. The rate of recovery is, however, slightly lower than for the recovery of the V_{oc} .

4.1.6 CdS buffer layer CIGS cells: white light soaking under different circuit conditions

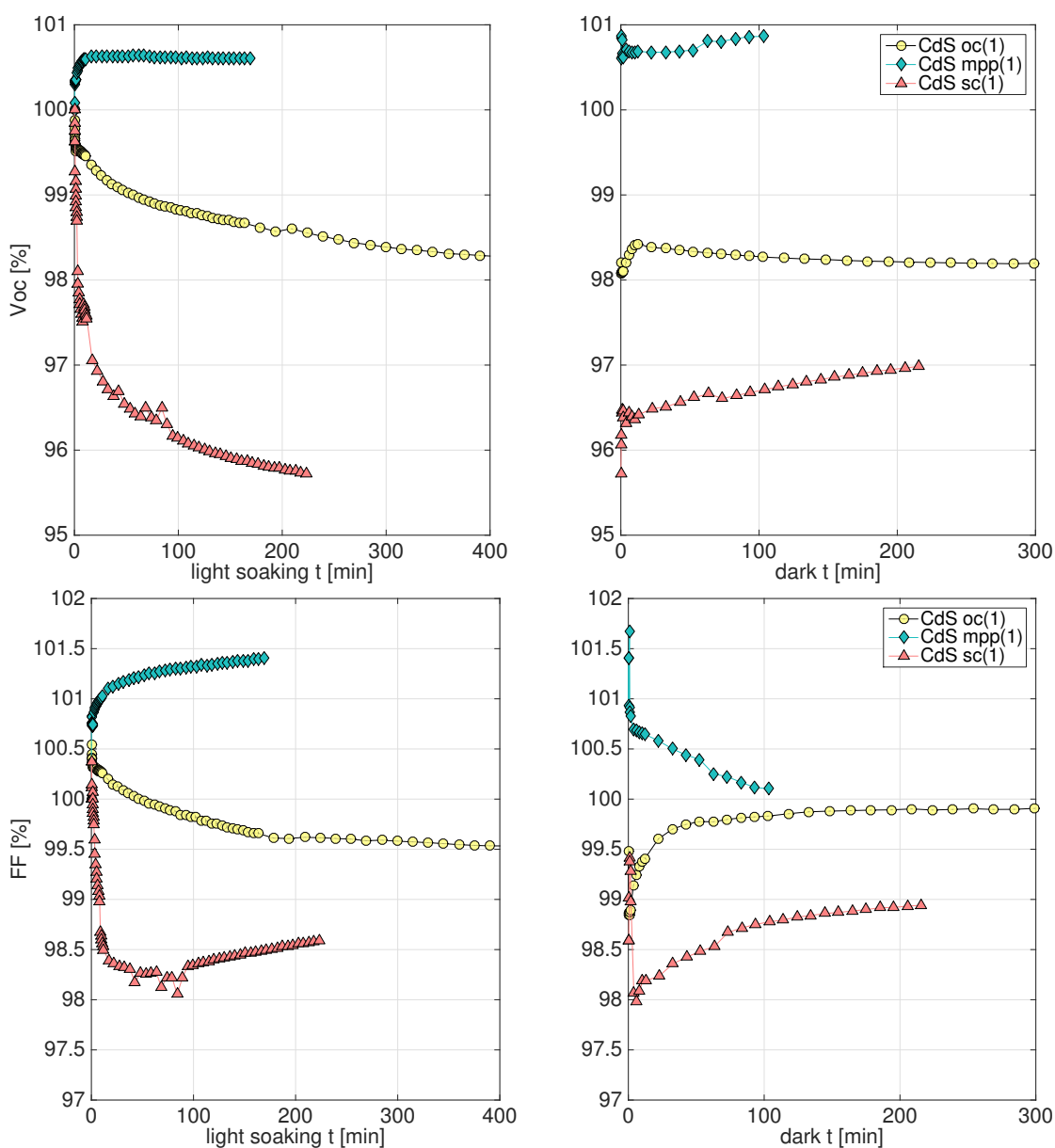


FIGURE 4.8: CdS buffer layer CIGS cells light soaking under OC, MPP and SC conditions. The top plots show the V_{oc} under light soaking (left) and for the subsequent dark relaxation (right). The bottom plots show the FF for light soaking and dark relaxation. The number in brackets represents the absorber batch.

Having in mind real operating conditions of solar cells, it is of interest how light soaking affects them under various bias conditions. Therefore, CdS (this section) and ZnSnO

Sample	CdS 9111-6313A1-01	CdS 9111-6313B2-32	CdS 9111-6363B2-32
illumination	white light soaking		
bias conditions	OC	500 mV	SC
duration [h:min]	9:21	2:49	3:43
initial V_{oc} [mV]	601.1	547.8	622.8
final V_{oc} [%]	98.2	100.6	95.7
initial FF [%]	69.1	67.0	71.9
max. FF [%]	100.5	101.4	100.4
final FF [%]	99.5	101.4	98.6
illumination	dark relaxation		
duration [h:min]	8:16	1:43	3:36
final V_{oc} [%]	98.2	100.9	97.0
final FF [%]	99.9	100.1	98.9

TABLE 4.8: Results: CdS buffer layer CIGS cells light soaking under OC, MPP and SC conditions. Final V_{oc} and max. and final FF percentages are relative to the respective initial values before light soaking.

(section 4.1.7) buffer layer cells were illuminated under open circuit (oc) conditions, short circuit (sc) conditions and under a forward bias close to the maximum power point (mpp). There was no power point tracking throughout the light soaking periods, so the bias in both short circuit and maximum power point state was not adapted to any change of the cell behavior.

After light soaking, the cells underwent a dark relaxation period under the same bias conditions as during their respective light soaking period.

Figure 4.8 shows the change in V_{oc} and FF for light soaking and dark relaxation for CdS buffer layer cells. As can be seen, metastable effects do not only occur under open circuit conditions, but can be even more pronounced under electrical bias. In this experimental run, the qualitative behavior of V_{oc} and FF show similarities. While the oc illuminated cell shows only a small drop in both characteristics (compare table 4.8), the sc cell drops more severely than the oc cell and the mpp cell experiences a rise in V_{oc} and FF .

During dark relaxation, all cells show the tendency to return to the initial values prior to light soaking in both V_{oc} and FF , with the exception of the mpp illuminated V_{oc} values, which seem to remain at the elevated level. This could hint to some permanent improvements to the cell, given that this light soaking run was also the first one of this sample.

4.1.7 ZnSnO buffer layer CIGS cells: white light soaking under different circuit conditions

Analogous to the previous section, ZnSnO buffer layer cells were illuminated under different bias conditions, as can be seen in figure 4.9. Here, all V_{oc} values drop heavily, with the illumination under oc conditions showing the smallest drop, and under sc conditions showing the largest drop down to 88.4 % of the initial V_{oc} , which can be compared with table 4.9.

During the subsequent dark relaxation period, all cells improve in their V_{oc} in a limited exponential growth curve, however, none of the cells recovers to the initial V_{oc} levels in the observed relaxation time, but rather indicate a limit below the initial V_{oc} .

For the FF , all cells exhibit an initial rise in the beginning. The FF under oc conditions improves by 1.6 % in the first 10 minutes, and under mpp conditions it improves by 4.1 % in the first 6 minutes of illumination. Afterwards, both these cells experience a drop in the FF , leaving the oc cell below the initial FF value after the light soaking phase and the mpp cell above the initial FF . The cell under sc conditions, however, shows the largest FF improvement without any drop. There, the FF rises by 15.2 % after the light soaking period.

During dark relaxation, the FF drops for the improved cells (mpp, sc) and remains rather stable for the cell under oc conditions.

Sample	ZnSnO 9098-1363B2-29	ZnSnO 9098-1363A2-25	ZnSnO 9098-1363B1-07
illumination	white light soaking		
circuit conditions	OC	500 mV	SC
duration [h:min]	10:22	3:40	2:49
initial V_{oc} [mV]	531.2	560.8	516.3
final V_{oc} [%]	87.6	88.4	85.7
initial FF [%]	61.5	60.9	53.9
max. FF [%]	101.6	104.1	115.2
final FF [%]	97.0	102.0	115.2
illumination	dark relaxation		
duration [h:min]	9:16	3:34	2:44
final V_{oc} [%]	94.2	93.5	93.4
final FF [%]	96.8	99.0	110.2

TABLE 4.9: Results: ZnSnO buffer layer CIGS cells light soaking under OC, MPP and SC conditions. Final V_{oc} and max. and final FF percentages are relative to the respective initial values before light soaking.

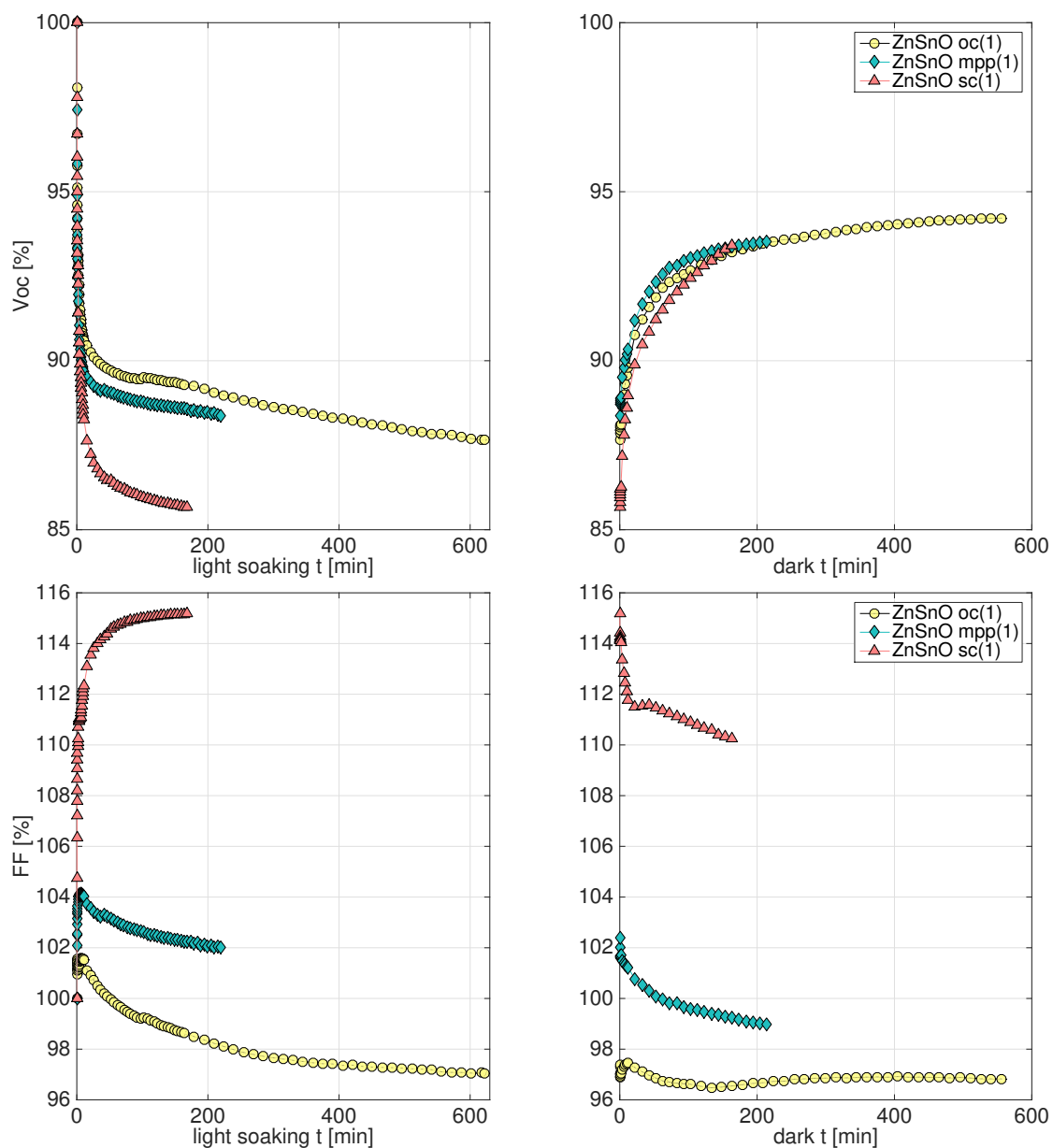


FIGURE 4.9: ZnSnO buffer layer CIGS cells light soaking under OC, MPP and SC conditions. The top plots show the V_{oc} under light soaking (left) and for the subsequent dark relaxation (right). The bottom plots show the FF for light soaking and dark relaxation. The number in brackets represents the absorber batch.

4.2 Metastability and buffer layer thicknesses

In order to further investigate the role of the buffer layer in metastable behavior, a series of cells only different in their buffer layer thickness was prepared according to [108]. The alternative buffer layer material ZnSnO was applied by variations of ALD cycles yielding buffer layer thicknesses of 13 nm, 30 nm, 76 nm, 165 nm and 342 nm. The layer thicknesses on the CIGS absorber was determined by transmission electron microscopy (TEM). The TEM images are shown in figure 4.10. By the time the cells were used for light soaking tests, the 13 nm cell had already deteriorated too much, which is why it was not included in this study.

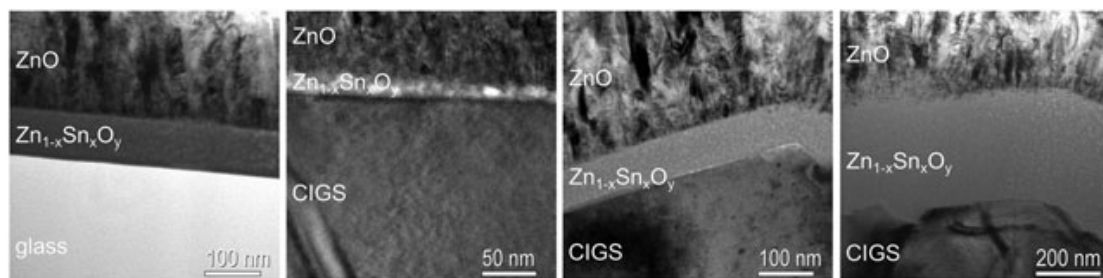


FIGURE 4.10: Bright field transmission electron microscopy images of ZnSnO buffer layers grown on a quartz glass substrate with 2000 cycles and grown on CIGS layers with 500, 2000 and 8000 cycles, respectively. Used with kind permission of the authors of [108].

4.2.1 ZnSnO buffer layer thickness: white, blue and red light soaking affecting V_{oc}

The ZnSnO buffer layer thickness series was illuminated with white, blue and red light. Figure 4.11 shows the evolution of the cells' V_{oc} under light soaking and subsequent dark relaxation. Under both white and red illumination, the V_{oc} drops and a correlation to the buffer layer thickness can be derived. For the cells with 30, 76 and 165 nm ZnSnO it can be seen, that the magnitude of the V_{oc} drop is directly proportional to the thickness. For the 342 nm cell, the drop happens slower and does not seem to have reached its plateau under either white or red light soaking. While under white light, the 342 nm V_{oc} results in the lowest relative V_{oc} after light soaking, it is possible, that under red light, the 342 nm V_{oc} will also drop below the 165 nm V_{oc} , given more light exposure time. Generally speaking, the magnitude of the V_{oc} drop is stronger under red light than under white, which can be compared with the V_{oc} values in table 4.10.

Under blue light, however, the V_{oc} experiences an overall increase after an initial drop in the first few minutes for the 30, 165 and 342 nm ZnSnO cells. Again, the thinner the ZnSnO layer, the better the V_{oc} outcome after light soaking. Only the 76 nm layer

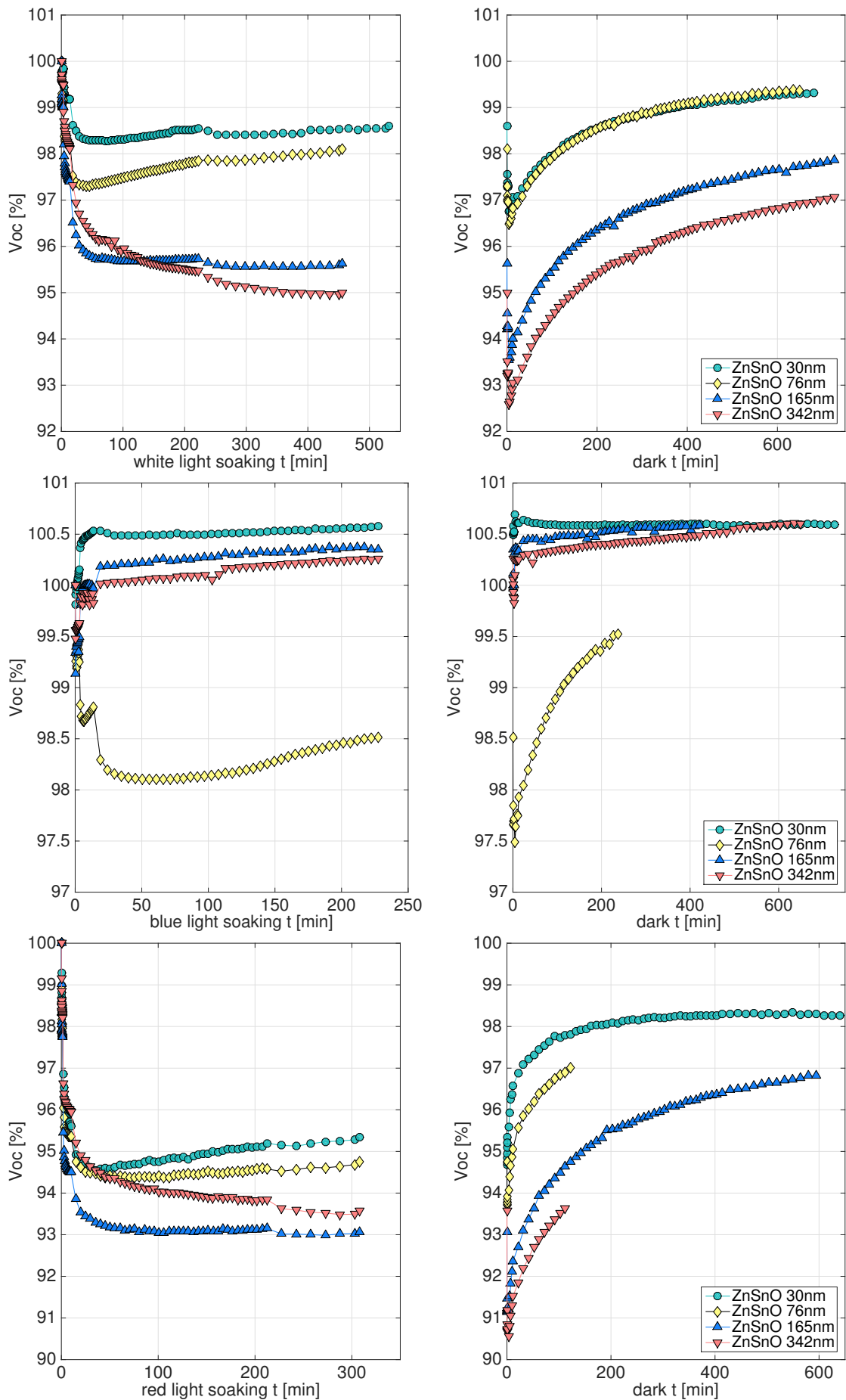


FIGURE 4.11: ZnSnO buffer layer thickness series: V_{oc} behavior under white (top), blue (middle) and red (bottom) light soaking and subsequent dark relaxation.

Sample	30nm ZnSnO 7850B2-14	76nm ZnSnO 7846B2-05	165nm ZnSnO 7844B2-14	342nm ZnSnO 7848B2-15
illumination	white light soaking			
circuit conditions	OC			
duration [h:min]	8:52	7:36	7:36	7:36
initial V_{oc} [mV]	639.0	627.1	621.2	604.9
final V_{oc} [%]	98.6	98.1	95.6	95.0
illumination	dark relaxation			
duration [h:min]	11:20	10:50	12:06	12:06
min. V_{oc} [%]	96.8	96.5	93.5	92.6
final V_{oc} [%]	99.3	99.4	97.9	97.1
illumination	blue light soaking			
circuit conditions	OC			
duration [h:min]	3:48	3:48	3:48	3:48
initial V_{oc} [mV]	634.9	633.7	610.2	590.1
final V_{oc} [%]	100.6	98.5	100.4	100.3
illumination	dark relaxation			
duration [h:min]	12:06	3:58	7:02	10:50
min. V_{oc} [%]	100.5	97.5	100.0	99.8
final V_{oc} [%]	100.6	99.5	100.6	100.6
illumination	red light soaking			
circuit conditions	OC			
duration [h:min]	5:08	5:08	5:08	5:08
initial V_{oc} [mV]	654.4	657.3	627.9	620.9
final V_{oc} [%]	95.3	94.7	93.0	93.6
illumination	dark relaxation			
duration [h:min]	11:55	2:02	9:54	1:52
min. V_{oc} [%]	94.7	93.7	91.1	90.6
final V_{oc} [%]	98.2	97.0	96.8	93.6

TABLE 4.10: Results: ZnSnO buffer layer thickness series. V_{oc} development for light soaking under white, blue and red illumination and subsequent dark relaxation. Minimum and final V_{oc} percentages are relative to the respective initial values before light soaking.

cell shows a contrary behavior by an overall decrease in the V_{oc} . After a drop in the first 6 minutes, the V_{oc} rises slightly for another 8 minutes, before it declines and only minimally recovers during light soaking after one hour. The light soaking run for this particular cell was redone and showed the same behavior trend. Therefore it must be assumed that the metastable mechanisms affect this cell differently from the others in the buffer layer thickness series.

Interestingly, in the first few seconds of dark relaxation, all V_{oc} values plunge, before they start a steady recovery following a limited growth characteristic. Overall, the V_{oc} recovers significantly after white and red light soaking periods for all ZnSnO layer thicknesses, although at slower rates than the respective light induced drops. This is also the case for the 76 nm cell under blue light soaking.

The cells experiencing an increase under blue light soaking roughly keep their V_{oc} levels throughout dark relaxation, 165 nm and 342 nm even rise further and remain above their original V_{oc} values after the dark relaxation periods.

4.2.2 ZnSnO buffer layer thickness: white, blue and red light soaking affecting the FF

Contrary to the V_{oc} behavior described in the last section, the FF development under white and red light soaking expresses a decreasing behavior, with the thinnest ZnSnO layers dropping the most (figure 4.12). Under white light soaking, all cells experience a swift FF increase, before dropping. For red light soaking, this is not observed, except for the 342 nm cell, which shows a strong increase by 8.6 % (compare table 4.11) in the first ten minutes, before the FF slowly declines to 106.9 % compared to the initial value. A low FF of 58.4 % in the initial measurement of the 342 nm cell before red light soaking could point to some cell damage and be the reason for the odd behavior.

Under blue light soaking, the FF behavior shows an initial small rise and a rather stable behavior thereafter, with the exception of the 76 nm cell, which drops to 98.3 % of the initial FF before light soaking. This cell already showed a different behavior in the V_{oc} under blue light.

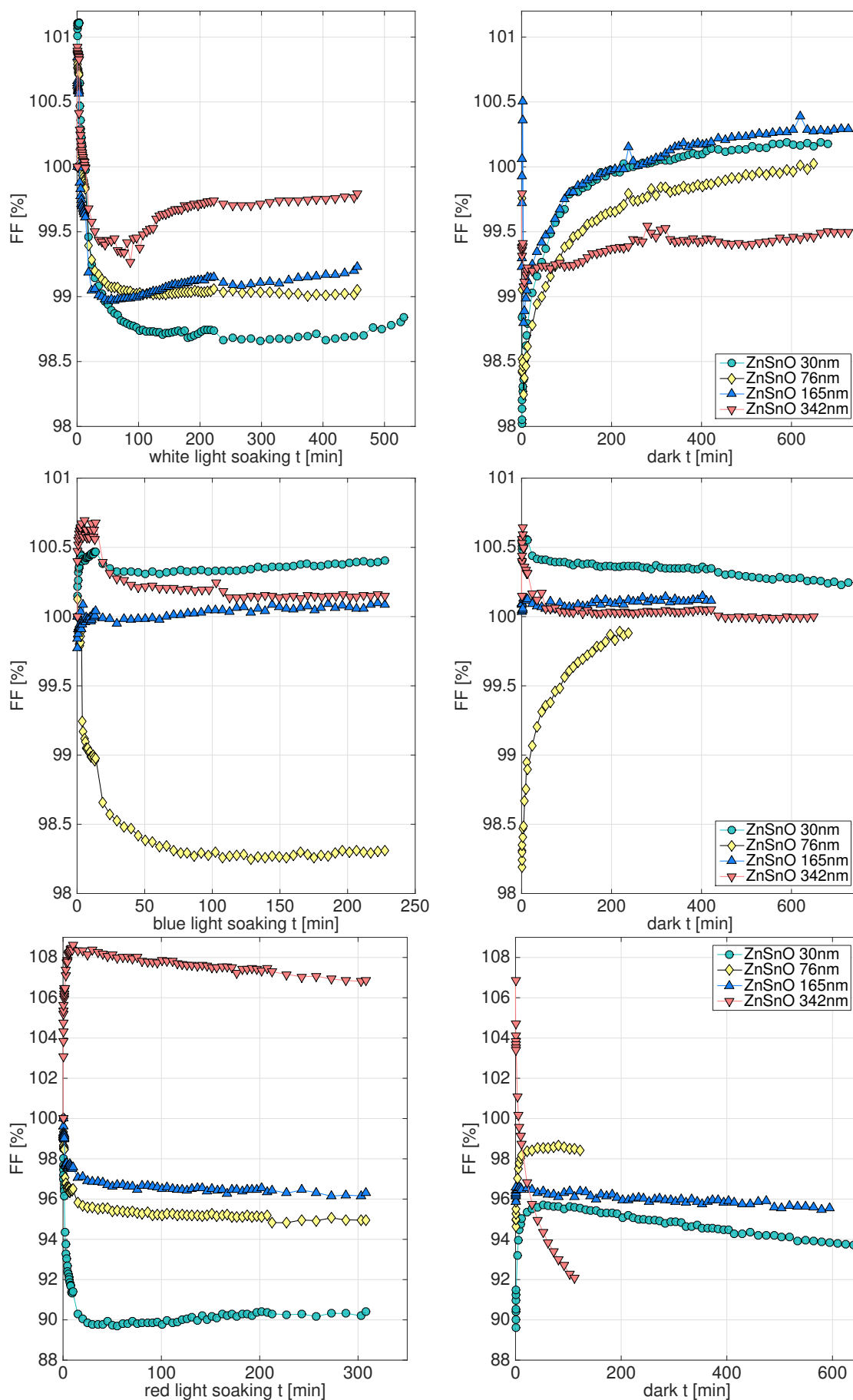


FIGURE 4.12: ZnSnO buffer layer thickness series: FF behavior under white (top), blue (middle) and red (bottom) light soaking and subsequent dark relaxation.

Sample	30nm ZnSnO 7850B2-14	76nm ZnSnO 7846B2-05	165nm ZnSnO 7844B2-14	342nm ZnSnO 7848B2-15
illumination	white light soaking			
circuit conditions	OC			
duration [h:min]	8:52	7:36	7:36	7:36
initial FF [%]	70.9	70.8	71.3	70.7
max. FF [%]	101.1	100.8	100.8	100.9
final FF [%]	98.8	99.1	99.2	99.8
illumination	dark relaxation			
duration [h:min]	11:20	10:50	12:06	12:06
final FF [%]	100.2	100.0	100.3	99.5
illumination	blue light soaking			
circuit conditions	OC			
duration [h:min]	3:48	3:48	3:48	3:48
initial FF [%]	71.2	71.8	72.1	70.8
max. FF [%]	100.5	100.1	100.1	100.7
final FF [%]	100.4	98.3	100.1	100.1
illumination	dark relaxation			
duration [h:min]	12:06	3:58	7:02	10:50
final FF [%]	100.2	99.9	100.1	100.0
illumination	red light soaking			
circuit conditions	OC			
duration [h:min]	5:08	5:08	5:08	5:08
initial FF [%]	62.4	67.5	69.0	58.4
max. FF [%]	100.0	100.0	100.0	108.6
final FF [%]	90.4	95.0	96.3	106.9
illumination	dark relaxation			
duration [h:min]	11:55	2:02	9:54	1:52
final FF [%]	93.5	98.4	95.6	92.1

TABLE 4.11: Results: ZnSnO buffer layer thickness series. FF development for light soaking under white, blue and red illumination and subsequent dark relaxation. Maximum and final FF percentages are relative to the respective initial values before light soaking.

4.3 CIGS cell reflectance spectroscopy

Measuring the reflectance of a cell reveals the optical losses of a photovoltaic device. In a spectrally resolved way, subtracting the reflectance curve and all collection losses leaves the quantum efficiency of a photovoltaic cell, as is explained in section 3.1.1 and 3.1.

The reflectance was determined for three CIGS cells with the buffer layers CdS, ZnSnO and Zn(O,S). This was done before light soaking in a relaxed state and immediately after light soaking. The spectrometer used is a Bruker Vertex 70 FTIR, a fourier-transform infrared spectrometer. For an immediate reflectance measurement after a light soaking period of 3 hours, the samples were transported and measurement was started within 5 minutes of the end of the light soaking period. The reflectance measurement itself could be done within a few minutes. For saving time between light soaking and reflectance measurement and for not disturbing the metastable state electrically, no current-voltage

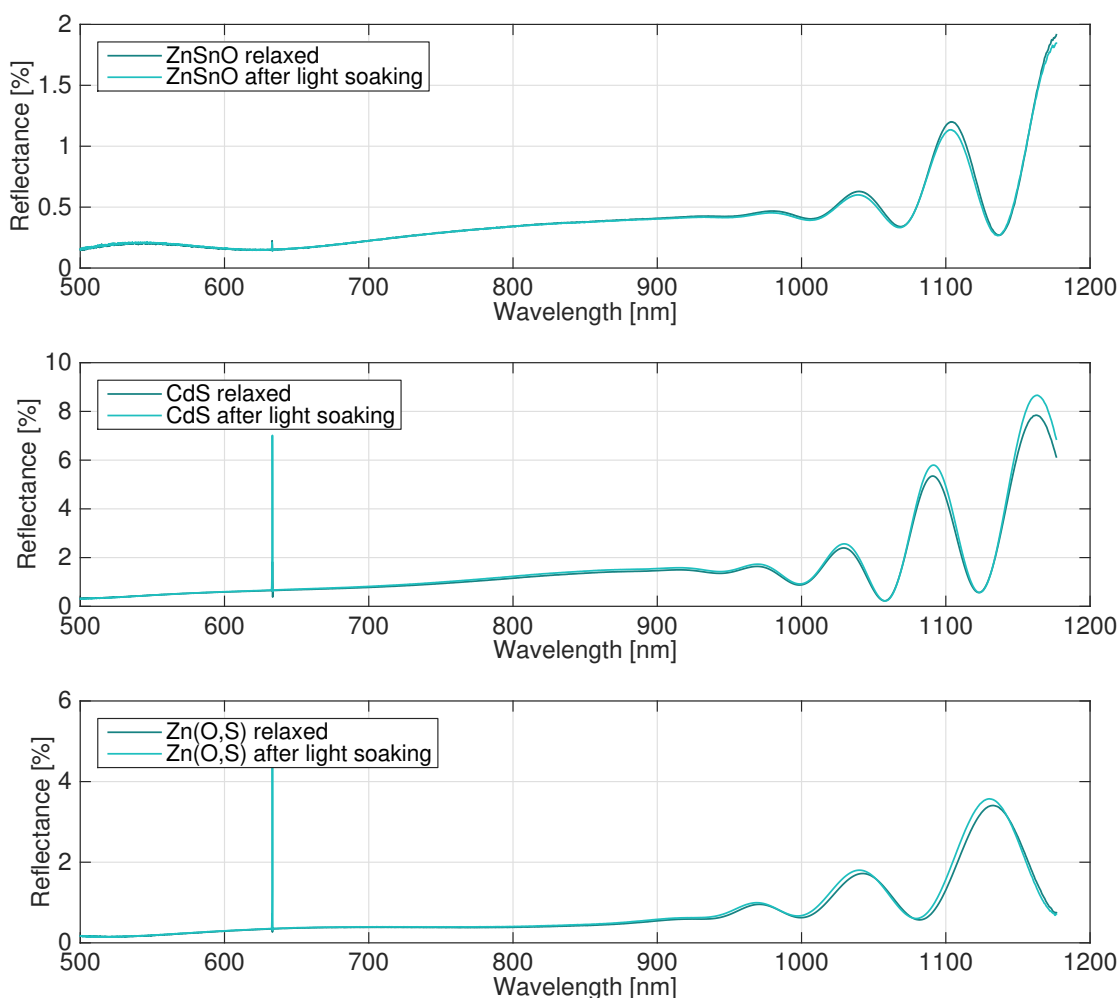


FIGURE 4.13: Spectrally resolved reflectance of CIGS cells with buffer layers ZnSnO, CdS and Zn(O,S) in a relaxed state and after light soaking.

characteristic was determined after light soaking. The results of the measured reflectance curves are shown in figure 4.13.

Unfortunately, the range of the measurement starts at 500 nm, leaving out the blue part of the visual spectrum and hence the band gap ranges of ZnSnO and Zn(O,S) at $E_g = 3.3 \text{ eV}$ [108] and $E_g = 2.7 - 3 \text{ eV}$ [111] respectively. The CdS band gap of $E_g = 2.4 - 2.5 \text{ eV}$ is at the border of the measured spectrum, however, no change in the reflectance curves can be observed in this area.

In the near-infrared section of the measured spectrum, interferences are visible. These interferences have been observed by other groups in similar device structures for reflectance [112] and also photoluminescence [113] in the NIR part of the spectrum. The interference occurs because of multiple reflections within the layer of a thin film device, before exiting the layer. According to [114], several requirements must be met for being able to observe interferences in thin-film photovoltaic devices: a smooth sample surface, high back reflectance, similar spectral range of layer thickness and photons, and weak absorption of photons when traveling through the absorber - all of which appear to be met with the used samples. The layer stack of the samples used for this study is described in the beginning of this chapter in table 4.1, with a typical absorber layer of 1700 nm.

As stated in [115], interference peaks in reflectance spectra match photoluminescence reflectance minima and vice versa. This is due to a $\lambda/2$ phase shift of the wave entering the device in reflectance measurements. This transition does not occur in photoluminescence, where the photons are generated within the absorber layer. The interferences can be simulated by optical modeling dating back to [116]. While modeling the photoluminescence interferences is more complex, interferences occurring in reflectance can generally be calculated by applying the transfer matrix method [115].

In the experiment of reflectance prior to and after light soaking, differences can be noticed in the NIR part of the spectrum for all buffer layer samples. Little surprisingly, the behavior among different buffer layer types shows to be quite different.

In the ZnSnO CIGS cell, the reflectance after light soaking is noticeably lower above 1000 nm. This means, for this spectral range, more photons are absorbed in the cell, leading to either photovoltaic conversion or collection losses. In the case of conversion, this could be translated into improved electrical parameters of the cell.

The CdS and Zn(O,S) cells, however, reflect more photons in the infrared spectrum after light soaking. This, in turn, has a detrimental effect on the conversion of incident photons.

With the numbers in 4.12, the trends in reflectance measurements and observations derived from IV curves can be compared. The measurements were done with cells from the same absorber batches, but unfortunately they could not be conducted with the very same cells. Because of relatively small change in the electrical parameters and the

differences in reflectance before and after light soaking, correlations can not be obtained directly and need to be established in future measurements.

Sample	CdS 9111-6313A1-01	ZnSnO 9098-1363A1-01	Zn(O,S) 9485C-07
illumination bias conditions		white light soaking open circuit	
duration [h:min]	9:21	11:45	5:08
initial V_{oc} [mV]	601.1	541.6	609.8
final V_{oc} [%]	98.2	85.8	100.6
initial FF [%]	69.1	58.7	68.1
final FF [%]	99.5	100.4	100.3
Sample	9111-6363A2-25	9098-1363B2-29	9485B-25
reflectance after light soaking	increased	decreased	increased

TABLE 4.12: CdS, ZnSnO, Zn(O,S) buffer layers in CIGS cells, white light soaking and trends in reflectance in cells with same buffer layer material. Final V_{oc} and FF percentages are relative to the respective initial values.

Chapter 5

Metastable Effects in Modules

The previous chapter showed that metastable behavior in CIGS solar cells is caused by material characteristics such as the absorber quality, the buffer layer material and its properties. This knowledge can be used to better understand metastable behavior, which also occurs in commercial thin film PV modules.

In this chapter, a collection of experimental results is gathered in order to verify these metastable effects in commercial thin film modules. Starting point for investigating metastable behavior in modules were the observed inconsistencies of characterization results. When measured according to the pre-treatment and characterization procedures given in the IEC standards (see 3.2), the same modules can exhibit a significant variation in the electrical output parameters. Therefore, a standardized module characterization is insufficient to describe the true performance of a thin film module, which shows metastable behavior.

Obviously, it is not known in the beginning, if a module exhibits a strong response to metastable triggers like light exposure or bias voltage. However, a sound characterization method should account for all kinds of metastable module behavior, because manufacturers rely on valid module characterization for their products' quality and customers require reliable data for their energy and revenue yield predictions.

5.1 Relaxed state

In order to measure metastable behavior in modules, it is necessary to determine an initial - or here also referred to as relaxed - state as a reference state of a module before light exposure. Since literature does not provide such information and relaxation times proved to be technology specific, the relaxation duration was determined for each module type individually.

For CdTe and also the a-Si modules used in these test series, the relaxation time was set to 12 h storage in darkness, under open circuit conditions and room temperature.

The investigated CIGS modules showed a much slower relaxation behavior. The relaxed state was reached slower than in the CdTe modules but also slower than in the CIGS cells from the previous chapter. Therefore, the dark relaxation period for CIGS modules was suggested to last for a minimum of two weeks of storage under the same conditions as mentioned before.

Before a light soaking experiment, the modules were covered while transferred to the test location and first exposed to light only with the initial I-V characterization before starting the light soaking cycle.

It should be stated that these relaxation times cannot be taken as representative durations for the respective material technology, not even within one material family, as the discrepancy between CIGS cells and modules shows. Rather, relaxation times should be determined for each module type individually, especially if manufacturing processes differ. For the limited number of test samples available for this study, the modules from the same manufacturer and same production batch showed to behave in the same time scales.

5.2 CdTe modules

CdTe solar cells were not part of the underlying cell study for metastabilities, however, CdTe solar devices can show metastable behavior just like CIGS based devices.

Three commercial CdTe specimen by First Solar Inc. were available for testing. The modules underwent initial characterization and stabilization according to IEC 61646 [99]. Their main parameters are shown in table 5.1 and can also be viewed in more detail in the data sheet in Appendix B.

Cell material	CdTe
Manufacturer	First Solar
Module type	FS-272
Number of cells	116
P_{mpp} [W]	72.5
V_{mpp} [V]	66.6
I_{mpp} [A]	1.09
V_{oc} [V]	88.7
I_{sc} [A]	1.23

TABLE 5.1: CdTe module specimen parameters at standard test conditions.

In addition, electroluminescence images of the modules were taken for visual inspection of the module quality, where some damages in the module structure can oftentimes be

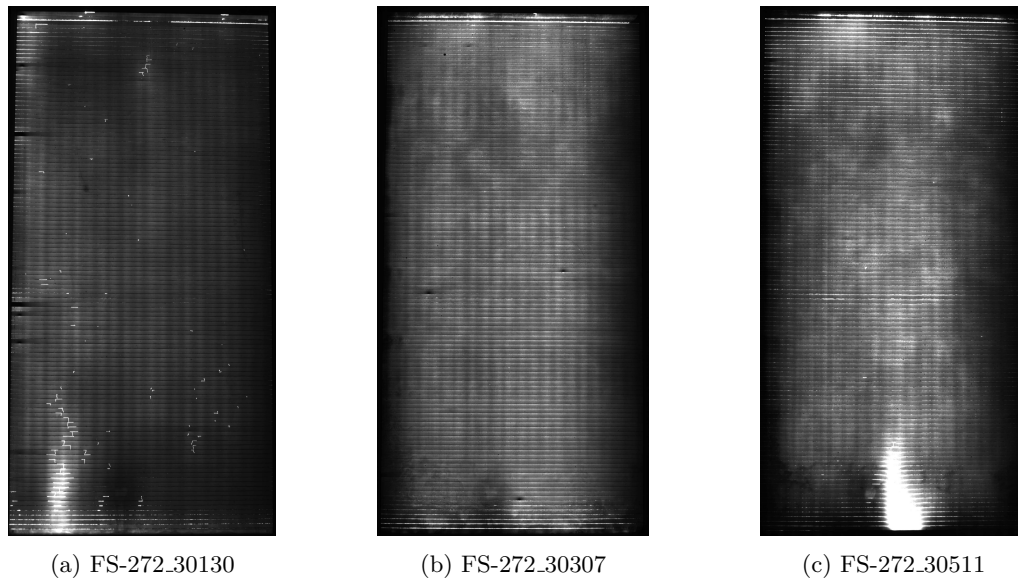


FIGURE 5.1: CdTe modules: Electroluminescence images of the untreated test devices.

noticed. While dark spots can be caused by improper contacts or poor cell performance, bright spots typically represent shunts [117]. Both of these effects lead to a reduced module efficiency and can be partly observed in the CdTe test modules in figure 5.1.

In order to correct for temperature deviations of module behavior, the temperature coefficients for current (α) and for voltage (β) for the CdTe modules were determined according to IEC 61646 [99] with $\alpha = 0.000492 \text{ AK}^{-1}$ and $\beta = -0.2218 \text{ VK}^{-1}$.

The following sections will show how these modules behave under and after various illumination and current treatments, which are referred to as light soaking and bias treatment respectively.

5.2.1 Forward bias treatment

To observe effects on the voltage, short circuit current in forward direction of $I_{sc} = 1.23 \text{ A}$ was applied to the CdTe modules while they were kept in the dark. The value for the current was chosen based on the data sheets for the modules (see Appendix B) and was fixed with a precision power supply, which was also used for in situ measuring of the voltage every 30 seconds. A drastic drop in voltage shown in figure 5.2 was the subsequent observation. During the entire procedure, the modules were kept completely dark and were not cooled, hence a significant increase in temperature from $20 \text{ }^\circ\text{C}$ to $47.5 \text{ }^\circ\text{C}$ was measured. To account for the influence of temperature on the module voltage, the voltage was corrected using the determined coefficients mentioned at the beginning of section 5.2.

The voltage drops were, however, only temporary. *IV* characterizations a week after the

treatment yielded the same parameters as before the short circuit current treatment. During this week the modules were "resting" in the dark and could therefore enter a relaxation phase.

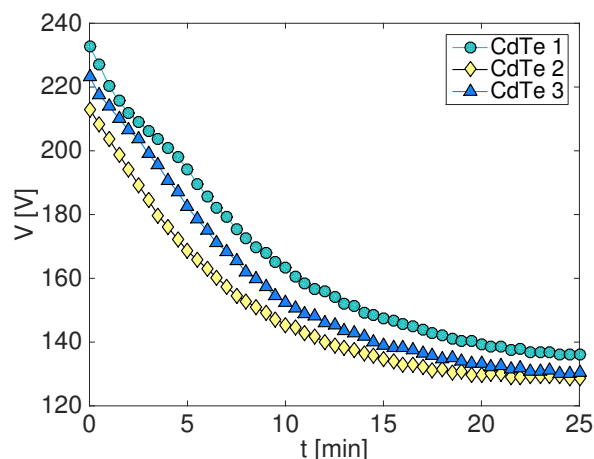


FIGURE 5.2: Dramatic voltage drop due to short circuit current treatment of CdTe modules. Voltage values are corrected for temperature effects.

5.2.2 CdTe low irradiance light soaking

Low irradiance light soaking

Cell material	CdTe
Device treatment	Light soaking
Test stand	IV flasher (3.2.1)
Light source	Halogen lamp field
Irradiance [W/m^2]	50
Illumination duration [$h:min$]	2:30
Bias state	OC

Low irradiance illumination of $50 W/m^2$ was chosen for light soaking for several reasons. Even though it does not occur in all thin-film technologies, annealing effects and module degradation caused by high irradiance could interfere with the metastable behavior. There are also practical reasons of easier handling, especially with temperature control of the modules, which is less so an issue with cells due to the size of the sample.

For this test, the module was illuminated in the indoor IV flasher setup (3.2.1) on a receding test plane under a halogen lamp array. Given the chosen low irradiance, the temperature of the module could be kept stable at room temperature throughout the experiment. After defined time steps, the electrical parameters were obtained from IV-curve measurements by the Pasan electronic load device (3.2.3), applying the voltage sweep in forward direction. Due to the sliding test plane, the net time associated with IV characterization, where the module was not illuminated (except for the flash), was minimized to $< 10 s$. The flash was set to $1000 W/m^2$ and had a duration of $10 ms$.

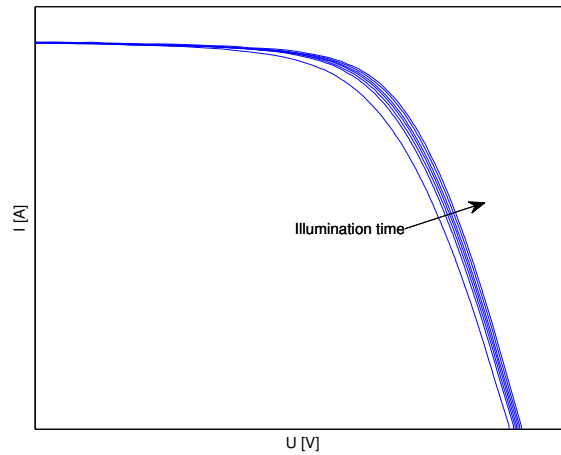


FIGURE 5.3: Qualitative improvement of CdTe IV characteristics through low-irradiance light soaking.

As a qualitative result in figure 5.3, the IV curves of the module improved with increasing illumination duration. This is due to both, an improvement in V_{oc} and the FF . The V_{oc} improvement is represented by an IV curve shift along the x -axis, while the FF increase can be found in the higher negative slope of the IV curve between the MPP and the V_{oc} , meaning a "bulgier" curve.

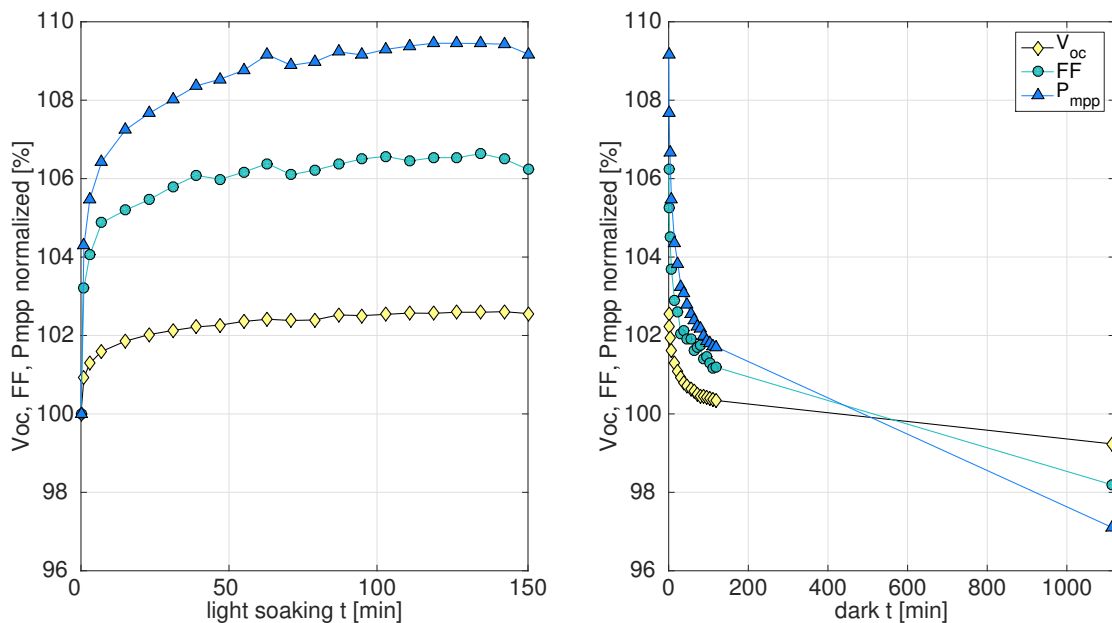


FIGURE 5.4: V_{oc} , FF and P_{mpp} development of a CdTe module under low light soaking of 50 W/m^2 and subsequent dark relaxation.

In quantitative terms, the behaviors of V_{oc} , FF and P_{mpp} are visualized in figure 5.4 and absolute values are given in table 5.2. While the I_{sc} is not significantly affected by the low light soaking, V_{oc} and FF show significant increases of 2.6% and 6.6% respectively, mainly within the first few minutes of illumination. Consequently, the maximum power P_{mpp} experiences an increase of 9.4% compared to the initial flash IV measurement.

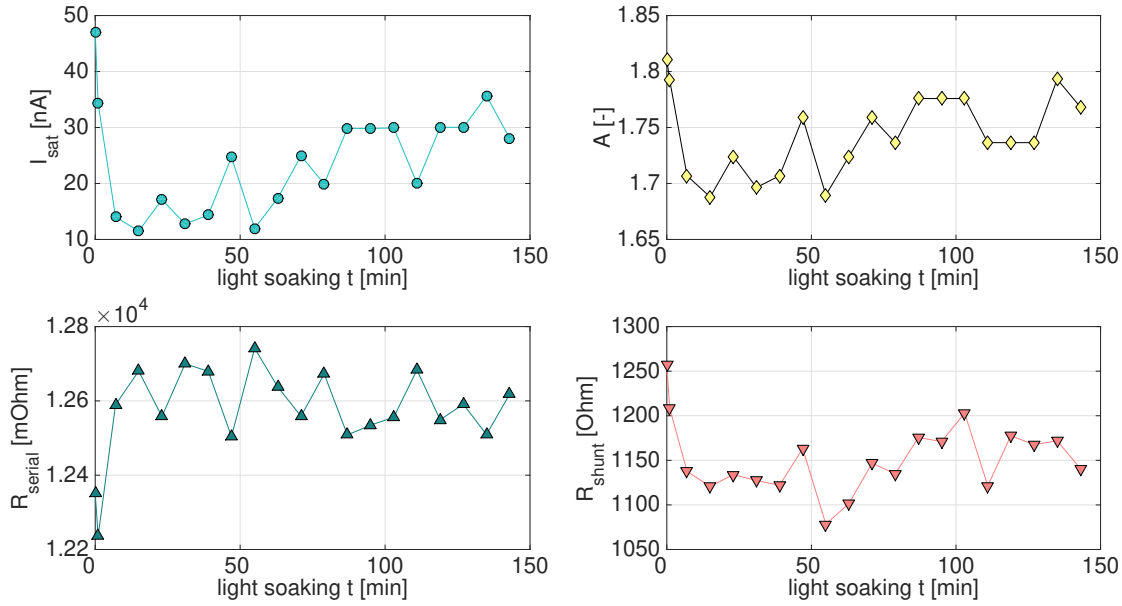


FIGURE 5.5: I_{sat} , ideality factor A , R_s and R_{sh} extracted from a single diode equation fit for 50 W/m^2 light soaking.

Further parameters were extracted from a single diode equation fit of the IV curves for each data point and plotted in figure 5.5. The model for the non-ideal diode equation is explained in chapter 2. In the case of modeling module IV characteristics, the equation must also include a term for the number of cells n . The CdTe modules used in this test comprise 116 cells in series.

$$I = I_{light} - I_{sat} \left(e^{\frac{q}{nAkT}(V + IR_s)} - 1 \right) - \frac{V + IR_s}{R_{sh}} \quad (5.1)$$

It can be assumed that $I_{light} \approx I_{sc}$. In a numerical fit, the parameters saturation current I_{sat} , ideality factor A , series resistance R_s and shunt resistance R_{sh} are extracted from the individual IV measurements. In lack of a dark IV characteristic, the precision of the obtained values has to be treated carefully.

The saturation current I_{sat} in figure 5.5 shows a decreasing tendency. With the relation between V_{oc} and I_{sat} derived from the illuminated diode equation, a decreasing I_{sat} supports the increase of the V_{oc} in figure 5.4.

$$V_{oc} = \frac{kT}{q} \ln \left(\frac{I_{light}}{I_{sat}} + 1 \right) \quad (5.2)$$

Likewise, a declining tendency in the ideality factor A can be related to the increase in the fill factor in figure 5.4. In a qualitative way, lower ideality factors are therefore also expressed in "bulgier" IV curves, as observed in figure 5.3. With ideality factors between $1.3 \leq A \leq 2$ for well-behaved thin film cells [10], the values appear to be in a reasonable range.

An increase in the series resistance in figure 5.5 is unexpected, given the overall increased

Sample	CdTe FS-272 30511
illumination	50 W/m^2 halogen light soaking
circuit conditions	OC
duration [h:min]	2:31
initial V_{oc} [V]	88.6
max. V_{oc} [V]	90.9
final V_{oc} [V]	90.8
initial FF [%]	59.7
max. FF [%]	63.6
final FF [%]	63.4
initial P_{mpp} [W]	67.6
max. P_{mpp} [W]	74.0
final P_{mpp} [W]	73.9
illumination	dark relaxation
duration [h:min]	18:34
V_{oc} [V] after 2:00h	88.9
final V_{oc} [V]	87.9
FF [%] after 2:00h	60.4
final FF [%]	58.6
P_{mpp} [W] after 2:00h	68.8
final P_{mpp} [W]	65.7

TABLE 5.2: Results: CdTe module light soaking with 50 W/m^2 irradiance and subsequent dark relaxation with absolute values for the V_{oc} , FF and P_{mpp} development.

performance of the module, however, the values may be artifacts of the numeric fit, since I_{sat} and A also influence the IV curve slope towards the V_{oc} . Also, values for the shunt resistance extracted from the fit need to be treated carefully, because of high variations in values due to starting points of the fit.

Figure 5.4 shows, that following the light soaking period, a dark relaxation induces a reverse effect on the module parameters V_{oc} , FF and P_{mpp} . Again, the largest change can be observed within the first few minutes of relaxation. This is bad news for reliable characterization procedures, because even after dedicated light soaking pre-treatment, the dark relaxation will change electrical module parameters within minutes after illumination.

After measuring the effect of dark relaxation for 2h, the module was left in the dark for another 16:34h before a final IV flash was done. The final values all lie below the initially measured values before light soaking, and hence leave the module at a worse

state than before light soaking. With a V_{oc} at 99.2% and a FF at 98.2% of the respective initial values, the P_{mpp} accumulates the losses and yields 97.1% of the initially measured maximum power.

A possible explanation for this drop below initial electrical characterization values could be an actually "undefined" and hence not fully relaxed state prior to the light soaking treatment, despite the special care which was taken for storing the modules in darkness. A general deterioration of the modules over the time period of several months was not observed.

5.2.3 50 W light soaking under different bias conditions

Low irradiance light soaking und different bias conditions

Cell material	CdTe
Device treatment	Light soaking
Test stand	IV flasher (3.2.1)
Light source	Halogen lamp field
Irradiance [W/m^2]	50
Illumination duration [$h:min$]	between 1:30 to 2:30
Bias state	OC, MPP, SC

The same procedure as described in 5.2.2 was adhered to also for low irradiance light soaking with the modules kept at a bias. In addition to light soaking at open circuit condition, a CdTe module was also illuminated while being kept at the maximum power point and under short circuit condition. The bias was applied through a power supply at the respective levels measured in the earlier *IV* characterization. During the light soaking phase, the bias was only disconnected for the time being of a characterization flash and re-applied immediately afterwards. For reasons of comparability, the same CdTe module was used for all three light soaking events, on different days providing enough time for the module to undergo relaxation in between.

Figure 5.6 exhibits the development of the V_{oc} , FF and P_{mpp} under light soaking for the three bias conditions. All three light soaking phases resulted in an improvement of the electrical parameters shown, while the I_{sc} did not change in any significant way. The observation shows clearly, that illumination under open circuit conditions has the strongest metastable effect on the the CdTe module. The smallest effect could be observed under short circuit condition. Keeping the module at maximum power point conditions via the power supply, however, yielded increases in between the other two.

These results show well, how flooding the junction with charge carriers can affect the metastable behavior of the photovoltaic device. In table 5.3 the values for V_{oc} , FF and P_{mpp} are displayed.

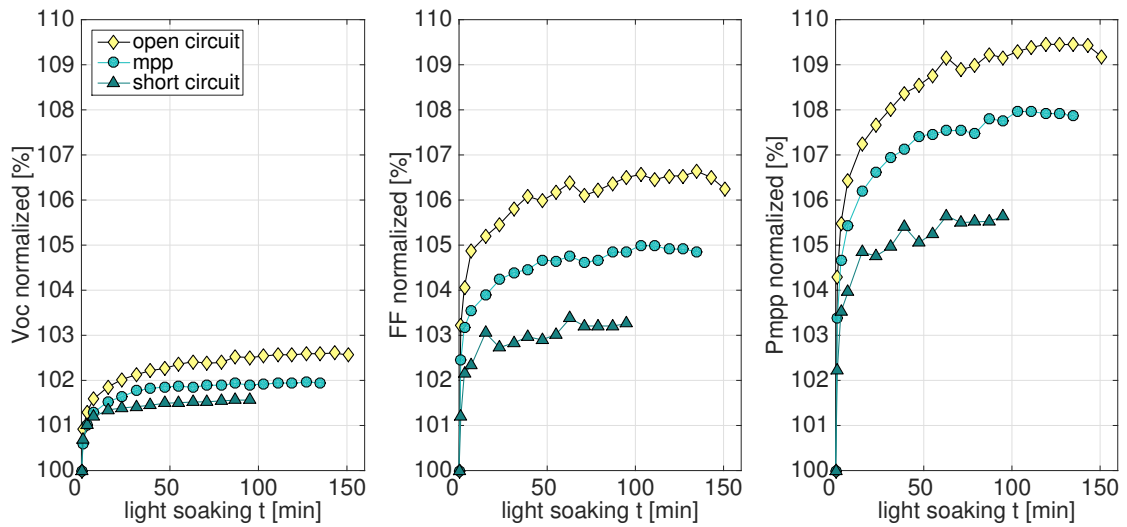


FIGURE 5.6: Comparison of different bias conditions during low irradiance light soaking of 50 W/m^2 . The graphs show the development of V_{oc} , FF and P_{mpp} at open circuit, maximum power point and short circuit conditions for a CdTe module.

illumination circuit conditions	50 W/m^2 halogen light soaking		
	open circuit	maximum power point	short circuit
duration [h:min]	2:31	2:15	1:35
initial V_{oc} [V]	88.6	87.1	87.6
max. V_{oc} [V]	90.9	88.8	89.0
final V_{oc} [V]	90.8	88.8	89.0
initial FF [%]	59.7	57.6	58.6
max. FF [%]	63.6	60.5	60.6
final FF [%]	63.4	60.4	60.5
initial P_{mpp} [W]	67.6	64.4	65.8
max. P_{mpp} [W]	74.0	69.5	69.5
final P_{mpp} [W]	73.9	69.4	69.5

TABLE 5.3: Results: CdTe module light soaking with 50 W/m^2 irradiance under different bias conditions with absolute values for the V_{oc} , FF and P_{mpp} development.

5.2.4 1000 W light soaking

1000W light soaking	
Cell material	CdTe
Device treatment	Light soaking
Test stand	Static solar simulator & Pasan electronic load
Light source	Static solar simulator
Irradiance [W/m^2]	1000
Illumination duration [$h:min$]	2:30
Bias state	OC

In contrast to the previous light soaking treatments for CdTe modules with a low irradiance, now the effect of a one-sun light soaking equivalent was investigated. For this purpose, a different setup was used. The modules were kept inside the static solar simulator (see section 3.2.2) for both light soaking and *IV* characterization sweeps. This in situ setup enabled light exposure and characterization without time delay. For obvious reasons, the reference cell also needed to be kept inside the static solar simulator.

Differences in the characterization setup can be attributed to a slightly different spectrum of the light sources (class B), however, tests have proven the comparability of *IV* characterizations for various module technologies between the flasher and the static solar simulator.

A greater challenge proved to be the thermal stability of modules within the setup. Because of the nature of the experiment of suddenly exposing a module to $1000 W/m^2$ irradiance, large temperature fluctuations of the modules could be observed. Starting at 25 °C, the module's temperature could rise above 45 °C within minutes, before the air cooling effect of the solar simulator showed an effect. Because of the insufficiency of the temperature correction parameters for temperatures strongly deviating from 25 °C, the temperature effect of this experimental setup could not be neglected.

This is why, eventually, the modules were pre-heated with a heating blanket before the light treatment, while still in the dark. This way, an adequate stationary thermal state throughout the light soaking period in the static solar simulator could be reached and the temperature effect could be ruled out.

After the light soaking period, the modules were, however, transferred to the *IV* flasher, in order to provide a dark environment for the relaxation phase. Moving the modules from one setup to the other took two minutes, before the first *IV* flash could be done. Figure 5.7 shows the electrical parameters V_{oc} , FF and P_{mpp} for a CdTe module at one-sun irradiance light soaking and subsequent dark relaxation. In figure 5.8 the fitted values of I_{sat} , ideality factor A , R_s and R_{sh} are plotted for the light soaking duration.

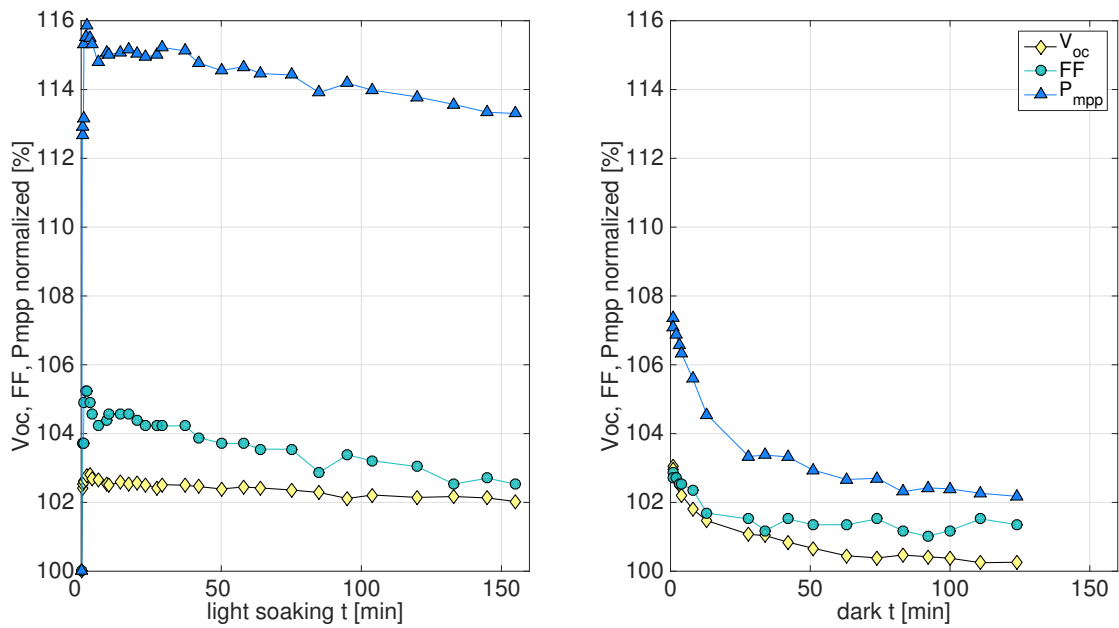


FIGURE 5.7: $1000 [W/m^2]$ light soaking and subsequent dark relaxation for a CdTe module. The graphs show the normalized development of V_{oc} , FF and P_{mpp} at open circuit conditions.

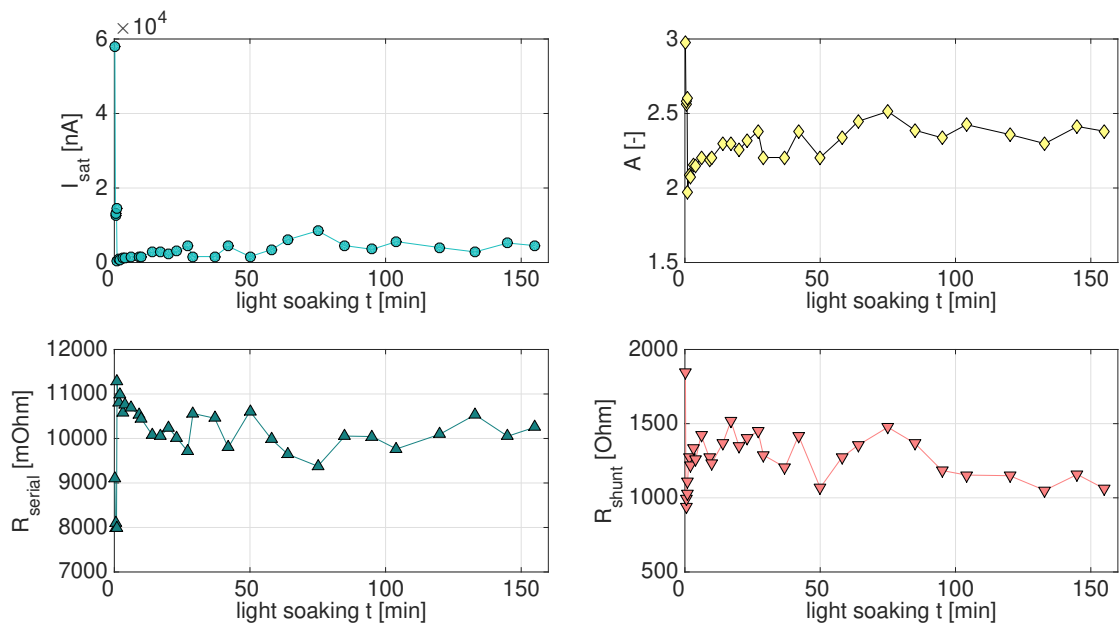


FIGURE 5.8: I_{sat} , ideality factor A , R_s and R_{sh} extracted from a single diode equation fit for $1000 W/m^2$ light soaking.

Sample	CdTe FS-272 30307
illumination	1000 W/m^2 light soaking static solar simulator
circuit conditions	OC
duration [h:min]	2:35
initial V_{oc} [V]	87.0
max. V_{oc} [V]	89.3
final V_{oc} [V]	88.8
initial FF [%]	59.2
max. FF [%]	62.3
final FF [%]	60.7
initial P_{mpp} [W]	53.1
max. P_{mpp} [W]	61.5
final P_{mpp} [W]	60.1
illumination	dark relaxation
duration [h:min]	2:04
first dark V_{oc} [V]	89.7
final V_{oc} [V]	87.2
first dark FF [%]	60.9
final FF [%]	60.0
first dark P_{mpp} [W]	57.0
final P_{mpp} [W]	54.2

TABLE 5.4: Results: 1000 [W/m^2] light soaking and subsequent dark relaxation for a CdTe module. Absolute values for the V_{oc} , FF and P_{mpp} development.

In this setup, the first measurement point was taken as initial characterization from the IV flasher. Different from the light soaking phases at $50 W/m^2$, the increase in all displayed electrical parameters happens almost immediately within the first minute. Following this jump, the V_{oc} and FF exhibit a slight decrease, which can consequently be observed in the P_{mpp} as well. Trends in the fits for the saturation current I_{sat} and the ideality factor A support this dynamic, whereas the values for series resistance R_s and shunt resistance R_{sh} prove less reliability being extracted from the fit.

The decrease of the V_{oc} , FF and P_{mpp} during the dark relaxation phase shows, that a performance enhancing metastable light soaking effect has actually occurred after the initial IV flasher characterization values. The small fluctuations of the values in the beginning of the light soaking cycle can be explained by a slight temperature drop of $5^\circ C$ in the first two minutes. Even at small temperature changes around STC temperature, the deficiency of temperature coefficients for metastable effects could be observed.

Interestingly, the V_{oc} and P_{mpp} show a certain gap between the last measured values during light soaking and the first measured values in dark relaxation. While the P_{mpp} exhibits a significant decrease, the V_{oc} appears to increase in the beginning, before entering the relaxation decrease which can also be observed in other CdTe dark relaxation phases, like in figure 5.4. The different spectra of the two light sources sources in the test setups could have an impact on the observed jump. The initial sweeps were taken in the flasher (see section 3.2.1) with a class-A spectrum, whereas the sweeps during the light soaking period were done under 1000 W/m^2 illumination of the static sun simulator (section 3.2.2) with a class-B spectrum.

5.3 CIGS modules

Three commercial CIGS specimen by former Würth Solar were available for testing. The modules underwent initial characterization and stabilization according to IEC 61646 [99]. Their main parameters are shown in table 5.5 and can also be viewed in more detail in the data sheet in Appendix B.

Cell material	CIGS
Manufacturer	Würth Solar
Module type	WSG0036E070
P_{mpp} [W]	70
V_{mpp} [V]	33
I_{mpp} [A]	2.12
V_{oc} [V]	42.3
I_{sc} [A]	2.4

TABLE 5.5: CIGS module specimen parameters at standard test conditions.

Electroluminescence images of the modules were taken for visual inspection of the module quality and can be viewed in figure 5.9, where some malfunctioning areas in dark spots can be detected.

5.3.1 CIGS low irradiance light soaking

For this test, the module was illuminated in the indoor IV flasher setup (3.2.1) under the halogen lamp array in the same setup as the CdTe modules. Given the chosen low irradiance, the temperature of the module could be kept stable at room temperature throughout the experiment. After defined time steps, electrical parameters were obtained from IV-curve measurements by the Pasan electronic load device (3.2.3), applying the voltage sweep in forward direction. Due to the sliding test plane, the net time

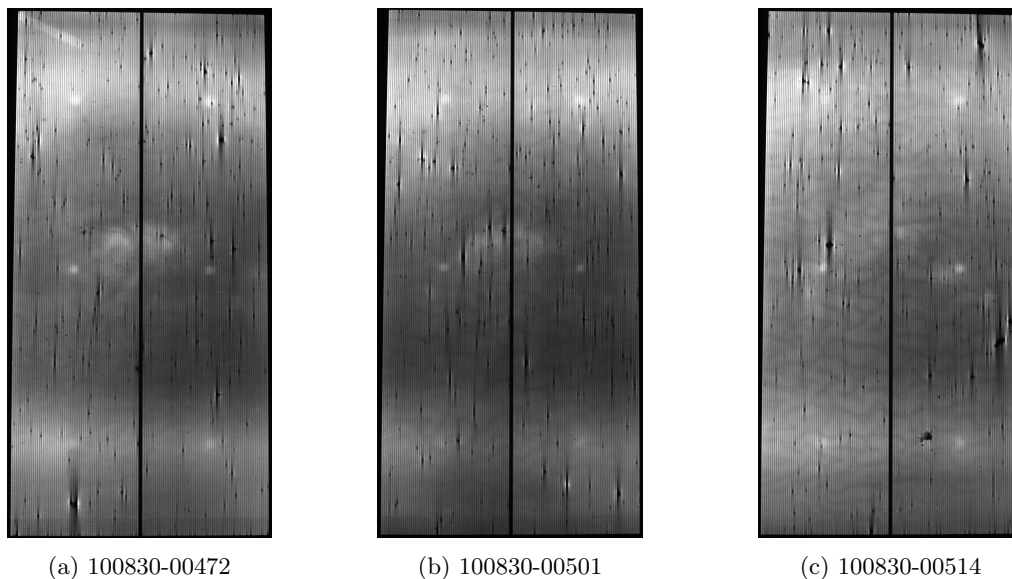


FIGURE 5.9: CIGS modules: Electroluminescence images of the untreated test devices.

Low irradiance light soaking

Cell material	CIGS
Device treatment	Light soaking
Test stand	IV flasher (3.2.1)
Light source	Halogen lamp field
Irradiance [W/m^2]	50
Illumination duration [$h:min$]	2:49
Bias state	OC

associated with *IV* characterization, where the module was not illuminated (except for the flash), was minimized to < 10 s. The flash was set to $1000 W/m^2$ and had a duration of 10 ms.

While figure 5.10 shows, that the V_{oc} is not affected by large metastable changes, it shows an upwards trend nonetheless, climbing by 0.2 % after 1:59 h of illumination. The *FF* and as a secondary effect the P_{mpp} experience larger changes, after an initial dip in the first 3 minutes. Looking at the change in V_{oc} compared to *FF*, it becomes apparent, that the P_{mpp} roughly follows the development of the *FF* in this case. This can also be qualitatively understood by looking at the development of the *IV* curve shapes in figure 5.11. In contrast to the CdTe modules, where the V_{oc} is more heavily affected by illumination, the V_{oc} in these CIGS modules remains rather stable, while the values of V_{mp} and I_{mp} for the maximum power point improve alongside with the *FF*. The values for I_{sat} , ideality factor A , R_s and R_{sh} in figure 5.12 were extracted from numerical fits using the single diode equation 5.1. Despite three outliers, which are probably fit artifacts, the saturation current does not show a significant trend, which is also represented in the relatively steady V_{oc} . Disregarding the outliers, the fits for the ideality factor A exhibit little variation, which leaves the recognizable decrease of the

series resistance R_s as the main contributor to the rise in the FF , which is also visibly noticeable in the overlay of IV curves in figure 5.11.

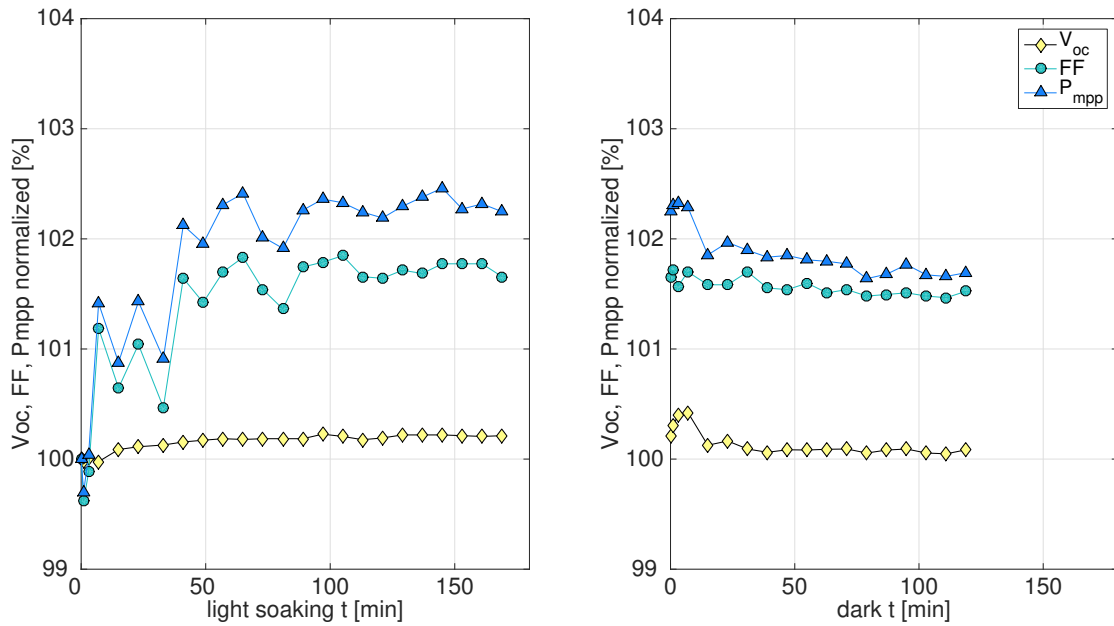


FIGURE 5.10: V_{oc} , FF and P_{mpp} development of a CIGS module under low light soaking of 50 W/m^2 and subsequent dark relaxation.

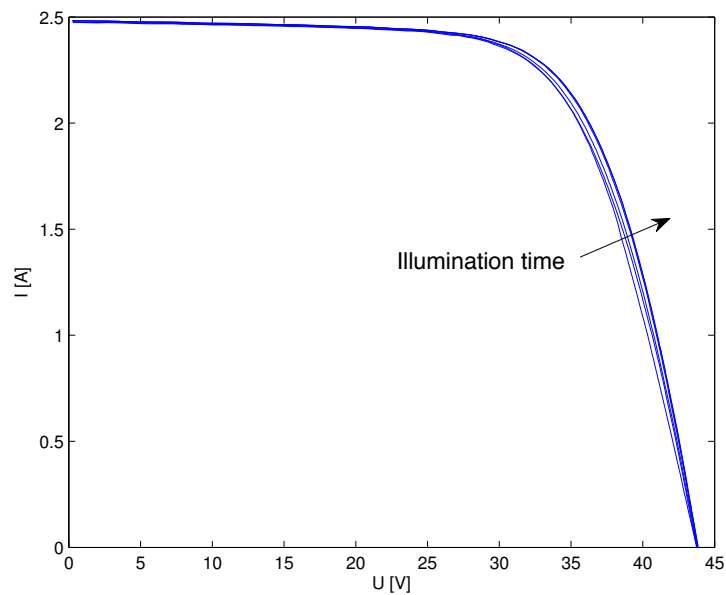


FIGURE 5.11: Qualitative improvement of CIGS IV characteristics through low-irradiance light soaking.

While most of the parameter change from illumination happens within the first hour of illumination, this is not true for the dark relaxation. In the first 7 minutes of relaxation, all three observed parameters even rise above the level of final illumination. Afterwards, a rather sharp drop occurs for V_{oc} and P_{mpp} , however, levels for all three stay well

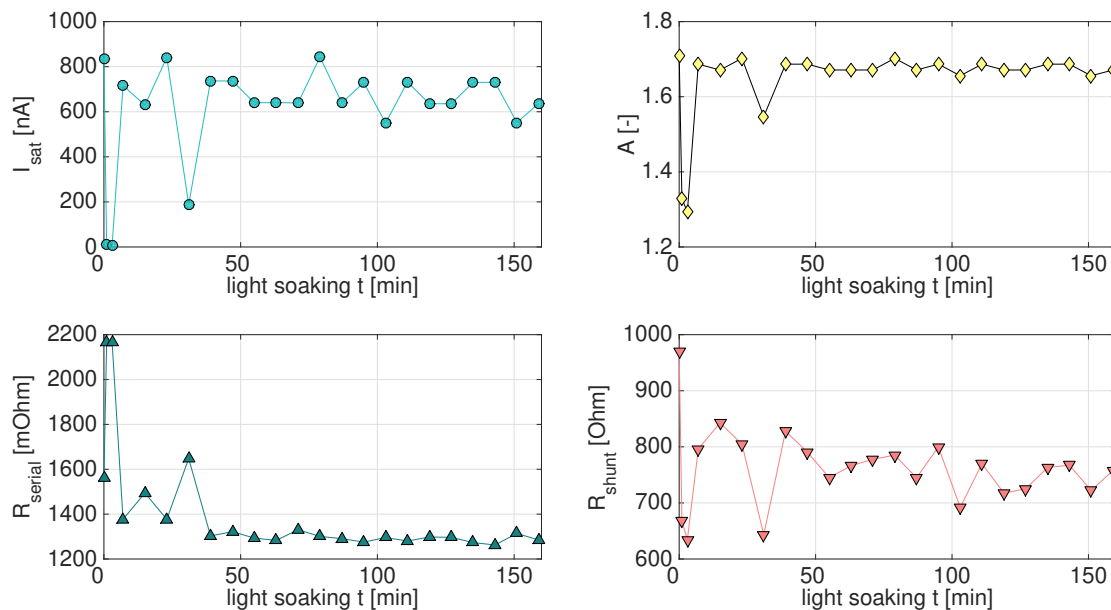


FIGURE 5.12: I_{sat} , ideality factor A , R_s and R_{sh} extracted from a single diode equation fit for 50 W/m^2 light soaking.

above the initial characterization before light soaking (100 %), even after 12 h of dark relaxation. Values for dark relaxation after a closely followed period of 1:59 hours are given in table 5.6. The module was stored in the dark and characterized again after 12h and eventually after 40 days. Only then, the initial levels before illumination could be detected, which poses a stark contrast to the relaxation behavior of CdTe modules. Apparently, relaxation in CIGS modules works at much slower time constants. It is important information for correct characterization, knowing that a light induced excited state will not return to the relaxed state within at least 12 h of dark storage.

5.4 Comparison with a-Si modules

In contrast to the chalcogenide solar cell technologies, silicon based technologies are typically not known for showing metastable behavior. Other than mono- and polycrystalline Si cells, hydrogenated a-Si is prone to the well established Staebler-Wronski effect [101], where changes in electrical parameters occur based on long lasting, high irradiance. The effect can mainly be attributed to defects of neutral dangling bonds D_0 [118] and is reversible when annealed under high temperatures of 170-200 °C.

Because amorphous silicon is a thin film technology, it was decided to include them in the early light-soaking study and investigate any non-Staebler-Wronski short-term light soaking behavior. The used specimen underwent initial characterization and stabilization as well as electroluminescence characterization. Displayed in figure 5.13, the

Sample	CIGS GeneCIS 472
illumination	50 W/m^2 halogen light soaking
circuit conditions	OC
duration [h:min]	2:49
initial V_{oc} [V]	43.7
max. V_{oc} [V]	43.8
final V_{oc} [V]	43.8
initial FF [%]	68.2
max. FF [%]	69.5
final FF [%]	69.4
initial P_{mpp} [W]	73.8
max. P_{mpp} [W]	75.6
final P_{mpp} [W]	75.5
illumination	dark relaxation
duration [h:min]	1:59
V_{oc} [V] after 1:59h	43.8
V_{oc} [V] after 12:00h	43.8
V_{oc} [V] after 40 days	43.7
FF [%] after 1:59h	69.3
FF [%] after 12:00h	69.0
FF [%] after 40 days	68.2
P_{mpp} [W] after 1:59h	75.1
P_{mpp} [W] after 12:00h	74.8
P_{mpp} [W] after 40 days	73.8

TABLE 5.6: Results: CIGS module light soaking with 50 W/m^2 irradiance and subsequent dark relaxation with absolute values for the V_{oc} , FF and P_{mpp} development.

modules show a good quality judging by the lack of visible defects in electroluminescence. The respective electrical parameters of this module type can be found in the following table 5.7.

5.4.1 a-Si low irradiance light soaking

The low irradiance light soaking was particularly valuable for investigating metastable effects in a-Si modules, while ruling out the Staebler-Wronski effect. Because of the low irradiance used in these short-term light soaking experiments, it can be assumed, that no Staebler-Wronski effect influences the electrical module parameters [119].

For this test, the module was illuminated in the indoor IV flasher setup (3.2.1) under

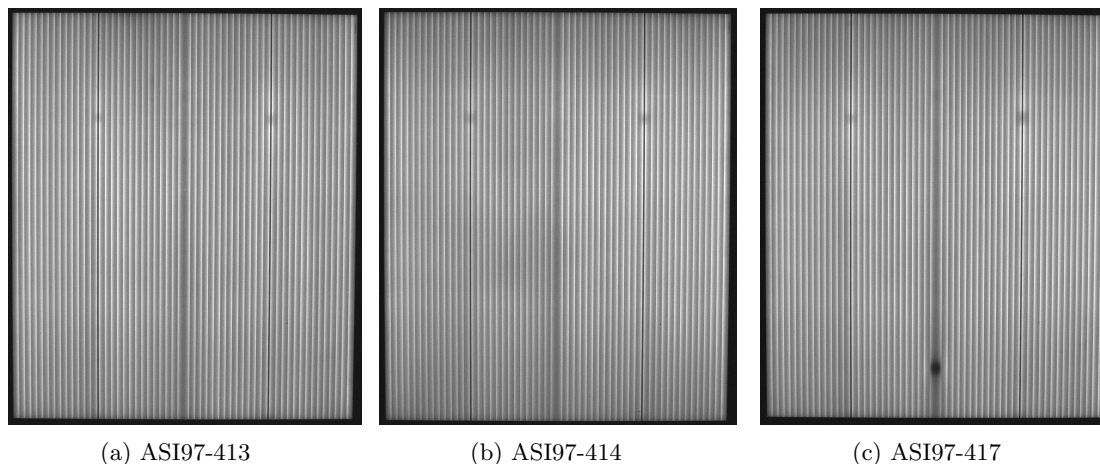


FIGURE 5.13: a-Si modules: Electroluminescence images of the untreated test devices.

Cell material	amorphous silicon
Manufacturer	Schott Solar
Module type	ASI97
P_{mpp} [W]	97
V_{mpp} [V]	17.4
I_{mpp} [A]	5.57
V_{oc} [V]	23.7
I_{sc} [A]	6.72

TABLE 5.7: a-Si module specimen parameters at standard test conditions after stabilization.

Low irradiance light soaking	
Cell material	a-Si
Device treatment	Light soaking
Test stand	IV flasher (3.2.1)
Light source	Halogen lamp field
Irradiance [W/m^2]	50
Illumination duration [h:min]	2:07
Bias state	OC

the halogen lamp array in the same setup as the CdTe and CIGS modules. At the low irradiance, the module temperature was kept stable at room temperature throughout the experiment. The experimental procedure also followed the same guidelines as already mentioned for the CdTe and CIGS tests.

Figure 5.14 shows how the electrical parameters of the a-Si module change throughout a low light soaking phase and a subsequent dark relaxation period. The V_{oc} is - similar to the results of the CIGS module - little affected by the light soaking treatment, however, also shows an upwards trend by 0.4 % after 2:07 h of illumination. This trend is almost entirely reversed after the 2:07 h dark relaxation period, which indicates that in fact another effect than Staebler-Wronski caused the light induced increase. This is also the

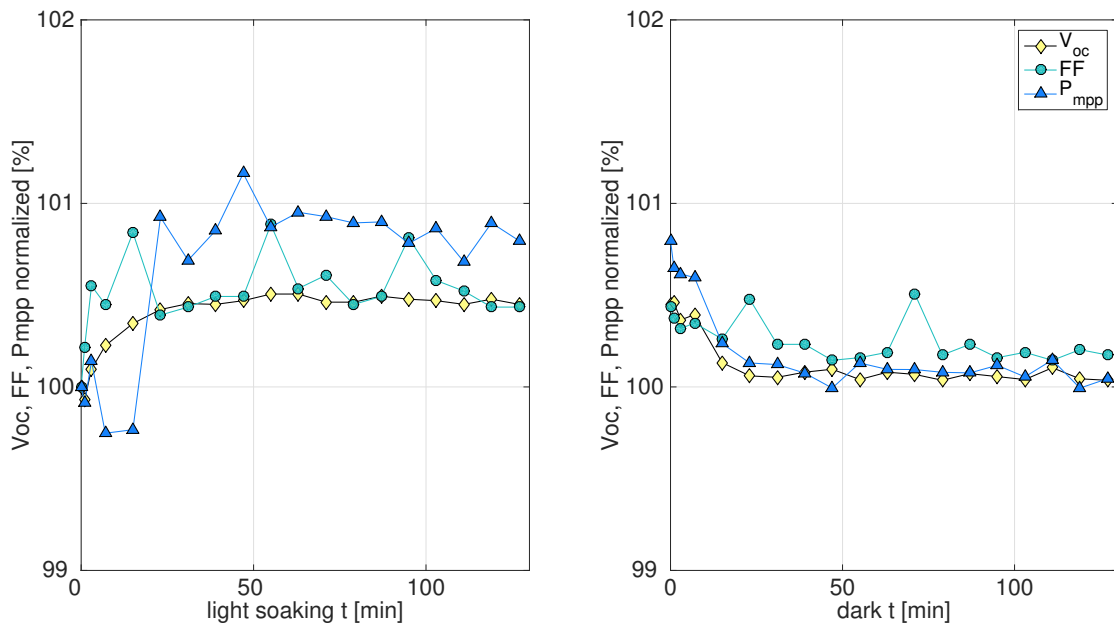


FIGURE 5.14: V_{oc} , FF and P_{mpp} development of an a-Si module under low light soaking of 50 W/m^2 and subsequent dark relaxation.

case for the FF and the P_{mpp} observations, where however, measurement results do not follow as smooth a trend as the V_{oc} . This can be due to the dependency of these parameters on several others each, making it more prone to fluctuation.

Values for the test series are given in table 5.8, which show the small change in absolute terms.

5.5 Stabilized and reliable CIGS characterization

In order to establish a practical preconditioning method, NREL proposed a procedure for CIGS stabilization and measurement majorly relying on forward bias treatment [120]. The proposal was designed as a round robin test among several characterization facilities being part of the International Energy Agency Photovoltaic Power Systems Programme Task 13, Subtask 3.1: Characterization of Performance of Thin-film Photovoltaic Technologies. The full report of Task 13 was published by IEA subsequently [121].

5.5.1 The NREL characterization practice

The primary motivation for an alternative preconditioning method is the current inadequacy of the standard IEC 61646 [99] for characterization of thin film modules other than amorphous silicon.

Sample	a-Si Schott ASI97
illumination	50 W/m^2 halogen light soaking
circuit conditions	OC
duration [h:min]	2:07
initial V_{oc} [V]	24.9
max. V_{oc} [V]	25.0
final V_{oc} [V]	25.0
initial FF [%]	69.0
max. FF [%]	69.6
final FF [%]	69.3
initial P_{mpp} [W]	125.7
max. P_{mpp} [W]	126.9
final P_{mpp} [W]	126.7
illumination	dark relaxation
duration [h:min]	2:07
final V_{oc} [V]	24.9
final FF [%]	69.1
final P_{mpp} [W]	125.7

TABLE 5.8: Results: a-Si module light soaking with 50 W/m^2 irradiance and subsequent dark relaxation with absolute values for the V_{oc} , FF and P_{mpp} development.

By applying forward bias rather than light soaking for preconditioning, heating up of the modules can be avoided to some degree. Hence, the time between preconditioning and characterization can be minimized and the modules undergoing significant relaxation before characterization can be avoided.

The round robin procedure suggests the following steps:

1. Collect the dark IV-curve at STC and determine $I_d(V_{oc})$ at the expected light V_{oc}
2. Expose the module to light for 5 consecutive hours at maximum power point condition, either
 - Indoors at 1000 W/m^2 under a CCC class light source or better, with the module temperature between 40-60 °C, or
 - Outdoors exposed to natural sunlight of 300-1300 W/m^2 at module temperature between 25-85 °C

3. Record light IV-curve for comparability reasons of the round robin test immediately after light soaking
4. Forward bias module at $I_d(V_{oc})$ during cool down for not more than 5 minutes to reach 24.5-25.5 °C
5. Record light IV-curve according to characterization standards

A full description of the proposed procedure can be found in Appendix A.

5.5.2 Validation of NREL practice

As part of a round robin test, the proposed procedure was validated by following original method as well as contrasting it with certain alterations. Results and additional characterization of used samples can be found in [122].

Two sets of devices were used for following the NREL procedure. In the first run, four un-encapsulated mini-modules fabricated at Ångström Solar Center were examined. The mini-modules were made specifically for this test together with the CIGS cell samples according to the baseline procedure explained in section 4.

Because of suspected variations in module behavior depending on different spectral light exposure [33], the NREL procedure was followed with indoor and outdoor light exposure, as well as by applying spectral filters for only red or blue light exposure, as given in table 5.9.

Module sample	Light soaking	Exposure duration [min]	V_{oc} [%]	FF [%]	P_{mpp} [%]
9105-6313	indoor white (A)	328	+1.5	-4.8	-5.1
8846d	outdoor	413	+2.7	+3.1	+7.5
9105-1313	red	397	+0.5	-2.3	-2.2
9105-1363	blue	405	+1.7	+1.2	+2.4

TABLE 5.9: List of NREL characterizations with CIGS mini-modules.

Figure 5.15 shows the normalized change in V_{oc} , FF and P_{mpp} compared to the initial characterization for these different spectral exposures, measured according to the suggested NREL procedure. While the I_{sc} was not subject to significant change, the values shown in the plot indicate an increase in V_{oc} after light soaking in all spectral ranges, even though it varies between +0.5% for red and +2.7% for outdoor light exposure.

Looking at the FF and the maximum power, it becomes evident, that the modules actually suffer in performance after exposure to indoor white light and red light. The -5.1% and -2.2% dip in P_{mpp} is mainly due to a very similar decrease in the FF .

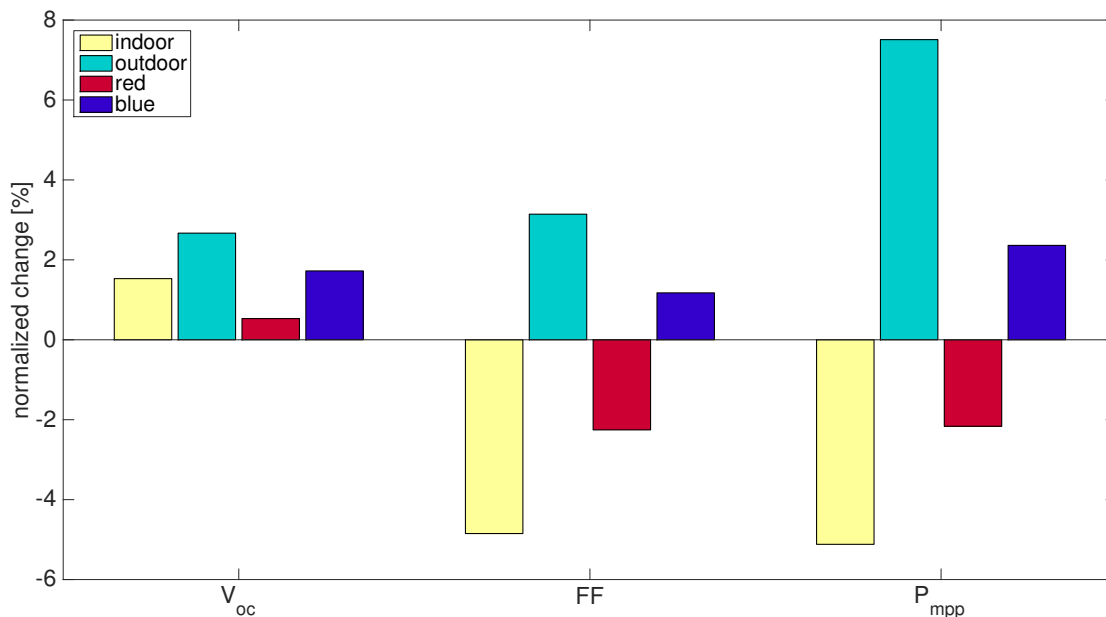


FIGURE 5.15: CIGS mini-modules characterized according to the suggested NREL procedure. V_{oc} , FF and P_{mpp} development after light exposure indoors (class A spectrum), outdoors, under a red filter and under a blue filter.

The results may be affected by varying module behavior due to variations in the fabrication process, leading to different overall light soaking behavior of the used samples. Nevertheless, they illustrate how spectral variations in the used light source can affect characterization outcomes. This is indicated by the difference between red and blue exposure and the even larger deviation between indoor white class A light soaking and outdoor exposure.

Aside from the characterization of CIGS mini-modules, three commercial modules, which are described in section 5.3, underwent the suggested NREL procedure, listed in table 5.10. One module was illuminated indoors in a class B solar simulator (see section 3.2.2), another one was illuminated outdoors and the third module was put under a UV-A lamp array, as an alternative light soaking suggestion. This could benefit from a drastically decreased illumination duration needed for the desired metastable effect.

Module sample	Light soaking	Exposure duration [min]	V_{oc} [%]	FF [%]	P_{mpp} [%]
401-001	indoor white (B)	320	+2.2	+4.9	+7.5
514-001	outdoor	358	+3.3	+4.9	+8.4
472-001	UV-A	15 ($114 W/m^2$)	+1.4	+4.1	+5.8

TABLE 5.10: List of NREL characterizations with commercial CIGS modules.

Figure 5.16 shows the results for V_{oc} , FF and P_{mpp} of the three modules following the

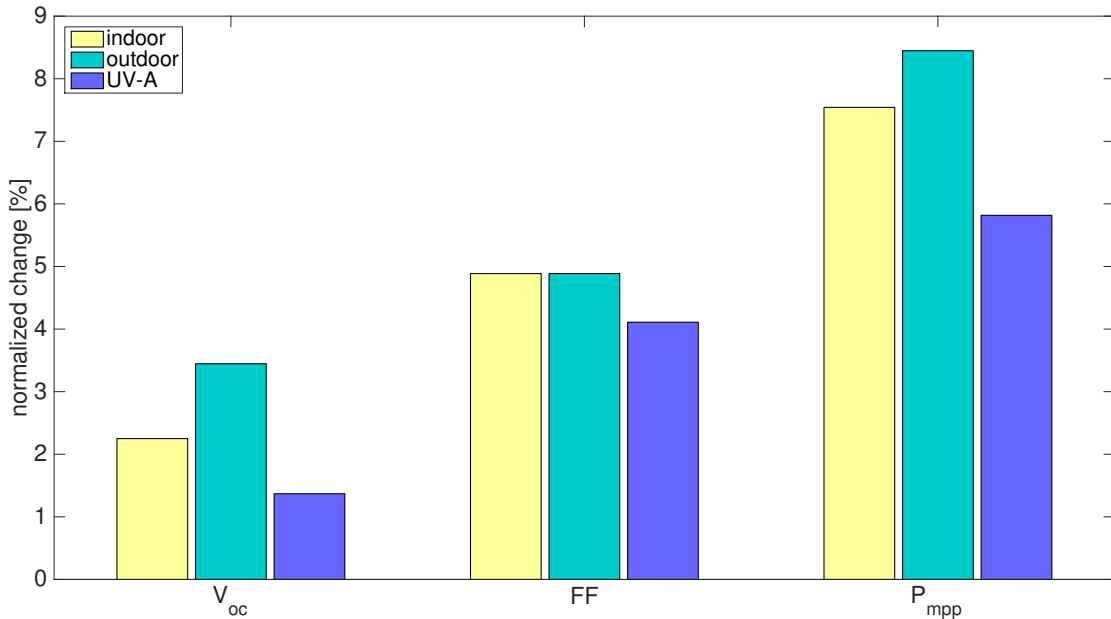


FIGURE 5.16: Commercial CIGS characterized according to the suggested NREL procedure. V_{oc} , FF and P_{mpp} development after light exposure indoors (class B spectrum), outdoors, and under 15 minutes of UV-A illumination.

NREL characterization procedure. Unlike the un-encapsulated mini modules, the commercial CIGS modules exhibit a much more homogeneous behavior. All displayed values show an increase after illumination and bias treatment. While the outdoor light soaking yields the highest increase in parameters, it is possible, that the UV-A illumination has not reached a saturated state yet. By increasing the UV-A light soaking duration, the exposure may be shortened to only half an hour or less. Finding the ideal illumination time is subject to further research.



Die approbierte gedruckte Originalversion dieser Dissertation ist an der TU Wien Bibliothek verfügbar.
The approved original version of this doctoral thesis is available in print at TU Wien Bibliothek.

Chapter 6

Discussion of Results

The previous chapters have shown experimental evidence of metastable behavior in CIGS cells and modules and CdTe modules. The extensive study encompasses variations of material compositions in the buffer layer of CIGS, buffer layer thickness in CIGS, as well as different bias conditions during illumination and different illumination spectra for both cells and modules.

Inconsistencies in some behavior illustrates, how heavily affected electrical device characteristics are by alterations in the material composition and sometimes unknown magnitudes of defects. Generally speaking, the results from commercial modules tend to be more consistent than the cell series. This is can be explained by the fact that the used cells do not always show perfect cell behavior. Even though only the best samples were taken for metastability tests, the behavior of the utilized cells is clearly not as reproducible compared to commercial modules. Also, the cells are more prone to long term changes, due to their un-encapsulated state.

The following sections will summarize the findings.

6.1 Impact of bias and light

If metastable behavior induced by forward bias or light exposure were to share the same root cause, this finding could have very beneficial effects for stabilization methods necessary for electrical device characterization. In this case, forward bias treatment could be considered a viable pre-treatment instead of lengthy light soaking procedures for chalcogenide solar devices.

The results in section 5.2.3 show a dependency of the effect of white light soaking on V_{oc} , FF and subsequently on P_{mpp} on CdTe modules. Illumination under open circuit conditions results in higher increases in all three factors, while short circuit conditions

result in the lowest increase.

This illustrates however, that bias conditions do not cancel or overpower a white light soaking effect in the investigated CdTe modules. Figure 5.6 also demonstrates, that a light induced metastable effect does affect a module under real operating conditions (*MPP*), since for the investigated modules an increase in P_{mpp} of more than 7% could be found. Procedures applied to characterize CdTe modules for power rating should therefore consider the effect of the bias condition during any phase of light soaking.

Moreover, results from forward bias treatment of CdTe modules in section 5.2.1 show contrasting behavior to light soaking treatment of the same modules in the subsequent sections. This disparity is supported by similar findings about the performance stabilization of CdTe modules in [123]. There, it is shown that bias-only treatment does not always result in the same metastable states as light soaking does. Hence, it is concluded, that the underlying mechanisms for metastable effects in CdTe devices do not share the same roots for bias or light treatment, however, in [123] it was not distinguished between red, white or blue light exposure.

The CIGS cell light soaking investigations under different bias conditions in sections 4.1.6 for CdS buffer layers and 4.1.7 for ZnSnO buffer layers leave an inconclusive picture. It can be stated, that the bias condition certainly has an influence on the development of the V_{oc} and the FF . However, in the case of the investigated CIGS cells, the influence is not completely consistent.

Especially for the bias effect in combination with light soaking, further test are necessary with very well behaved devices. By changing the bias condition, another dimension of potential effects is added to the light induced metastable effect. When dealing with less well behaved samples, it becomes too complex to single out individual sources for the observed behavior.

The effect of forward-bias-only on metastable behavior has already been shown for CdTe in [35] and for CIGS in [124]. It is suspected, that the bias-only effect shares the same origin as red light soaking does (see section 2.3.4). In [33], it is shown, that the donor defect N1, which is related to metastabilities in CIGS, has similar activation energies for forward bias, red and white light soaking. It does, however, show a significantly lower effect on capacitance-temperature (CT) profiles in comparison to red and white light soaking. Further research is required for a similar investigation of CdTe devices.

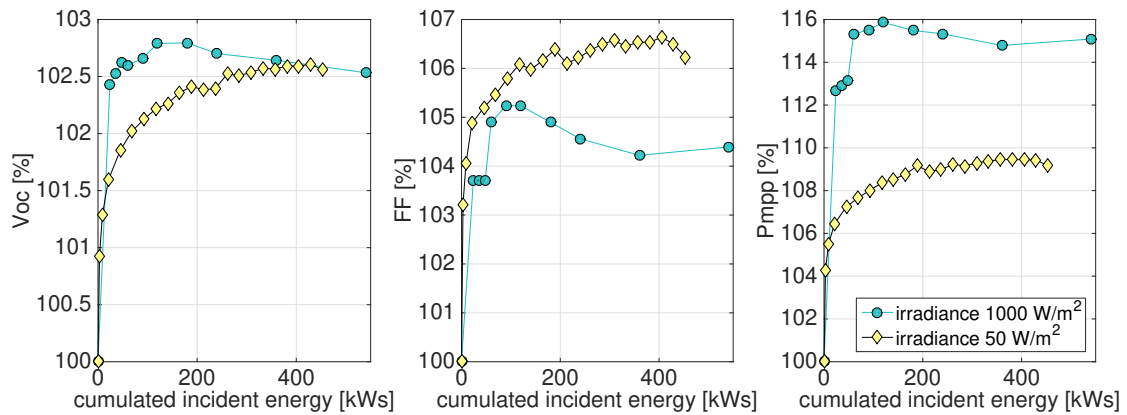


FIGURE 6.1: Normalized changes of V_{oc} , FF and P_{mpp} in CdTe modules for light soaking at $50 W/m^2$ and $1000 W/m^2$ dependent on incident energy.

6.2 Impact of irradiance

To date, there are no studies investigating the influence of the irradiance level on metastable effects. In section 5.2, CdTe modules were illuminated at different intensities. Unlike light soaking defined in the IEC 61646 [99], where irradiance levels between $600\text{--}1000 W/m^2$ are allowed, most light soaking experiments in this work were done at $50 W/m^2$. The purpose of light soaking in the IEC standard is to permanently stabilize thin film modules, primarily for overcoming the Staebler-Wronski effect for a-Si technology. Short-term metastable effects, however, are not accounted for.

For investigating metastable effects in this study, low irradiance of $50 W/m^2$ was chosen to avoid uncontrolled temperature fluctuations and keep the modules steady at STC temperature. The results in chapter 5 for both, CdTe and CIGS modules show, that metastable changes are already observable at this low intensity. Contrasting low irradiance effects of CdTe modules of section 5.2.2 with the results of section 5.2.4 with light soaking at $1000 W/m^2$ indicates that metastable changes follow a different time constant depending on the irradiance. The investigated devices show a steeper increase in V_{oc} , FF and P_{mpp} overall. This difference in the time constant could be observed in all measurements at low and high irradiance in CdTe devices. In figure 6.1, the V_{oc} , FF and P_{mpp} are charted against the cumulated incident energy for light soaking at $50 W/m^2$ and $1000 W/m^2$. Unlike considering only the illumination time, it appears, that saturation of the effect occurs within the same order of magnitude, when considering the overall incident energy. This is proportional to the number of incident photons, given similar spectral distributions.

Remaining differences could be attributed to differing spectral distributions of the light sources for low and high irradiance illumination. While for low irradiance, a common halogen lamp field was used, the static sun simulator runs at a class B spectrum at $1000 W/m^2$. Even though, the exact spectral distribution of the halogen lamps could

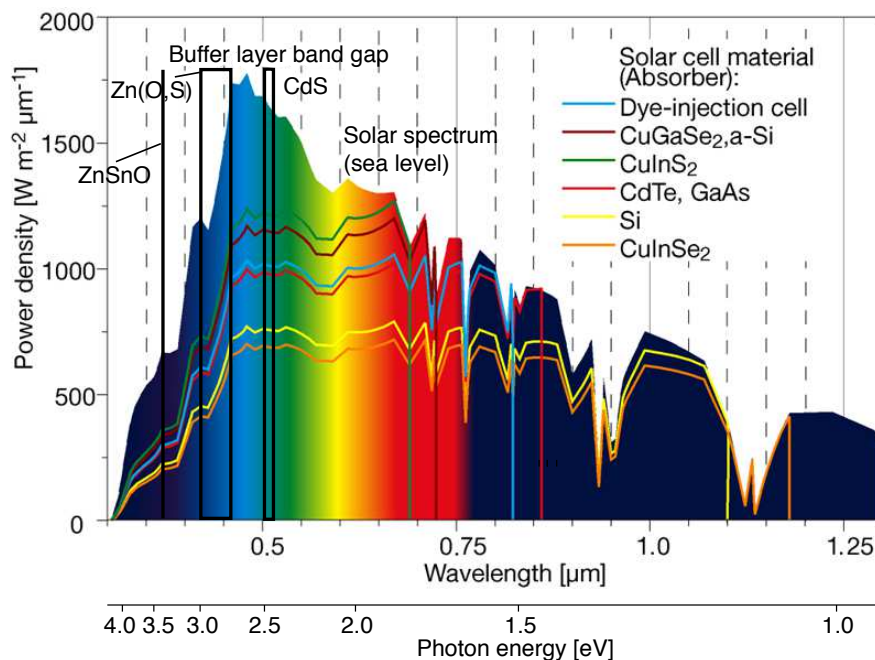


FIGURE 6.2: Buffer layer band gap of CdS, Zn(O,S) and ZnSnO in reference to solar spectrum. Original image from [125].

not be determined, it is certain, that the illumination of the static sun simulator contains significantly higher levels of blue and other visible short-wavelength photons.

Also, the generation and recombination dynamics of defect centers and traps could respond differently to different irradiance levels. This can be another reason for variations in the time constant for the saturation of metastabilities and needs further investigation.

6.3 Impact of illumination wavelength

Most solar module test laboratories lack module-size lamp arrays for single optical wavelengths. As an alternative, optical filters could be used. However, commercial module-size optical filter films typically do not have very narrow transmission bands. This is why it is difficult to come by tests at single or narrow wavelength bands for solar modules.

Because literature (see section 2.3.4) describing metastable effects in CIGS cells indicates a correlation with the spectral range of the light exposure, the effect of light soaking at different colors on metastabilities in CIGS cells was investigated in this work.

While the photon energy of the red LED used for the experiments in chapter 4 is well below the band gap of any used buffer material, the energy of the blue LED at around 450 nm is above the CdS band gap and within the range of the suspected Zn(O,S) and ZnSnO band gaps. To a significant part, the light of the white LED is also composed of blue light at 450 nm.

	V_{oc}			FF		
	red	white	blue	red	white	blue
CdS	↘	↘	↘	↗	↘	↘
Zn(O,S)	↗	↗	↘	↘	↗	↘
ZnSnO	↘	↘	↘/↗	↗	↗	↗

TABLE 6.1: Comparison of metastable behavior of V_{oc} and FF in CIGS cells upon red, white and blue light soaking.

The light soaking cycles in chapter 4 show that the buffer layer of a CIGS cell plays a decisive role for the metastable behavior of the cell. As the buffer layer must have a wider band gap than the absorber material in a heterostructure solar cell, only high energy photons can be absorbed by the buffer layer. CdS, the most widely used buffer layer material has a band gap of $E_g = 2.4 - 2.5 \text{ eV}$. The band gap for the alternative buffer layer material Zn(O,S) was determined to be between $E_g = 2.7 - 3 \text{ eV}$ [111]. For ZnSnO the optical band gap was found at $E_g = 3.3 \text{ eV}$ [108]. The band gap of these buffer layers for CIGS cells in relation to the solar spectrum available for photovoltaic energy is displayed in figure 6.2.

Aside from the differences in the band gap, different buffer layer materials vary in their ability to passivate the absorber surface. This interplay between the layers can also affect the predominant recombination path [26]. For example, in CdS buffer layer cells, the activation energy E_a indicates a space charge region dominating recombination as dominant path. In cells with Zn(O,S) buffer layers, E_a points to interface recombination as the predominant path, however, other recombination paths may be similar in magnitude.

The delicate interaction of layer materials, their grain sizes, interface effects and defects expose the complexity of observations like metastabilities. It certainly plays a role in the sometimes seemingly inconsistent behavior of different cells to light soaking.

Comparing the results from light soaking of CIGS cells with different buffer layers and different wavelengths in table 6.1, a variety of behaviors could be detected that shows the multitude of observations.

In the chapter 4 test series of CIGS cells with different buffer layer thicknesses, red light soaking has the most detrimental effect on the V_{oc} . All but one cell exhibit a moderate increase in the V_{oc} upon blue light soaking and a drop in between both red and blue for white light soaking. This not only shows two opposing behaviors for red and blue light soaking for the CIGS samples with ZnSnO buffer layers, but also indicates an overlap between red and blue light soaking effect under white light soaking.

Red and blue light effect in CIGS Interestingly, the magnitude of the metastable effect under red, blue and white light soaking differs for different buffer layer thicknesses for the V_{oc} and the FF . Assuming, that red light passes through the buffer layer unaffected by its thickness, the effect of the buffer layer on metastabilities must go beyond the absorption of high energy photons. In [108], all samples from this series are analyzed and compared. An overall trend of decreasing V_{oc} , increasing series resistance R_s and decreasing shunt conductivity G with increasing ZnSnO layer thickness is presented. Also, an overall decrease in cell efficiency η with increasing layer thickness is shown in [108]. The effects of the buffer layer thickness on the overall cell performance can therefore be an indicator for varying responses to red light soaking.

While most literature sources report a V_{oc} increase following red light soaking, falling V_{oc} and both increasing and decreasing FF have also been reported [39, 45, 52].

As suggested by [42], blue photons with $h\nu > E_{g,buffer}$ can be absorbed within the buffer layer and trigger metastable behavior. The LED used for blue light soaking emits at 450 nm, which is well above the CdS band gap and in the range of the suspected Zn(O,S) band gap, which can be compared with figure 6.2. A systematic difference in response to blue light between CIGS cells with different buffer materials, however, could not be detected. Nevertheless, it is confirmed in all experiments, that CIGS cells show different metastable behavior upon exposure to blue, red and hence white light. However, the present results do neither clearly support or oppose one of the models offered by theoretical considerations.

The CIGS mini-module tests presented in section 5.5.1 show a minor increase in the V_{oc} and a decrease in the FF upon red light exposure, with an overall decrease in maximum power P_{mpp} . This is opposing the blue light and the outdoor exposure tests, where V_{oc} , FF and P_{mpp} all improve from light soaking. Interestingly, the cell undergoing indoor light soaking under a class A solar simulator shows the worst power performance after exposure.

6.4 Summary

- Metastable behavior induced by light soaking cannot be entirely reproduced by bias instead, because the investigated electrical characteristics (V_{oc} , FF and P_{mpp}) of CIGS devices respond differently to light exposure of different wavelengths. Results of test with red, blue and white light soaking are described in chapter 4 and verify, that different kinds of effects are triggered by photons of different wavelengths. Similar conclusions for CdTe modules were made by Silverman et al. [123].
- While most literature reports metastable behavior from light exposure around one sun (1000 W/m^2), the results in chapter 5 show that significant metastable effects

in chalcogenide devices can also be observed at low irradiance levels of 50 W/m^2 . Sub-minute time resolutions of electrical parameters point to faster time constants at higher irradiance.

- Post light soaking, CIGS cells show different levels of reflectance in the NIR spectrum, described in section 4.3. The reflectance can either increase or decrease upon light soaking, depending on the buffer layer material.
- With the observations in chapters 4 and 5 being so diverse, neither theoretical model described in section 2.3.5 can be distinctly confirmed or contradicted.
- Material and layer composition has a significant effect on metastable behavior. Examinations with CIGS cells and three different buffer layer materials and thickness (see chapter 4) reveal the impact of the buffer layer on the metastable behavior of CIGS devices.
- A small reversible effect induced by light soaking and not related to the Staebler-Wronski effect could be detected in amorphous silicon modules. (See section 5.4.1)

6.5 Implications for the characterization of modules

Temperature Regardless if the source for metastable behavior is bias or light, a change in temperature of the device can influence the resulting metastable state. In [123] it is suspected, that temperature coefficients of CdTe devices are also subject to metastable changes caused by bias or light. For the interpretation of the V_{oc} development in section 5.2.1 it means, that the voltage drop could be a result of both, the metastable effect of the bias treatment plus a share of the drop resulting from a metastable temperature coefficient.

There are no studies systematically investigating the metastable effect on the temperature coefficient. Therefore it is necessary to rule out any influence secondarily caused by bias or light through a temperature change. For this reason, characterization at STC is essential and pre-treatment with either bias or light should be limited to small temperature changes for the device.

Material composition Typically, a detailed material composition of all layers in a commercial chalcogenide device is not known to a test facility. Therefore it is impractical to suggest characterization rules dependent on certain material attributes, such as the buffer layer material. Generally speaking, the fewer defects a cell has, the better "behaved" the cell or module will be, which is fortunately true for most commercially

available modules. The link between defects of various kinds and metastabilities in different theoretical models (see section 2.3.5) and observations with cells of good and poor electrical characteristics support this statement.

Bias pre-treatment Forward bias as a single step for pre-conditioning devices for electrical characterization can induce metastable behavior, which is summarized in section 2.3.4. Confirming the link between the forward bias effect and the red light soaking effect, which is described in many scientific sources, was not part of this work. However, the clear verification of differences in electrical parameters after red or blue light soaking shows, that bias by itself cannot account for all metastable changes in a cell. Therefore it is not recommended to establish a testing procedure purely relying on forward bias pre-treatment.

Using bias to fix a metastable state of a cell for a certain period of time, as it is proposed in the NREL procedure in section 5.5.1, requires further investigation. Since forward bias induces metastable behavior by itself, it is arguable whether it can be used to put a device in a stable condition for electrical characterization after a light soaking treatment.

Light soaking pre-treatment A common testing procedure should be valid and reproducible for all possible metastable behavior in thin film devices. Given the variety of metastable effects, this poses a challenge to any simplified procedure. Three aspects of pre-treatment through light soaking can be modified: irradiance, spectral composition and duration.

Tests in section 5.2 investigated the implications of low irradiance light soaking at 50 W/m^2 and light soaking at 1000 W/m^2 . In the CdTe devices, no absolute difference could be determined between low irradiance light soaking and light soaking at one sun. However, electrical parameters jump to the maximum values within the first minute of illumination, while in the cases of low irradiance, significant increase occurs throughout the entire first hour of illumination.

The spectral composition of the illumination is obviously related to triggering either red or blue light soaking effects or a mix of them. Literature and experiments in this work in chapter 4 have investigated CIGS cells. It could be verified, that the buffer layer material and thickness have a significant influence on the cell's metastable behavior. Because of the similar cell structure in CdTe devices e.g. by using the same buffer layer material of CdS, it can be speculated that this spectral sensitivity will also be the case in CdTe cells.

For commercial device characterization for power rating it can be recommended to pre-treat modules with a light source as close as possible to the AM 1.5 reference spectral

irradiance. This way, the best match between real operating conditions and characterization is guaranteed.

Verification of the NREL procedure in section 5.5.1 was also done using a UV-A light source. The procedure yielded a comparable result for V_{oc} , FF and P_{mpp} , despite a significantly shorter illumination duration of only 15 *min*. Nevertheless, only relying on illumination in the blue end of the spectrum cannot be recommended for accurate device characterization, given the strong differences of metastable behavior in different spectral regions.

The standard IEC 60904-9 [102] labels solar simulators in classes A, B and C. Among other criteria, the classification is based on a spectral match in six wavelength intervals of the spectrum between 400 and 1100 *nm*. Class A allows for a mismatch of $\pm 25\%$ in each interval, class B qualifies a $\pm 40\%$ mismatch and class C a -60% and $+100\%$ mismatch.

Because of the above mentioned results in this work regarding low irradiance light soaking, it can be assumed, that all spectral classes A, B and C for solar simulators yield sufficient results with respect to metastable behavior of chalcogenide devices.

Lastly, the duration of light soaking determines, if the metastable state is still building up or is already saturated. Depending on the irradiance, the required amount of time may significantly change, as was shown in section 5.2. Experiences with investigated commercial devices of both CdTe and CIGS have shown, that saturation was reached after 120 *min* of light soaking at low irradiance. This was also the case for the majority of CIGS cells, however, irradiance was equaling AM 1.5 J_{sc} .

Light soaking for five hours as proposed in the NREL in section 5.5.1 procedure may be reduced to two or three hours, if intermediate characterization shows saturated behavior. Apart from parameters concerning illumination, the bias condition during light soaking also has an effect on the saturated metastable state, as was shown in section 5.2.3. For accurate power rating, it can therefore be recommended to apply a load and conduct light soaking at the maximum power point of the device. This is also suggested in the NREL procedure.

6.6 Further research questions

The complex nature of metastabilities across chalcogenide devices and the still ongoing discussion about underlying theoretical models behind several involved effects still leaves many questions unanswered. In the course of this work, many problems became apparent, which could not be addressed by further experimental work.

At the cell level, a higher time resolution at the beginning of light soaking may give away more details about the dependency of metastabilities on irradiance levels. Many

of the observations in this work show quick effects occurring within the first minute of illumination. Some of these effects may eventually be overpowered by developments with a longer time constant. This has not been described in literature yet.

Putting observations in dark relaxation periods in better context with the respective metastabilities occurring during light soaking phases is necessary for better understanding. In many cases, dark relaxation completely reverses the metastable effect in either direction. In others, however, the original state can not be re-established through dark relaxation. Certain relaxation dynamics also deserve a closer examination, for example, a drop of the V_{oc} in the first few minutes of dark relaxation, which could especially but not exclusively be observed in CIGS cells with a ZnSnO buffer layer in section 4.2.1.

Further research is also necessary for establishing a correlation between the reflectance and the electrical characteristics of cells. This could help interpreting changing reflectance behavior upon light soaking in context of cell performance. Only relying on reflectance measurements has the advantage of not altering a cell's metastable behavior with a JV measurement sweep.

Overall, many experiments with CIGS cells should be repeated with CdTe cells to learn about the parallels and differences within chalcogenide solar cell metastabilities. Especially changes in the buffer layer material and properties as well as investigations with different wavelengths for illumination could be very insightful.

At the module level, the correlation between temperature coefficients and metastabilities needs to be better understood. Some experiments of this study needed to be stopped because of alterations in electrical parameters, which could not be accounted for by regular temperature corrections. This points to metastable behavior being influenced by the temperature of a device. In reality, this can pose a practical hurdle, when light soaking is considered a pre-treatment for device characterization.

Essentially, device characteristics need to deliver reasonable parameters for designing solar systems and estimating energy yields. Therefore, metastabilities close to real operating conditions need to be investigated further.

Appendix A

Experiment Documentation

Date	Material	Buffer	Sample ID	buffer thiclSetup	LS/DS	white/red/bl	OC/MPP/SC	Voc /-\	FF /-\
13.09.12	CIGS	CdS	9111-6313A1-01	IVT	LS	w	OC	\	^
13.09.12	CIGS	CdS	9111-6313A1-01	IVT	DS	w	OC	^	v
17.09.12	CIGS	ZnSnO	9098-1363A1-01	IVT	LS	w	OC	\	^
17.09.12	CIGS	ZnSnO	9098-1363A1-01	IVT	DS	w	OC	/	-
08.10.12	CIGS	CdS	9111-6313A1-01	IVT	LS	b	OC	\	/
08.10.12	CIGS	CdS	9111-6313A1-01	IVT	DS	b	OC	-	-
14.09.12	CIGS	ZnSnO	9098-1363B2-29	IVT	LS	w	OC	\	\
14.09.12	CIGS	ZnSnO	9098-1363B2-29	IVT	DS	w	OC	/	-
19.09.12	CIGS	ZnSnO	9098-1363A2-25	IVT	LS	w	MPP	\	^
19.09.12	CIGS	ZnSnO	9098-1363A2-25	IVT	DS	w	MPP	/	\
20.09.12	CIGS	ZnSnO	9098-1363B1-07	IVT	LS	w	SC	\	/
20.09.12	CIGS	ZnSnO	9098-1363B1-07	IVT	DS	w	SC	/	\
18.09.12	CIGS	CdS	9111-6313B2-32	IVT	LS	w	MPP	/	\
18.09.12	CIGS	CdS	9111-6313B2-32	IVT	DS	w	MPP	-	\
20.09.12	CIGS	CdS	9111-6363B2-32	IVT	LS	w	SC	\	\
20.09.12	CIGS	CdS	9111-6363B2-32	IVT	DS	w	SC	/	-
13.09.12	CIGS	CdS	9111-6313A2-25	IVT	LS	w	OC	\	/
13.09.12	CIGS	CdS	9111-6313A2-25	IVT	DS	w	OC	-	\
09.10.12	CIGS	ZnSnO	7850b2-14	30 nm	IVT	LS	b	OC	/
09.10.12	CIGS	ZnSnO	7850b2-14	30 nm	IVT	DS	b	OC	-
10.10.12	CIGS	ZnSnO	7846b2-05	76 nm	IVT	LS	b	OC	\
10.10.12	CIGS	ZnSnO	7846b2-05	76 nm	IVT	DS	b	OC	/
10.10.12	CIGS	ZnSnO	7848b2-15	342 nm	IVT	LS	b	OC	v
10.10.12	CIGS	ZnSnO	7848b2-15	342 nm	IVT	DS	b	OC	/
02.10.12	CIGS	ZnSnO	7850b2-14	30 nm	IVT	LS	w	OC	\
02.10.12	CIGS	ZnSnO	7850b2-14	30 nm	IVT	DS	w	OC	v
06.10.12	CIGS	ZnSnO	7846b2-05	76 nm	IVT	LS	w	OC	\
06.10.12	CIGS	ZnSnO	7846b2-05	76 nm	IVT	DS	w	OC	v
07.10.12	CIGS	ZnSnO	7844b2-14	165 nm	IVT	LS	w	OC	\
07.10.12	CIGS	ZnSnO	7844b2-14	165 nm	IVT	DS	w	OC	v
05.10.12	CIGS	ZnSnO	7848b2-15	342 nm	IVT	LS	w	OC	\
05.10.12	CIGS	ZnSnO	7848b2-15	342 nm	IVT	DS	w	OC	v
20.07.12	CIGS	ZnSnO	9098-1363	IV_meas	LS	w	OC	v	~
09.10.12	CIGS	ZnSnO	9098-1363A2-25	IVT	LS	b	OC	v	/
09.10.12	CIGS	ZnSnO	9098-1363A2-25	IVT	DS	b	OC	v	^
21.09.12	CIGS	CdS	9111-6363A2-25	IVT	DS	-	MPP	^	\
21.09.12	CIGS	ZnSnO	9098-1363A2-25	IVT	DS	-	MPP	v	^
30.04.13	CIGS	CdS	9267 A-01	IVT	LS	b	OC		
30.04.13	CIGS	CdS	9267 A-01	IVT	DS	b	OC		
02.05.13	CIGS	Zn(O,S)	9485 A-01	IVT	LS	b	OC		
02.05.13	CIGS	Zn(O,S)	9485 A-01	IVT	DS	b	OC		
02.05.13	CIGS	CdS	9267 B-25	IVT	LS	r	OC		
02.05.13	CIGS	CdS	9267 B-25	IVT	DS	r	OC		
03.05.13	CIGS	Zn(O,S)	9485 B-25	IVT	LS	r	OC		
03.05.13	CIGS	Zn(O,S)	9485 B-25	IVT	DS	r	OC		
03.05.13	CIGS	ZnSnO	7850b2-14	30 nm	IVT	LS	r	OC	
03.05.13	CIGS	ZnSnO	7850b2-14	30 nm	IVT	DS	r	OC	
04.05.13	CIGS	ZnSnO	7846b2-05	76 nm	IVT	LS	r	OC	
04.05.13	CIGS	ZnSnO	7846b2-05	76 nm	IVT	DS	r	OC	
04.05.13	CIGS	ZnSnO	7844b2-15	165 nm	IVT	LS	r	OC	
04.05.13	CIGS	ZnSnO	7844b2-15	165 nm	IVT	DS	r	OC	
05.05.13	CIGS	ZnSnO	7848b2-15	342 nm	IVT	LS	r	OC	
05.05.13	CIGS	ZnSnO	7848b2-15	342 nm	IVT	DS	r	OC	
05.05.13	CIGS	ZnSnO	9098-1363B2-25	IVT	LS	r	OC		
05.05.13	CIGS	ZnSnO	9098-1363B2-25	IVT	DS	r	OC		
06.05.13	CIGS	CdS	9267 D-30	IVT	LS	b	MPP		
06.05.13	CIGS	Zn(O,S)	9485 D-22	IVT	LS	w	OC		
06.05.13	CIGS	Zn(O,S)	9485 D-22	IVT	DS	w	OC		
07.05.13	CIGS	Zn(O,S)	9485 C-07	IVT	LS	w	OC		
07.05.13	CIGS	Zn(O,S)	9485 C-07	IVT	DS	w	OC		
07.05.13	CIGS	ZnSnO	9098-1363B2-25	IVT	LS	b	OC		
07.05.13	CIGS	ZnSnO	9098-1363B2-25	IVT	DS	b	OC		
08.05.13	CIGS	ZnSnO	7846b2-05	76 nm	IVT	LS	b	OC	
08.05.13	CIGS	ZnSnO	7846b2-05	76 nm	IVT	DS	b	OC	
08.05.13	CIGS	ZnSnO	9704d-23	150deg	IVT	LS	b	OC	
08.05.13	CIGS	ZnSnO	9692c-23	120deg	IVT	LS	b	OC	
08.05.13	CIGS	ZnSnO	9692c-23	120deg	IVT	DS	b	OC	
09.05.13	CIGS	ZnSnO	9705c-07	90deg	IVT	LS	b	OC	
09.05.13	CIGS	ZnSnO	9704d-23	150deg	IVT	LS	r	OC	
09.05.13	CIGS	ZnSnO	9692c-23	120deg	IVT	LS	r	OC	
09.05.13	CIGS	ZnSnO	9692c-23	120deg	IVT	DS	r	OC	
10.05.13	CIGS	ZnSnO	9705c-07	90deg	IVT	LS	r	OC	
10.05.13	CIGS	ZnSnO	9705c-07	90deg	IVT	DS	r	OC	

FIGURE A.1: CIGS cell experiment overview

Zelltype	Dünnschicht							
Technologie	CdTe							
Hersteller	First Solar							
Modultype	FS-272							
Seriennummer	100402030307							
Messbeginn	2010							
Datum	Durchgeführte Untersuchung	Berger	Pasan	LS	DS	OC	SC	MPP
19.11.2010	Eingangsmessung Kennlinie Flasher	x						
22.11.2010	Eingangsmessung Elektrolumineszenz							
01.12.2010	Spannungsänderung bei eingepprägtem Kurzschlussstrom							
06.12.2010	Light-Soaking	x		x		x		
15.03.2011-29.03.2011	Alterung statischer Sonnensimulator		x					x
21.06.2011	Light-Soaking	x		x		x		
04.07.2011	LS statischer Sonnensimulator 1000 W		x	x		x		
18.07.2011	Temperatureinfluss Heizdecke						x	
26.07.2011	Gleichgewichtstemperaturen im SunSim					x		
05.08.2011	Light Soaking SunSim 400 W		x	x		x		
08.08.2011	Light Soaking SunSim 200 W		x	x		x		
07.11.2011	LS statischer Sonnensimulator 1000 W, DS Flasher		x	x		x		
					x	x		
02.03.2012	LS statischer Sonnensimulator 1000 W, DS Flasher		x	x		x		
					x	x		
Zelltype	Dünnschicht							
Technologie	CdTe							
Hersteller	First Solar							
Modultype	FS-272							
Seriennummer	100402030511							
Messbeginn	2010							
Datum	Durchgeführte Untersuchung	Berger	Pasan	LS	DS	OC	SC	MPP
19.11.2010	Eingangsmessung Kennlinie Flasher	x						
22.11.2010	Eingangsmessung Elektrolumineszenz							
01.12.2010	Spannungsänderung bei eingepprägtem Kurzschlussstrom							
09.12.2010	Light-Soaking/Dark-Soaking	x	x			x		
				x		x		
08.03.2011	Light-Sokaing Kurzschluss	x	x				x	
11.03.2011	Light-Sokaing Leerlauf/Dark-Soaking Kurzschluss	x	x			x		
				x			x	
07.04.2011	Light-Soaking MPP/Dark-Soaking MPP	x	x					x
				x				x
09.05.2011-23.05.2011	Alterung statischer Sonnensimulator		x					x
28.07.2011	Light Soaking SunSim 620 W		x	x		x		
01.08.2011	Light Soaking SunSim 1000 W		x	x		x		
04.08.2011	Light Soaking SunSim 400 W		x	x		x		
23.09.2011	Light Soaking SunSim 360W, abgedunkelte Rückseite		x	x		x		
07.10.2011	Light Soaking SunSim 100W		x	x		x		
	Dark Soaking Flasher		x		x	x		
Zelltype	Dünnschicht							
Technologie	CdTe							
Hersteller	First Solar							
Modultype	FS-272							
Seriennummer	100402030130							
Messbeginn	2010							
Datum	Durchgeführte Untersuchung	Berger	Pasan	LS	DS	OC	SC	MPP
19.11.2010	Eingangsmessung Kennlinie Flasher	x						
22.11.2010	Eingangsmessung Elektrolumineszenz							
01.12.2010	Spannungsänderung bei eingepprägtem Kurzschlussstrom							
27.03.2011	Light-Soaking OC/Dark-Soaking OC	x			x		x	
						x	x	
13.04.2011-26.04.2011	Alterung statischer Sonnensimulator		x					x

FIGURE A.2: CdTe module experiment overview

Zelltype	Dünnschicht							
Technologie	CIGS							
Hersteller	Würth Solar							
Modultype	GeneCIS							
Seriennummer	01-100830-00472-001							
Messbeginn	2010							
Datum	Durchgeführte Untersuchung	Berger	Pasan	LS	DS	OC	SC	MPP
19.11.2010	Eingangsmessung Kennlinie Flasher	x						
22.11.2010	Eingangsmessung Elektrolumineszenz							
02.12.2010	Spannungsänderung bei eingepprägtem Kurzschlussstrom							
15.12.2010	Light-Soaking/Dark-Soaking	x		x		x		
24.01.2011	Light-Soaking OC/Dark-Soaking SC	x		x		x		
13.04.2011-26.04.2011	Alterung statischer Sonnensimulator		x		x		x	
								x
Zelltype	Dünnschicht							
Technologie	CIGS							
Hersteller	Würth Solar							
Modultype	GeneCIS							
Seriennummer	01-100830-00514-001							
Messbeginn	2010							
Datum	Durchgeführte Untersuchung	Berger	Pasan	LS	DS	OC	SC	MPP
19.11.2010	Eingangsmessung Kennlinie Flasher	x						
22.11.2010	Eingangsmessung Elektrolumineszenz							
17.12.2010	Doppelte LS/DS Sequenz mit anschließendem LS im Kurzsch			x		x		
					x	x		
5/3/2010	LS SC/DS SC	x		x			x	
					x		x	
09.05.2011-23.05.2011	Alterung statischer Sonnensimulator		x					
								x
Zelltype	Dünnschicht							
Technologie	CIGS							
Hersteller	Würth Solar							
Modultype	GeneCIS							
Seriennummer	01-100830-00501-001							
Messbeginn	2010							
Datum	Durchgeführte Untersuchung	Berger	Pasan	LS	DS	OC	SC	MPP
19.11.2010	Eingangsmessung Kennlinie Flasher	x						
22.11.2010	Eingangsmessung Elektrolumineszenz							
15.03.2011-29.03.2011	Alterung statischer Sonnensimulator		x					
								x

FIGURE A.3: CIGS module experiment overview

Zelltype	Dünnschicht								
Technologie	a-Si/a-Si								
Hersteller	Schott								
Modultype	ASI97								
Seriennummer	15011035022413								
Messbeginn	2010								
Datum	Durchgeführte Untersuchung	Berger	Pasan	LS	DS	OC	SC	MPP	
11/15/2010	Eingangsmessung Kennlinie Flasher	x							
22.11.2010	Eingangsmessung Elektrolumineszenz								
15.03.2011-29.03.2011	Alterung statischer Sonnensimulator		x					x	
5/5/2011	LS MPP/ DS MPP	x		x				x	
					x			x	
Zelltype	Dünnschicht								
Technologie	a-Si/a-Si								
Hersteller	Schott								
Modultype	ASI97								
Seriennummer	15011035022417								
Messbeginn	2010								
Datum	Durchgeführte Untersuchung	Berger	Pasan	LS	DS	OC	SC	MPP	
11/15/2010	Eingangsmessung Kennlinie Flasher	x							
22.11.2010	Eingangsmessung Elektrolumineszenz								
02.12.2010	Spannungsänderung bei eingepprägtem Kurzschlussstrom								
12/10/2010	Light-Soaking OC	x		x		x			
12/13/2010	Light-Soaking OC	x		x		x			
12/21/2010	LS OC / DS OC	x		x		x			
					x	x			
09.05.2011-23.05.2011	Alterung statischer Sonnensimulator		x					x	
Zelltype	Dünnschicht								
Technologie	a-Si/a-Si								
Hersteller	Schott								
Modultype	ASI97								
Seriennummer	15011035022414								
Messbeginn	2010								
Datum	Durchgeführte Untersuchung	Berger	Pasan	LS	DS	OC	SC	MPP	
11/15/2010	Eingangsmessung Kennlinie Flasher	x							
22.11.2010	Eingangsmessung Elektrolumineszenz								
13.04.2011-26.04.2011	Alterung statischer Sonnensimulator		x					x	
5/4/2011	Light-Soaking/Dark-Soaking im Kurzschluss	x		x			x		
					x		x		

FIGURE A.4: a-Si module experiment overview

Zelltype	Dünnschicht							
Technologie	CIGS							
Hersteller	Flisom							
Modultype	Testmodul							
Seriennummer	A11-01355-350							
Messbeginn	2011							
Datum	Durchgeführte Untersuchung	Berger	Pasan	LS	DS	OC	SC	MPP
31.10.2011	Eingangsmessung Flasher		x					
30.11.2011	LS, DS Flasherlade 50 W/m ²		x	x		x		
					x	x		
Zelltype	Dünnschicht							
Technologie	CIGS							
Hersteller	Flisom							
Modultype	Testmodul							
Seriennummer	A61-04682-100							
Messbeginn	2011							
Datum	Durchgeführte Untersuchung	Berger	Pasan	LS	DS	OC	SC	MPP
18.10.2011	Eingangsmessung Zellsonnensim		x					
31.10.2011	Eingangsmessung Flasher		x					
Zelltype	Dünnschicht							
Technologie	CIGS							
Hersteller	Flisom							
Modultype	Testmodul							
Seriennummer	A61-05406-100							
Messbeginn	2011							
Datum	Durchgeführte Untersuchung	Berger	Pasan	LS	DS	OC	SC	MPP
31.10.2011	Eingangsmessung Flasher		x					
16.11.2011	Light-Soaking stat. Zellsone 1000W		x	x		x		
					x	x		
-30.01.2012	Humidity Freeze Cycle							
30.01.2012	Leistungsbestimmung Flasher 1000W		x					
30.01.2012	LS Flasherlade		x	x		x		
Zelltype	Dünnschicht							
Technologie	CIGS							
Hersteller	Flisom							
Modultype	Testmodul							
Seriennummer	A61-05406-180							
Messbeginn	2011							
Datum	Durchgeführte Untersuchung	Berger	Pasan	LS	DS	OC	SC	MPP
31.10.2011	Eingangsmessung Flasher		x					
18.11.2011	Light-Soaking stat. Zellsone 150W		x	x		x		
					x	x		
Zelltype	Dünnschicht							
Technologie	CIGS							
Hersteller	Flisom							
Modultype	Testmodul							
Seriennummer	A61-05493-370							
Messbeginn	2011							
Datum	Durchgeführte Untersuchung	Berger	Pasan	LS	DS	OC	SC	MPP
31.10.2011	Eingangsmessung Flasher		x					
-30.01.2012	Humidity Freeze Cycle							
30.01.2012	Leistungsbestimmung Flasher 1000W		x					
30.01.2012	LS Flasherlade		x	x		x		

FIGURE A.5: CIGS test module experiment overview



Subject: Proposed CIGS stabilization and measurement procedure

Authors: Michael Deceglie, Timothy Silverman, Chris Deline, Bill Marion, Sarah Kurtz

Date: July 25, 2013

Introduction

Transient, light-induced changes in the performance of CIGS photovoltaic modules present a challenge to precise and repeatable measurement of performance. The current procedure for stabilizing thin-film module performance, as specified in IEC 61646, was not developed specifically for CIGS modules. In contrast, this proposed stabilization and test protocol is designed to stabilize the CIGS material system prior to measurement. This procedure will be used in a round robin test with the goal of reducing lab-to-lab variation in the measurement of CIGS module performance.

In general, the performance of a PV module changes over a continuum of time scales during its service life. The scope of this procedure is to eliminate variations from transients occurring in a day or less, while yielding standard test condition (STC) performance representative of a module operating outdoors (as opposed to one stored in the dark). We have observed significant transient behavior in CIGS modules occurring on the time-scale of minutes to hours, both upon exposure to light, and upon being kept in the dark after light exposure. While the procedure described in IEC 61646 provides no guidance on the time between light-exposure and measurement, the procedure described here requires that the reported measurement be taken within 5 minutes of the module cooling to the measurement temperature after light exposure. This is intended to minimize errors associated with changes in module performance as it reverts to its dark state. In addition, it is known that forward bias can induce the same changes in performance as light exposure. Based on our observations that the light state can be preserved by forward bias, this procedure dictates that forward bias be applied to the module while it cools to the measurement temperature to further reduce errors associated with modules reverting to their dark state. Here we choose 300 W m^{-2} as a minimum irradiance during light exposure to ensure that any transients are being induced; this is based on our observations that transients can be induced with irradiance as low as 150 W m^{-2} .

This proposed procedure calls for two measurements of performance. One immediately after the conclusion of the light-soak, regardless of module temperature, and one once the module has cooled to STC temperature. The first curve will serve as diagnostic data in the analysis of the round-robin results to determine if, and to what extent, transients may have affected the test results. The second measurement will be the reportable performance from a given test lab.

15013 Denver West Parkway
Golden, CO 80401
Phone 303-275-3000

NREL is a national laboratory of the U.S. Department of Energy
Office of Energy Efficiency & Renewable Energy
Operated by the Alliance for Sustainable Energy, LLC

FIGURE A.6: NREL proposed CIGS measurement procedure, page 1

Procedure

1. Collect dark IV curve
 - Module temperature: 24.5–25.5°C (monitored at single point on center of back of module)
 - Voltage range: 0 – expected V_{oc} at standard test conditions (STC), AM1.5G and 25°C, unless another voltage limit is specified by manufacturer. Maximum forward bias must be at least to expected V_{oc} .
 - The power supply used in this measurement should have a current limit set to expected I_{sc} to protect the module.
 - Measure, record, and report:
 - i. Full IV curve
 - ii. $I_d(V_{oc})$ as derived from the dark IV curve. $I_d(V_{oc})$ is defined here as the forward-bias current passed through the module in the dark when biased to the expected STC V_{oc} .
2. Expose module to light
 - Expose to light for 5 continuous hours
 - If the equipment is available to do the indoor procedure (2.1), then procedure 2.1 must be used. If indoor capability is not available, 2.2 may be used.
 - 2.1: Indoors
 - Expose to class CCC or better illumination at 1000 W m^{-2} .
 - Maintain the module at 40–60°C.
 - Maintain the module at maximum power, a constant load may be used.
 - 2.2: Outdoors
 - Expose to natural sunlight between $300\text{--}1300 \text{ W m}^{-2}$.
 - Module temperature must remain between 25–85°C.
 - Use active tracking to maintain the module at maximum power operation.
 - Excursions of irradiance or temperature outside the limits require restarting this step.
 - Measure, record, and report:
 - i. Start and end time and date
 - ii. Whether 2.1 or 2.2 is used
 - iii. Irradiance (sampled at least once every 5 minutes)
 - iv. Module temperature (sampled at least once every 5 minutes, monitored at single point on center of back of module)
3. Record first light IV curve
 - Must be done as soon as possible after the conclusion of the light soak, regardless of module temperature. If the time between light exposure and measurement exceeds 1 minute for any module, the module must be biased at a constant current of $I_d(V_{oc})$ until the measurement is made. Time between Steps 2 and 3 must not exceed 15 minutes.
 - A shuttered continuous or pulsed solar simulator should be used.
 - Illumination with class AAA illumination according to IEC 60904-9.
 - Measure, record, and report:
 - i. Full IV curve

15013 Denver West Parkway
Golden, CO 80401
Phone 303-275-3000

NREL is a national laboratory of the U.S. Department of Energy
Office of Energy Efficiency & Renewable Energy
Operated by the Alliance for Sustainable Energy, LLC

FIGURE A.7: NREL proposed CIGS measurement procedure, page 2

- ii. Module temperature (3 or 4 point measurement according to IEC 61853-1 or IEC 61853-2)
 - iii. Date and time of curve
 - iv. Whether the module was biased between light exposure and measurement
- 4. Bias module while it cools
 - Bias the module at a constant current of $I_d(V_{oc})$ while it cools. Fans can be used to increase the cooling rate.
 - Begin the bias within 1 minute of the conclusion of the measurement from Step 3.
 - Monitor the module temperature (3 or 4 point measurement according to IEC 61853-1 or IEC 61853-2)
 - Within 5 minutes of all temperature measurement points reaching the range 24.5–25.5°C, carry out Step 5 (record 2nd light IV curve).
 - Measure:
 - i. Module temperature (3 or 4 point measurement according to IEC 61853-1 or IEC 61853-2)
- 5. Record 2nd light IV curve
 - Take IV curve when module is in the temperature range 24.5–25.5°C.
 - A shuttered continuous or pulsed solar simulator should be used.
 - Illumination with class AAA illumination according to IEC 60904-9.
 - Measure, record, and report:
 - i. Full IV curve
 - ii. Module temperature (3 or 4 point measurement according to IEC 61853-1 or IEC 61853-2)
 - iii. Date and time of curve

Notes:

- All times must be recorded with one-second resolution from synchronized clocks.
- This plan describes the test of a single module. Multiple modules may be simultaneously tested, however, the measurements and records must be kept for individual modules. All time limits apply to individual modules.
- Set the light level for the light IV curves using the spectral correction factor calculated from the furnished module QE.
- Whenever bias is applied before an IV curve, the module must not be removed from the bias source for more than 1 minute prior to the measurement.
- If the module must be biased while being moved around the test facility to meet the requirements of this procedure, a mobile cart equipped with a power supply running from a UPS may provide a suitable solution. Depending on facility layout, a power supply with long leads to the module may also be helpful.
- When bias is used, set a voltage limit on the power supply of the expected module V_{oc} .
- Some power supplies may be damaged if connected to the module under illumination.

15013 Denver West Parkway
 Golden, CO 80401
 Phone 303-275-3000

NREL is a national laboratory of the U.S. Department of Energy
 Office of Energy Efficiency & Renewable Energy
 Operated by the Alliance for Sustainable Energy, LLC

FIGURE A.8: NREL proposed CIGS measurement procedure, page 3



Die approbierte gedruckte Originalversion dieser Dissertation ist an der TU Wien Bibliothek verfügbar.
The approved original version of this doctoral thesis is available in print at TU Wien Bibliothek.

Appendix B

Module Data Sheets



First Solar PV-Module der Serie FS 2

Dünnschichtmodule für leistungsstarke PV-Projekte

Die PV-Module der Serie FS 2 von First Solar stellen den neuesten Stand der Dünnschicht-Technologie dar. Die Module der Serie FS 2 sind für eine Systemspannung von 1000 VDC nach IEC 61464 und IEC 61730 zertifiziert. Damit entsprechen sie den Vorgaben der Schutzklasse II. First Solar versorgt damit weiterhin führende Projektentwickler mit kosteneffizienten Dünnschichtmodul-Lösungen für große, netzgekoppelte Photovoltaikkraftwerke. Die Anwendungsingenieure von First Solar bieten technische Unterstützung und liefern eine umfassende Produktdokumentation, um die Entwicklung, die Installation und den langfristigen Betrieb von Hochleistungs-Photovoltaikkraftwerken zu unterstützen.



GARANTIE

- Gewährleistung für Material- und Verarbeitungsfehler sind fünf (5) Jahre, Leistungsgarantie über 90% der Nennleistung ($P_{MPP} \pm 5\%$) gelten für die ersten zehn (10) Jahre und 80% für fünfundzwanzig (25) Jahre entsprechend der Garantiebedingungen.
- Alle Module unterliegen einem Lebenszyklus-Management mit einem integrierten – für den Käufer kostenlosen – Rücknahme- und Recyclingprogramm.

Alle Angaben und Garantien gelten für Produkte, die in Europa verkauft und installiert werden. Für Anwendungen in den USA bitte Bezug nehmen auf das US Datenblatt (PD-5-401-02 NA).

First Solar (Europe)
Tel: +49 (0)6131 1443-0
info@firstsolar.de

First Solar (US)
Tel: +1 (602)414-9300
info@firstsolar.com

www.firstsolar.com

PD-5-401-02 DE JAN 2009

Das First Solar Logo, First Solar™ und alle mit ® gekennzeichneten Produkte sind gesetzlich geschützte Marken. Die mit ™ markierten Produkte sind Marken von First Solar Inc.

FIGURE B.1: Data sheet: First Solar CdTe modules, page 1

ELEKTRISCHE SPEZIFIKATIONEN

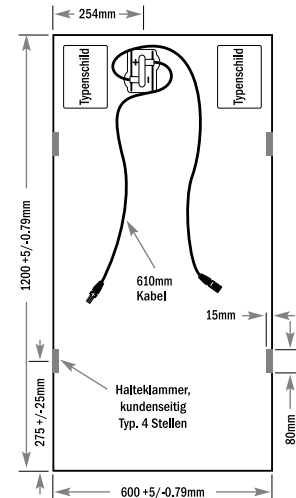
TYPEN UND NENN DATEN BEI STANDARDTESTBEDINGUNGEN**					
Nennwerte		FS-270	FS-272	FS-275	FS-277
Nennleistung (+/-5%)	$P_{MPP}(W)$	70	72.5	75	77.5
Spannung bei P_{MAX}	$V_{MPP}(V)$	65.5	66.6	68.2	69.9
Elektrischer Strom bei P_{MAX}	$I_{MPP}(A)$	1.07	1.09	1.10	1.11
Leerlaufspannung	$V_{OC}(V)$	88.0	88.7	89.6	90.5
Kurzschlussstrom	$I_{SC}(A)$	1.23	1.23	1.23	1.22
Maximale Systemspannung	$V_{SYS}(V)$	1000			
Temperaturkoeffizient von P_{MPP}	$T_K(P_{MPP})$	-0.25%/°C			
Temperaturkoeffizient von V_{OC} , für hohe Temp. (>25°C)	$T_K(V_{OC}, \text{hohe Temp.})$	-0.25%/°C			
Temperaturkoeffizient von V_{OC} , für niedrige Temp. (-40°C bis +25°C)	$T_K(V_{OC}, \text{niedrige Temp.})$	-0.20%/°C			
Temperaturkoeffizient von I_{SC}	$T_K(I_{SC})$	+0.04%/°C			
Rückstrombelastbarkeit ²	$I_R(A)$	2			
Strangsicherung max.	$I_{CF}(A)$	10 (2 IEC61730 ³)			

TYPEN UND NENN DATEN BEI 800W/m ² , 45°C, AM 1.5*					
Nennwerte		FS-270	FS-272	FS-275	FS-277
Nennleistung (+/-5%)	$P_{MPP}(W)$	52.6	54.4	56.3	58.1
Spannung bei P_{MAX}	$V_{MPP}(V)$	61.4	62.5	63.9	65.4
Elektrischer Strom bei P_{MAX}	$I_{MPP}(A)$	0.86	0.87	0.88	0.89
Leerlaufspannung	$V_{OC}(V)$	81.8	82.5	83.3	84.2
Kurzschlussstrom	$I_{SC}(A)$	1.01	1.01	1.01	1.00

MECHANISCHE BESCHREIBUNG

Länge	1200mm	Dicke	6.8mm
Breite	600mm	Fläche	0.72m ²
Gewicht	12kg	Anschl. Kabel	3.2mm ² , 610mm
Stecker	Typ Solarline 1 Stecker		
Bypassdiode	entfällt		
Zellentyp	CdS/CdTe Halbleiter, 116 aktive Solarzellen		
Rahmenmaterial	entfällt		
Abdeckung	3,2mm thermisch behandeltes Glas auf der Vorderseite, rückseitig laminiert auf 3,2mm gehärtetes Glas		
Einbettung	Laminationsmaterial mit Modulrandversiegelung		

TECHNISCHE ZEICHNUNG



Wirkungsgrad bei 200W/m²: Bei den Modulen der Serie FS 2 steigert sich der Wirkungsgrad bei 200W/m² um 2% im Vergleich zu dem bei 1000W/m² ermittelten Wert. Siehe Anwendungsrichtlinie PD-5-420 von First Solar für eine detaillierte Analyse der Leistung bei geringer Lichtintensität.

* Alle Werte +/-10%, falls nicht anders ausgewiesen. Änderungen vorbehalten.

¹ Standardtestbedingungen: 1000W/m², AM 1.5, 25°C

² Das in EN50380, Abschnitt 3.6.2. spezifizierte Verfahren wurde für kristalline Siliziummodule entwickelt. Aufgrund der Zellkonfiguration von Dünnschichtmodulen sind extrem hohe Spannungen und Ströme notwendig um Rückströme im Modul zu erzeugen. Die dadurch entstehenden Modultemperaturen liegen deutlich über den normalen Betriebstemperaturen sowie über den für den Test vorgesehenen Temperaturen. Deshalb liegt der IR-Wert des Moduls unterhalb des für den sicheren Betrieb des Moduls vorgeschriebenen Wertes der Strangsicherung.

³ Voraussetzung für die Einhaltung der IEC 61730 Zertifizierung.

Leistungsstarke Lösungen für PV-Systeme

Technische Merkmale:

- Hohe Energieerträge unter verschiedensten klimatischen Bedingungen, ausgezeichnetes Schwachlichtverhalten, hervorragender Temperaturkoeffizient.
- Nachweisliche Lieferung des vorausgerechneten Energieertrags mit hohem Systemwirkungsgrad (PR).
- Rahmenlose Solarmodule sind robust, kostengünstig und recycelbar. Sie benötigen keine Erdung.
- Fertigung in modernen, hochautomatisierten, nach ISO9001:2000 (Qualität) und ISO14001:2004 (Umweltmanagement) zertifizierten Anlagen.
- Von international führenden Instituten getestet und für Zuverlässigkeit und Sicherheit zertifiziert:
 - Schutzklasse II @1000V
 - CE-Kennzeichnung
 - Zertifiziert nach IEC 61646
 - Zertifiziert nach IEC 61730

© Copyright 2009, First Solar, Inc.



www.firstsolar.com

First Solar PV-Module der Serie FS 2; PD-5-401-02 DE JAN 2009

FIGURE B.2: Data sheet: First Solar CdTe modules, page 2

Energie, die ankommt.



GeneCIS-Solarmodul 70W

WSG0036E070

MERKMALE

- GeneCIS-Solarmodul für serielle Verschaltung
- Optimale Energieerträge durch hervorragendes Temperatur- und Schwachlichtverhalten
- Bestechende Ästhetik durch homogen schwarze Oberfläche
- Hoher Schutz vor Umwelteinflüssen durch Glas-Glas-Aufbau
- Schwarz eloxierter Aluminiumrahmen
- Leistungszusage auf 20 Jahre
- Made in Germany (Würth Solar)

TECHNISCHE DATEN

Elektrische Daten bei STC	
Nennleistung nach STC	70 W
MPP-Spannung (Umpp)	33 V
MPP-Strom (Impp)	2,12 A
Leerlaufspannung (Uoc)	42,3 V
Kurzschlussstrom (Isc)	2,4 A

Elektrische Daten bei NOCT	
NOCT	47 (+/-3)

Systemdaten	
Max Systemspannung	1.000 V
Leistungstoleranz (Pmax)	-2 / +5 %
Rückstromfestigkeit	3 x Isc
SysUoc, Leerlaufspannung (Uoc) bei -10°C	46,6 V
MPP-Spannung (Umpp) bei +70°C	27,8 V
Temperatur-Koeffizient (Pmpp)	-0,36 % / °C
Temperatur-Koeffizient (Uoc)	-0,29 % / °C
Temperatur-Koeffizient (Isc)	0,05 % / °C
Zellmaterial	CIS
Zelltechnologie	CIS
Mechanischer Aufbau	Glas-Glas-Modul mit schwarz eloxiertem Aluminiumrahmen
Frontabdeckung	Weißglas
Rahmung	Aluminiumrahmen mit Innennut
Rahmenhöhe	35 mm
Max. Verwindung	1,2 °
Max. Flächendruck	2.400 N/m ²
DC-Anschluss	MC4-Steckverbindung
Zulässige Modultemperatur	-40 ... +85 °C
Gewicht	12,71 kg
Abmessungen (B x H x T)	605 x 1.205 x 35 mm

Elektrische Daten bei Standardtestbedingungen (STC): I=1000W/m², AM 1,5, T_u=25°C
 Zellen Betriebstemperatur (NOCT): I=800W/m², T_u=20°C, V_w=1m/s



Würth Solar GmbH & Co. KG
 Alfred-Leikam-Straße 25 · D-74523 Schwäbisch Hall
 Tel. +49 (0) 791 946 00-0 · Fax +49 (0) 791 946 00-119
 wuerth-solar@we-online.de · www.wuerth-solar.de

FIGURE B.3: Data sheet: Würth Solar GeneCIS CIGS modules

SCHOTT ASI™ Dünnschicht-Solarmodul

SCHOTT ASI™ 95/97/100/103

Das deutsche Traditionsunternehmen SCHOTT Solar agiert weltweit mit mehr als 50 Jahren Erfahrung in der Entwicklung und im Bau von Komponenten für die Solarindustrie.

Die ASI® Dünnschicht-Technologie ist das Ergebnis langjähriger Erfahrung und hochmoderner Fertigungsstandards. Dünnschichtsolarmodule mit ASI® Zelltechnologie garantieren dauerhaft hohe Leistung und überdurchschnittliche Energieerträge über Jahre.

Hoher Ertrag: Die Gewährung besonders hoher Erträge bei diffusem Licht, schlecht hinterlüfteten und warmen Standorten, teilverschatteter und weniger gut ausgerichteter Dächer zeichnen das ASI® Dünnschichtmodul von SCHOTT Solar aus.

Einfache und kostengünstige Verschaltung: Bypass-Dioden sind in den elektrischen Anschlussdosen integriert. Die 17-Volt-Modulspannung des Niederspannungsmoduls und die auf max. 1000 Volt ausgelegte Systemspannung stellen die schnelle, einfache und kostengünstige Verschaltung der Module sicher.

Doppelte Qualitätsstandards: Der SCHOTT Solar interne Qualitätsstandard entspricht der doppelten von der IEC-Norm geforderten Prüfdauer.

Höchste Leistungstreue: Die ausgelieferten SCHOTT Solar Module verfügen ausschließlich über eine Plusoleranz in der Nennleistung. Dies gewährleistet dauerhaft hohe Energieerträge.

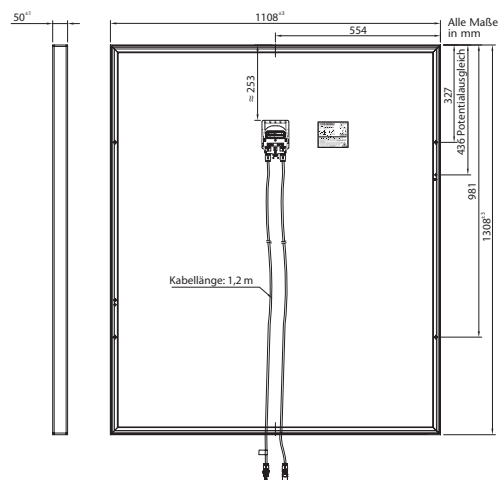
Langjährige Verlässlichkeit „Made in Germany“: Betreiber einer Anlage von SCHOTT Solar erhalten eine langfristige Leistungsgarantie von 25 Jahren und eine Gewährleistung von fünf Jahren.

Langzeitstabile Verkapselung: Das ASI® Dünnschichtmodul mit der bewährten ASI® Verkapselung verfügt über eine herausragende UV-, Temperatur- und Witterungsbeständigkeit unter extremen Bedingungen.

- Hoher Ertrag
- Einfache und kostengünstige Verschaltung
- Doppelte Qualitätsstandards
- Höchste Leistungstreue
- Langjährige Verlässlichkeit „Made in Germany“
- Langzeitstabile Verkapselung



SCHOTT ASI™ 95/97/100/103



SCHOTT
solar

FIGURE B.4: Data sheet: Schott a-Si modules, page 1

Technische Daten

Elektrische Moduldaten

Die elektrischen Daten gelten bei Standard-Test-Bedingungen (STC):
Einstrahlung in Modulebene 1000 W/m² mit Spektrum AM 1,5 bei einer Zelltemperatur von 25°C

Produktname	SCHOTT ASI™ 95		SCHOTT ASI™ 97		SCHOTT ASI™ 100		SCHOTT ASI™ 103	
	stabiler Wert	Anfangswert	stabiler Wert	Anfangswert	stabiler Wert	Anfangswert	stabiler Wert	Anfangswert
Nennleistung [Wp]	$P_{mpp} \geq 95$	116	≥ 97	118	≥ 100	122	≥ 103	126
Nennspannung [V]	U_{mpp}	17,4	19,3	17,4	19,3	17,5	19,4	19,5
Nennstrom [A]	I_{mpp}	5,47	6,00	5,57	6,10	5,71	6,30	5,86
Leerlaufspannung [V]	U_{oc}	23,6	24,6	23,7	24,7	23,8	24,8	23,9
Kurzschluss-Strom [A]	I_{sc}	6,69	6,90	6,72	6,90	6,79	7,00	6,91
Modulwirkungsgrad (%)	η	6,6		6,7		6,9		7,1

Sortierung der Moduleistung nach Flasherdaten (-0 %, reine Plus toleranz)
Die Messtoleranz der Nennleistung beträgt ± 5 %, die der übrigen Einzelwerte ± 10 %.

Zellen-Nennbetriebstemperatur (NOCT)

Typische Daten unter Einstrahlung in Modulebene 800 W/m² mit Spektrum AM 1,5, Windgeschwindigkeit 1 m/s, Umgebungstemperatur 20°C

Nennleistung [Wp]	P_{mpp}	75	77	79	82
Nennspannung [V]	U_{mpp}	17,2	17,2	17,3	17,4
Leerlaufspannung [V]	U_{oc}	23,3	23,4	23,5	23,6
Kurzschluss-Strom [A]	I_{sc}	5,35	5,37	5,43	5,48
Temperatur [°C]	T_{NOCT}	49	49	49	49

Die Messtoleranz der Nennleistung beträgt ± 5 %, die der übrigen Einzelwerte ± 10 %.

Daten bei geringer Strahlungsintensität

Einstrahlung in Modulebene 200 W/m² mit Spektrum AM 1,5, Zelltemperatur 25°C

Nennleistung [Wp]	P_{mpp}	19,0	19,4	20,0	20,6
Nennspannung [V]	U_{mpp}	17,4	17,4	17,6	17,6
Nennstrom [A]	I_{mpp}	1,09	1,11	1,14	1,17
Leerlaufspannung [V]	U_{oc}	21,2	21,3	21,4	21,5
Kurzschluss-Strom [A]	I_{sc}	1,27	1,28	1,29	1,31
Modulwirkungsgrad (%)	η	6,6	6,7	6,9	7,1

Die Messtoleranz beträgt ± 10 %.

Temperaturkoeffizienten

Leistung [%/K]	$T_K (P_n)$	-0,20	-0,20	-0,20	-0,20
Spannung [%/K]	$T_K (U)$	-0,33	-0,33	-0,33	-0,33
Leerlaufspannung [mV/K]	$T_K (U_{oc})$	-78	-78	-79	-79
Strom [%/K]	$T_K (I)$	0,08	0,08	0,08	0,08

Die Toleranz der Angaben beträgt ± 10 %.

Kenndaten

Solarzellen pro Modul	56
Solarzellentyp	a-Si/a-Si Tandemzelle
Anschluss	Anschlussdose IP65 mit einer Bypassdiode, 4 mm ² Solarkabel mit Tyco-Steckverbindern, Länge je Pol: 1,2 m
Maße Anschlussdose [mm]	138 x 90 x 22
Frontabdeckung	wärmebehandeltes Floatglas 4 mm
Rahmenmaterial	Aluminium - schwarz

Abmessungen und Gewicht

Abmessungen [mm]	1.108 x 1.308 (Toleranzen ± 3 mm)
Dicke [mm]	50 (Toleranzen ± 1 mm)
Gewicht [kg]	18

Grenzwerte

Max. zulässige Spannung [V _{oc}]	1000
Max. Rückstrom I_R [A]*	15
Zulässige Modultemperatur [°C]	-40... +85
Max. Belastung (nach IEC 61646 ed. 2)	Druck: 2.400 N/m ² oder 245 kg/m ² Sog: 2.400 N/m ² oder 245 kg/m ²
Anwendungs klasse (nach IEC 61730)	A
Brandklasse (nach IEC 61730)	C

* Keine externe Spannung größer als U_{oc} auf das Modul aufprägen.

Zulassung und Zertifikate

Die Module sind zertifiziert und zugelassen nach IEC 61646 ed. 2 und IEC 61730, der elektrischen Schutzklasse II sowie den CE-Richtlinien.



Hinweise zu Installation und Bedienung dieses Produkts finden Sie in der **Installationsanleitung**.

Alle Angaben entsprechen der EN 50380-Norm.

SCHOTT Solar AG
Carl-Zeiss-Straße 4
63755 Alzenau
Germany

Tel.: +49 (0)60 23 / 91 - 1712
Fax: +49 (0)60 23 / 91 - 1700
solar.sales@schottsolar.com
www.schottsolar.com

SCHOTT
solar

FIGURE B.5: Data sheet: Schott a-Si modules, page 2

Appendix C

List of Publications

- [I] S. Novalin, M. Rennhofer, J. Summhammer, R. Leidl, S. Zamini. Pre-Treatment Verhalten von Dünnschicht PV-Modulen. *Proceedings 26. Symposium Photovoltaische Solarenergie*, pages 569-574, Bad Staffelstein, Mar. 2011. ISBN: 978-3-934681-51-9
- [II] S. Novalin, M. Rennhofer, J. Summhammer, R. Leidl, S. Zamini. Metastabilities in thin-film modules due to pre-treatment. *Proceedings of the 26th European Photovoltaic Solar Energy Conference*, pages 3473 - 3475, Hamburg, Sept. 2011. doi: 10.4229/26thEUPVSEC2011-4AV.1.56
- [III] S. Novalin, M. Rennhofer, J. Summhammer. Electrical metastabilities in chalcogenide photovoltaic devices. *Thin Solid Films*, 535:261-264, 2013. doi: 10.1016/j.tsf.2012.10.041
- [IV] R. Ebner, B. Kubicek, G. Újvári, S. Novalin, M. Rennhofer, M. Halwachs. Optical Characterization of Different Thin Film Module Technologies. *International Journal of Photoenergy*, 2015:159458, 2015. doi: 10.1155/2015/159458



Die approbierte gedruckte Originalversion dieser Dissertation ist an der TU Wien Bibliothek verfügbar.
The approved original version of this doctoral thesis is available in print at TU Wien Bibliothek.

Bibliography

- [1] B. Burger, K. Kiefer, C. Kost, S. Nold, S. Philipps, R. Preu, R. Schindler, T. Schlegl, G. Stryi-Hipp, G. Willeke, H. Wirth, I. Brucker, A. Häberle, V. Schacht, and W. Warmuth. Photovoltaics Report. Technical report, Fraunhofer Institute for Solar Energy Systems ISE, Freiburg, 2019. URL <http://www.ise.fraunhofer.de/de/downloads/pdf-files/aktuelles/photovoltaics-report-in-englischer-sprache.pdf>. Date accessed 2020-05-10.
- [2] J. Carbone. Expect Silicon Wafer Tags to Rise Through 2019, 2018. URL <https://www.sourcetoday.com/supply-chain/expect-silicon-wafer-tags-rise-through-2019>. Date accessed 2019-04-04.
- [3] NREL. Best Research-Cell Efficiencies, 2020. URL <https://www.nrel.gov/pv/assets/pdfs/best-research-cell-efficiencies.20200406.pdf>. Date accessed 2020-05-02.
- [4] NREL. Champion Module Efficiencies, 2019. URL <https://www.nrel.gov/pv/assets/pdfs/champion-module-efficiencies.20191104.pdf>. Date accessed 2020-05-02.
- [5] A. Luque and S. Hegedus, editors. *Handbook of Photovoltaic Science and Engineering*. John Wiley & Sons Ltd, West Sussex, 2003. ISBN 0471491969.
- [6] R.L. Anderson. Experiments on Ge-GaAs heterojunctions. *Solid-State Electronics*, 5:341–351, 1962.
- [7] G.A. Somorjai and Y. Li. *Introduction to Surface Chemistry and Catalysis*. John Wiley & Sons, Inc., Hoboken, New Jersey, 2nd edition, 2010.
- [8] M.A. Green. *Solar Cells: Operating Principles, Technology and System Applications*. The University of New South Wales, Rosebery, 1992.
- [9] N.W. Ashcroft and N.D. Mermin. *Solid state physics*. Holt, Rinehart and Winston, New York, 1976.

- [10] S.S. Hegedus and W.N. Shafarman. Thin-film solar cells: device measurements and analysis. *Progress in Photovoltaics: Research and Applications*, 12:155–176, mar 2004. ISSN 1062-7995. doi: 10.1002/pip.518.
- [11] J. Nelson. *The Physics of Solar Cells*. Imperial College Press, London, 2003. ISBN 9781860943492.
- [12] R. Scheer and H.-W. Schock. *Chalcogenide Photovoltaics: Physics, Technologies, and Thin Film Devices*. Wiley-VHC Verlag & Co. KGaA, Weinheim, 2011. ISBN 978-3-527-31459-1.
- [13] NREL. Best Research-Cell Efficiencies, 2014. URL http://www.nrel.gov/ncpv/images/efficiency_chart.jpg. Date accessed 2020-05-10.
- [14] U. Rau and H.-W. Schock. Cu(In, Ga)Se₂ Solar Cells. In Mary D Archer and Robert Hill, editors, *Clean Electricity from Photovoltaics*, chapter 7. Imperial College Press, London, 1 edition, 2001. ISBN 9781848161504 1848161506.
- [15] J.L. Shay, S. Wagner, and H.M. Kasper. Efficient CuInSe₂/CdS solar cells. *Applied Physics Letters*, 27(2):89, 1975. ISSN 00036951. doi: 10.1063/1.88372.
- [16] P. Jackson, D. Hariskos, R. Wuerz, W. Wischmann, and M. Powalla. Compositional investigation of potassium doped Cu(In,Ga)Se₂ solar cells with efficiencies up to 20.8%. *physica status solidi (RRL) - Rapid Research Letters*, 8:219–222, 2014. ISSN 18626254. doi: 10.1002/pssr.201409040.
- [17] A. Chirilă, P. Reinhard, F. Pianezzi, P. Bloesch, A.R. Uhl, C. Fella, L. Kranz, D. Keller, C. Gretener, H. Hagendorfer, D. Jaeger, R. Erni, S. Nishiwaki, S. Buecheler, and A.N. Tiwari. Potassium-induced surface modification of Cu(In,Ga)Se₂ thin films for high-efficiency solar cells. *Nature materials*, 12(12): 1107–11, dec 2013. ISSN 1476-1122. doi: 10.1038/nmat3789.
- [18] Solar Frontier. Solar Frontier Sets Thin-Film PV World Record with 20.9% CIS Cell, 2014. URL <http://www.solar-frontier.com/eng/news/2014/C031367.html>. Date accessed 2020-05-10.
- [19] S. Mehta. Global 2013 PV Module Production Hits 39.8GW; Yingli is the Shipment Leader, 2014. URL <http://www.greentechmedia.com/articles/read/Global-2013-PV-Module-Production-Hits-39-8-GW-Yingli-Leads-in-Production-a>. Date accessed 2020-05-10.
- [20] Public. Chalcopyrite unit cell 3D balls, 2007. URL http://en.wikipedia.org/wiki/Copper_indium_gallium_selenide_solar_cells#mediaviewer/File:Chalcopyrite-unit-cell-3D-balls.png. Date accessed 2020-05-10.

- [21] W.N. Shafarman and L. Stolt. Cu(In,Ga)Se₂ Solar Cells. In Antonio Luque and Steven Hegedus, editors, *Handbook of Photovoltaic Science and Engineering*, chapter 13. John Wiley & Sons Ltd, West Sussex, 2003. ISBN 0-471-49196-9.
- [22] S. Niki, M. Contreras, I. Repins, M. Powalla, K. Kushiya, S. Ishizuka, and K. Matsubara. CIGS absorbers and processes. *Progress in Photovoltaics: Research and Applications*, 18(6):453–466, sep 2010. ISSN 10627995. doi: 10.1002/pip.969.
- [23] M.A. Contreras, B. Egaas, P. Dippo, J. Webb, J.E. Granata, K. Ramanathan, S. Asher, A. Swartzlander, and R. Noufi. On the role of Na and modifications to Cu(In,Ga)Se₂ absorber materials using thin-MF (M=Na, K, Cs) precursor layers. In *Proceedings of the 26th IEEE Photovoltaic Specialists Conference*, pages 359–362, Anaheim, CA, 1997.
- [24] D.W. Niles, K. Ramanathan, F.S. Hasoon, and R. Noufi. Na impurity chemistry in photovoltaic CIGS thin films: Investigation with x-ray photoelectron spectroscopy. *Journal of vacuum science and Technology A*, 15:3044–3049, 1997.
- [25] L. Kronik, D. Cahen, and H.-W. Schock. Effects of sodium on polycrystalline Cu(In,Ga)Se₂ and its solar cell performance. *Advanced Materials*, 10:31–36, 1998.
- [26] A. Hultqvist. *Cadmium Free Buffer Layers and the Influence of their Material Properties on the Performance of Cu(In,Ga)Se₂ Solar Cells*. PhD thesis, Uppsala University, 2010.
- [27] N. Naghavi, D. Abou-Ras, N. Allsop, N. Barreau, S. Bücheler, A. Ennaoui, C.-H. Fischer, C. Guillen, D. Hariskos, J. Herrero, R. Klenk, K. Kushiya, D. Lincot, R. Menner, T. Nakada, C. Platzer-Björkman, S. Spiering, A.N. Tiwari, and T. Törndahl. Buffer layers and transparent conducting oxides for chalcopyrite Cu(In,Ga)(S,Se)₂ based thin film photovoltaics: present status and current developments. *Progress in Photovoltaics: Research and Applications*, 18(6):411–433, sep 2010. ISSN 10627995. doi: 10.1002/pip.955.
- [28] R. Klenk. Characterisation and modelling of chalcopyrite solar cells. *Thin Solid Films*, 387(1-2):135–140, may 2001. ISSN 00406090. doi: 10.1016/S0040-6090(00)01736-3.
- [29] A. Niemegeers, M. Burgelman, and A. De Vos. On the CdS/CuInSe₂ conduction band discontinuity. *Applied Physics Letters*, 67(6):843, 1995. ISSN 00036951. doi: 10.1063/1.115523.
- [30] A. Niemegeers, M. Burgelman, R. Herberholz, U. Rau, D. Hariskos, and H.-W. Schock. Model for electronic transport in Cu(In, Ga)Se₂ solar cells. *Progress in Photovoltaics: Research and Applications*, 6:407–421, 1998.

- [31] S. Siebentritt, M. Igalson, C. Persson, and S. Lany. The electronic structure of chalcopyrites - bands, point defects and grain boundaries. *Progress in Photovoltaics: Research and Applications*, 18(6):390–410, sep 2010. ISSN 10627995. doi: 10.1002/pip.936.
- [32] S.B. Zhang, S.-H. Wei, and A. Zunger. Stabilization of Ternary Compounds via Ordered Arrays of Defect Pairs. *Physical Review Letters*, 78(21):4059–4062, may 1997. ISSN 0031-9007. doi: 10.1103/PhysRevLett.78.4059.
- [33] T. Eisenbarth, R. Caballero, M. Nichterwitz, C.A. Kaufmann, H.-W. Schock, and T. Unold. Characterization of metastabilities in Cu(In,Ga)Se₂ thin-film solar cells by capacitance and current-voltage spectroscopy. *Journal of Applied Physics*, 110(9):094506, 2011. ISSN 00218979. doi: 10.1063/1.3656453.
- [34] M.N. Ruberto and A. Rothwarf. Time-depenent open-circuit voltage in CuInSe₂/CdS solar cells: Theory and experiment. *Journal of Applied Physics*, 61(9):4662, 1987.
- [35] R.A. Sasala and J.R. Sites. Time dependent voltage in CuInSe₂ and CdTe solar cells. In M L Timmons, editor, *Proc. 23rd IEEE Photovoltaic Specialists Conference*, number 1, pages 543–548, New York, 1993. IEEE. ISBN 0780312201.
- [36] F. Engelhardt, M. Schmidt, T. Meyer, O. Seifert, J. Parisi, and U. Rau. Metastable electrical transport in Cu(In, Ga)Se₂ thin films and ZnO/CdS/Cu(In, Ga)Se₂ heterostructures. *Physics Letters A*, 245:489, 1998.
- [37] M. Igalson and H.-W. Schock. The metastable changes of the trap spectra of CuInSe₂-based photovoltaic devices. *Journal of Applied Physics*, 80(10):5765, 1996.
- [38] R. Herberholz, U. Rau, H.-W. Schock, T. Haalboom, T. Godecke, F. Ernst, C. Beilharz, K.W. Benz, and D. Cahen. Phase segregation, Cu migration and junction formation in Cu(In, Ga)Se₂. *European Physical Journal, Applied Physics*, 6:131–139, 1999. ISSN 1286-0042. doi: 10.1051/epjap:1999162.
- [39] J.T. Heath, J.D. Cohen, and W.N. Shafarman. Distinguishing metastable changes in bulk CIGS defect densities from interface effects. *Thin Solid Films*, 431-432(03):426–430, may 2003. ISSN 00406090. doi: 10.1016/S0040-6090(03)00189-5.
- [40] U. Rau, M. Schmitt, J. Parisi, W. Riedl, and F. Karg. Persistent photoconductivity in Cu(In,Ga)Se₂ heterojunctions and thin films prepared by sequential deposition. *Applied Physics Letters*, 73(2):223, 1998. ISSN 00036951. doi: 10.1063/1.121762.

- [41] T. Meyer, F. Engelhardt, J. Parisi, and U. Rau. Spectral dependence and Hall effect of persistent photoconductivity in polycrystalline Cu(In,Ga)Se₂ thin films. *Journal of Applied Physics*, 91(8):5093, 2002. ISSN 00218979. doi: 10.1063/1.1459597.
- [42] I.L. Eisgruber, J.E. Granata, J.R. Sites, J. Hou, and J. Kessler. Blue-photon modification of nonstandard diode barrier in CuInSe₂ solar cells. *Solar Energy Materials and Solar Cells*, 53:367–377, 1998.
- [43] M. Igalson and C. Platzer-Björkman. The influence of buffer layer on the transient behavior of thin film chalcopyrite devices. *Solar Energy Materials and Solar Cells*, 84(1-4):93–103, oct 2004. ISSN 09270248. doi: 10.1016/j.solmat.2004.02.038.
- [44] U. Rau, K. Weinert, Q. Nguyen, M. Mamor, G. Hanna, A. Jasenek, and H.-W. Schock. Device analysis of Cu(In,Ga)Se₂ heterojunction solar cells-some open questions. In *Symposium H – II-IV Compound Semiconductor Photovoltaic Materials, MRS Proceedings*, page 668, 2001. doi: 10.1557/PROC-668-H9.1.
- [45] M. Igalson, A. Kubiacyk, and P. Zabierowski. Deep centers and fill factor losses in the CIGS devices. In *II - VI Compound Semiconductor Photovoltaic Materials, Materials Research Society Symposium*, pages H921–H926, San Francisco, CA, 2001.
- [46] T. Meyer, M. Schmidt, F. Engelhardt, J. Parisi, and U. Rau. A model for the open circuit voltage relaxation in Cu(In,Ga)Se₂ heterojunction solar cells. *European Physical Journal, Applied Physics*, 8(1):43–52, 1999.
- [47] M. Igalson, M. Cwil, and M. Edoff. Metastabilities in the electrical characteristics of CIGS devices: Experimental results vs theoretical predictions. *Thin Solid Films*, 515(15):6142–6146, may 2007. ISSN 00406090. doi: 10.1016/j.tsf.2006.12.038.
- [48] V. Nadazdy, M. Yakushev, E.H. Djebbar, A.E. Hill, and R.D. Tomlinson. Switching of deep levels in CuInSe₂ due to electric field-induced Cu ion migration. *Journal of Applied Physics*, 84(8):4322, 1998. ISSN 00218979. doi: 10.1063/1.368651.
- [49] M. Igalson, M. Cwil, and M. Edoff. Persistent capture and release of electrons in CIGS solar cells. In W. Palz, H. Ossenbrink, and P. Helm, editors, *Proceedings of the 20th European Photovoltaic Solar Energy Conference*, page 1800, Barcelona, 2005. WIP.
- [50] M. Igalson, M. Bodegard, L. Stolt, and A. Jasenek. The ‘defected layer’ and the mechanism of the interface-related metastable behavior in the ZnO/CdS/Cu(In, Ga)Se₂ devices. *Thin Solid Films*, 431-432:153–157, 2003.

- [51] P. Zabierowski, U. Rau, and M. Igalson. Classification of metastabilities in the electrical characteristics of ZnO/CdS/Cu(In, Ga)Se₂ solar cells. *Thin Solid Films*, 387:147–150, 2001.
- [52] U. Rau, A. Jasenek, R. Herberholz, H.-W. Schock, J.-F. Guillemoles, D. Lincot, and L. Kronik. The inherent stability of Cu(In,Ga)Se₂-based solar cells. In J. Schmid, editor, *Proceedings of the 2nd World Conference on Photovoltaic Energy Conversion*, number July, pages 428–433, Vienna, 1998.
- [53] M. Igalson, M. Bodegård, and L. Stolt. Reversible changes of the fill factor in the ZnO/CdS/Cu(In,Ga)Se₂ solar cells. *Solar Energy Materials and Solar Cells*, 80(2):195–207, oct 2003. ISSN 09270248. doi: 10.1016/j.solmat.2003.06.006.
- [54] C. Deline, A. Stokes, T.J. Silverman, S. Rummel, D. Jordan, and S. Kurtz. Electrical bias as an alternate method for reproducible measurement of copper indium gallium diselenide (CIGS) photovoltaic modules. In Neelkanth G. Dhere and John H. Wohlgemuth, editors, *Proc. of SPIE Optics and Photonics 2012*, pages CP–5200–56078, San Diego, 2012.
- [55] R. Kniese, M. Powalla, and U. Rau. Characterization of the CdS/Cu(In,Ga)Se₂ interface by electron beam induced currents. *Thin Solid Films*, 515(15):6163–6167, may 2007. ISSN 00406090. doi: 10.1016/j.tsf.2006.12.045.
- [56] D.V. Lang and R.A. Logan. Large-Lattice-Relaxation Model for Persistent Photoconductivity in Compound Semiconductors. *Physical Review Letters*, 39(10):635, 1977.
- [57] S. Lany and A. Zunger. Intrinsic DX Centers in Ternary Chalcopyrite Semiconductors. *Physical Review Letters*, 100(1):016401, jan 2008. ISSN 0031-9007. doi: 10.1103/PhysRevLett.100.016401.
- [58] Y.-J. Zhao, C. Persson, S. Lany, and A. Zunger. Why can CuInSe₂ be readily equilibrium-doped n-type but the wider-gap CuGaSe₂ cannot? *Applied Physics Letters*, 85(24):5860, 2004. ISSN 00036951. doi: 10.1063/1.1830074.
- [59] A. Klein and W. Jaegermann. Fermi-level-dependent defect formation in Cu-chalcopyrite semiconductors. *Applied Physics Letters*, 74(16):2283, 1999. ISSN 00036951. doi: 10.1063/1.123825.
- [60] J.-F. Guillemoles, L. Kronik, D. Cahen, U. Rau, A. Jasenek, and H.-W. Schock. Stability Issues of Cu(In, Ga)Se₂-Based Solar Cells. *J. Phys. Chem. B*, 104:4849–4862, 2000.

- [61] M. Burgelman, F. Engelhardt, J.-F. Guillemoles, R. Herberholz, M. Igalson, R. Klenk, M. Lampert, T. Meyer, V. Nadenau, A. Niemegeers, J. Parisi, U. Rau, H.-W. Schock, M. Schmitt, O. Seifert, T. Walter, and S. Zott. Defects in Cu(In, Ga)Se₂ Semiconductors and their Role in the Device Performance of Thin-film Solar Cells. *Progress in Photovoltaics: Research and Applications*, 5(1997):121, 1997.
- [62] A.O. Pudov, J.R. Sites, M.A. Contreras, T. Nakada, and H.-W. Schock. CIGS J-V distortion in the absence of blue photons. *Thin Solid Films*, 480-481:273–278, jun 2005. ISSN 00406090. doi: 10.1016/j.tsf.2004.11.099.
- [63] A.O. Pudov, A. Kanevce, H.A. Al-Thani, J.R. Sites, and F.S. Hasoon. Secondary barriers in CdS-CuIn_{1-x}Ga_xSe₂ solar cells. *Journal of Applied Physics*, 97(6): 064901, 2005. ISSN 00218979. doi: 10.1063/1.1850604.
- [64] R. Herberholz, M. Igalson, and H.-W. Schock. Distinction between bulk and interface states in CuInSe₂/CdS/ZnO by space charge spectroscopy. *Journal of Applied Physics*, 83(1):318, 1998. ISSN 00218979. doi: 10.1063/1.366686.
- [65] T. Eisenbarth. *Identifikation von Defekten und Metastabilitäten in Cu(In,Ga)Se₂-Dünnschichtsolarzellen*. Dissertation, Freie Universität Berlin, 2010.
- [66] S. Lany and A. Zunger. Light- and bias-induced metastabilities in Cu(In,Ga)Se₂ based solar cells caused by the (V[Se]-V[Cu]) vacancy complex. *Journal of Applied Physics*, 100(11):113725, 2006. ISSN 00218979. doi: 10.1063/1.2388256.
- [67] S. Lany and A. Zunger. Anion vacancies as a source of persistent photoconductivity in II-VI and chalcopyrite semiconductors. *Physical Review B*, 72(3):035215, jul 2005. ISSN 1098-0121. doi: 10.1103/PhysRevB.72.035215.
- [68] D.A. Cusano. CdTe solar cells and photovoltaic heterojunctions in II-VI compounds. *Solid State Electronics*, 6:217–232, 1963.
- [69] E.L. Lane. *Clean tech intellectual property : eco-marks, green patents and green innovation*. Oxford University Press USA, 2011. ISBN 9780199737093.
- [70] D. Bonnet. Cadmium Telluride Solar Cells. In Mary D Archer and Robert Hill, editors, *Clean Electricity from Photovoltaics*, chapter 6. Imperial College Press, London, 1 edition, 2001. ISBN 9781848161504 1848161506.
- [71] A. Romeo, G. Khrypunov, F. Kurdesau, M. Arnold, D. L. Bätzner, H. Zogg, and A. N. Tiwari. High-efficiency flexible CdTe solar cells on polymer substrates. *Solar Energy Materials and Solar Cells*, 90(18-19):3407–3415, nov 2006. ISSN 09270248. doi: 10.1016/j.solmat.2005.09.020.

- [72] C.S. Ferekides, U. Balasubramanian, R. Mamazza, V. Viswanathan, H. Zhao, and D.L. Morel. CdTe thin film solar cells: device and technology issues. *Solar Energy*, 77(6):823–830, dec 2004. ISSN 0038092X. doi: 10.1016/j.solener.2004.05.023.
- [73] C.S. Ferekides, R. Mamazza, U. Balasubramanian, and D.L. Morel. Transparent conductors and buffer layers for CdTe solar cells. *Thin Solid Films*, 480-481:224–229, jun 2005. ISSN 00406090. doi: 10.1016/j.tsf.2004.11.094.
- [74] First Solar Achieves Yet Another Cell Conversion Efficiency World Record, 2016. URL <https://investor.firstsolar.com/news/press-release-details/2016/First-Solar-Achieves-Yet-Another-Cell-Conversion-Efficiency-World-Record/default.aspx>. Date accessed 2020-05-10.
- [75] B.E. McCandless, L.V. Moulton, and R.W. Birkmire. Recrystallization and sulfur diffusion in CdCl₂-treated CdTe/CdS thin films. *Progress in Photovoltaics: Research and Applications*, (5):249–260, 1997.
- [76] K. Durose, P.R. Edwards, and S.A. Galloway. EBIC and luminescence mapping of CdTe/CdS solar cells. *Thin Solid Films*, (361-362):364–370, 2000.
- [77] J.D. Major, R.E. Treharne, L.J. Phillips, and K. Durose. A low-cost non-toxic post-growth activation step for CdTe solar cells. *Nature*, 511(7509):334–337, jun 2014. ISSN 0028-0836. doi: 10.1038/nature13435.
- [78] S.-H. Wei and S. Zhang. Chemical trends of defect formation and doping limit in II-VI semiconductors: The case of CdTe. *Physical Review B*, 66(15):155211, oct 2002. ISSN 0163-1829. doi: 10.1103/PhysRevB.66.155211.
- [79] R.A. Enzenroth, K.L. Barth, and W.S. Sampath. Correlation of stability to varied CdCl₂ treatment and related defects in CdS/CdTe PV devices as measured by thermal admittance spectroscopy. *Journal of Physics and Chemistry of Solids*, 66(11):1883–1886, nov 2005. ISSN 00223697. doi: 10.1016/j.jpcs.2005.09.022.
- [80] J. Zhou, X. Wu, Y. Yan, S. Asher, J. Da Silva, S. Wei, L. Weinhardt, M. Bar, and C. Heske. The mechanism of J-V ”roll-over” in CdS/CdTe devices. In *Materials Research Society Symposium Proceedings*, pages 491–496, 2007.
- [81] S.S. Hegedus and B.E. McCandless. CdTe contacts for CdTe/CdS solar cells: effect of Cu thickness, surface preparation and recontacting on device performance and stability. *Solar Energy Materials and Solar Cells*, 88(1):75–95, jun 2005. ISSN 09270248. doi: 10.1016/j.solmat.2004.10.010.

- [82] G. Stollwerck and J.R. Sites. Analysis of CdTe back contact barriers. In *Proceedings of the 13th European Photovoltaic Solar Energy Conference*, page 2020, 1995.
- [83] S.H. Demtsu and J.R. Sites. Effect of back-contact barrier on thin-film CdTe solar cells. *Thin Solid Films*, 510(1-2):320–324, jul 2006. ISSN 00406090. doi: 10.1016/j.tsf.2006.01.004.
- [84] D.M. Oman, K.M. Dugan, J.L. Killian, V. Ceekala, C.S. Ferekides, and D.L. Morel. Device performance characterization and junction mechanisms in CdTe/CdS solar cells. *Solar Energy Materials and Solar Cells*, 58(4):361–373, aug 1999. ISSN 09270248. doi: 10.1016/S0927-0248(99)00008-2.
- [85] M. Köntges, R. Reineke-Koch, P. Nollet, J. Beier, R. Schäffler, and J. Parisi. Light induced changes in the electrical behavior of CdTe and Cu(In,Ga)Se₂ solar cells. *Thin Solid Films*, 403/404:280–286, 2002.
- [86] G. Agostinelli, D.L. Blätzner, and M. Burgelman. An alternative model for V, G and T dependence of CdTe solar cells JV characteristics. In *Proceedings of the 29th IEEE Photovoltaics Specialist Conference*, page 744, 2002.
- [87] P. Nollet, M. Köntges, M. Burgelman, S. Degrave, and R. Reineke-Koch. Indications for presence and importance of interface states in CdTe/CdS solar cells. *Thin Solid Films*, 431-432(03):414–420, may 2003. ISSN 00406090. doi: 10.1016/S0040-6090(03)00201-3.
- [88] A. Niemegeers and M. Burgelman. Effects of the Au/CdTe back contact on IV and CV characteristics of Au/CdTe/CdS/TCO solar cells. *Journal of Applied Physics*, 81(6):2881, 1997. ISSN 00218979. doi: 10.1063/1.363946.
- [89] J.A. Del Cueto and B. Von Roedern. Long-term Transient and Metastable Effects in Cadmium Telluride Photovoltaic Modules. *Progress in Photovoltaics: Research and Applications*, 14(7):615–628, nov 2006. ISSN 1062-7995. doi: 10.1002/pip.687.
- [90] T.J. McMahon, T.J. Bernard, and D.S. Albin. Nonlinear shunt paths in thin-film CdTe solar cells. *Journal of Applied Physics*, 97(5):054503, 2005. ISSN 00218979. doi: 10.1063/1.1856216.
- [91] T.J. McMahon. Dark current transients in thin-film CdTe solar cells. In *Conference Record of the Twenty-Ninth IEEE Photovoltaic Specialists Conference*, page 768, 2002.
- [92] A. Fahrenbruch. Current transients in CdS/CdTe solar cells. In *Materials Research Society Symposium Proceedings*, page 865, 2005.

- [93] J. Heath and P. Zabierowski. Capacitance Spectroscopy of Thin-Film Solar Cells. In D. Abou-Ras, T. Kirchartz, and U. Rau, editors, *Advanced Characterization Techniques for Thin Film Solar Cells*, chapter 4. Wiley-VHC Verlag & Co. KGaA, Weinheim, 2011. ISBN 978-3-527-41003-3.
- [94] C. Ulbrich, K. Decock, J. Pohl, and D. Abou-Ras. Young Scientist Tutorial on Characterization Techniques for Thin-Film Solar Cells, 2012.
- [95] V.L. Dalal and A. Rothwarf. Comment on "A simple measurement of absolute solar cell efficiency". *Journal of Applied Physics*, 50(4):2980, 1979. ISSN 00218979. doi: 10.1063/1.326181.
- [96] X.X. Liu and J.R. Sites. Solar-cell collection efficiency and its variation with voltage. *Journal of Applied Physics*, 75(1):577, 1994. ISSN 00218979. doi: 10.1063/1.355842.
- [97] IEC. International Standard IEC 60904-1 Photovoltaic devices - Part 1: Measurement of photovoltaic current-voltage characteristics. *International Electrotechnical Commission*, 2006.
- [98] IEC. International Standard IEC 61215 Crystalline silicon terrestrial photovoltaic (PV) modules - Design qualification and type approval. *International Electrotechnical Commission*, 2005.
- [99] IEC. International Standard IEC 61646 Thin film terrestrial photovoltaic (PV) modules - Design qualification and type approval. *International Electrotechnical Commission*, 2005.
- [100] N. Cereghetti, D. Chianese, S. Rezzonico, and G. Travaglini. Behaviour of Triple Junction a-Si Modules. In *16th European Photovoltaic Solar Energy Conference and Exhibition*, Glasgow, 2000.
- [101] D.L. Staebler and C.R. Wronski. Reversible conductivity changes in discharge-produced amorphous Si. *Applied Physics Letters*, 31(4):292-294, 1977. ISSN 00036951. doi: 10.1063/1.89674.
- [102] IEC. International Standard IEC 60904-9 Photovoltaic devices - Part 9: Solar simulator performance requirements. *International Electrotechnical Commission*, 2007.
- [103] M. Gostein and L. Dunn. Light Soaking Effects on PV Modules: Overview and Literature Review. In *NREL PV Module Reliability Workshop*, Denver, 2011.

- [104] M. Gostein and L. Dunn. Light Soaking Effects on Photovoltaic Modules: Overview and Literature Review. In *Proceedings of the 37th IEEE Photovoltaic Specialists Conference*, 2011.
- [105] J.A. Del Cueto, C.A. Deline, and S. Rummel. Analysis of Alternate Methods to Obtain Stabilized Power Performance of CdTe and CIGS PV Modules. In *NREL PV Module Reliability Workshop*, Denver, 2011.
- [106] A.E. Eeles, T.R. Betts, and R. Gottschalg. Preconditioning effects on CIGS solar cells and modules based on metastabilities caused by the Se-Cu di-vacancy complex. In *28th European Photovoltaic Solar Energy Conference and Exhibition*, pages 2887–2892, Villepinte, France, 2013.
- [107] J. Lindahl, U. Zimmermann, P. Szaniawski, T. Törndahl, A. Hultqvist, P. Salome, C. Platzer-Bjoerkman, and M. Edoff. Inline Cu(In,Ga)Se₂ Co-evaporation for High-Efficiency Solar Cells and Modules. *IEEE Journal of Photovoltaics*, 3(3): 1100–1105, 2013.
- [108] J. Lindahl, J.T. Wätjen, A. Hultqvist, T. Ericson, M. Edoff, and T. Törndahl. The effect of Zn(1-x)Sn(x)O(y) buffer layer thickness in 18.0% efficient Cd-free Cu(In,Ga)Se₂ solar cells. *Progress in Photovoltaics: Research and Applications*, 2012. doi: 10.1002/pip.
- [109] A. Hultqvist, C. Platzer-Björkman, J. Pettersson, T. Törndahl, and M. Edoff. CuGaSe₂ solar cells using atomic layer deposited Zn(O,S) and (Zn,Mg)O buffer layers. *Thin Solid Films*, 517:2305–2308, 2009. doi: 10.1016/j.tsf.2008.10.109.
- [110] T. Törndahl, A. Hultqvist, C. Platzer-Björkman, and M. Edoff. Growth and characterization of ZnO-based buffer layers for CIGS solar cells. *Proceedings of SPIE*, 7603:76030D–1, 2010. doi: 10.1117/12.846351.
- [111] C. Platzer-Björkman, T. Törndahl, D. Abou-Ras, J. Malmström, J. Kessler, and L. Stolt. Zn(O,S) buffer layers by atomic layer deposition in Cu(In,Ga)Se₂ based thin film solar cells: Band alignment and sulfur gradient. *Journal of Applied Physics*, 100(4):1–9, 2006.
- [112] B. Bissig, R. Carron, L. Greuter, E. Avancini, T. Feuerer, S. Buecheler, and A.N. Tiwari. Novel back contact reflector for high efficiency and double-graded Cu(In,Ga)Se₂ thin-film solar cells. *Progress in Photovoltaics Research and Applications*, 26(May):894–900, 2018. doi: 10.1002/pip.3029.
- [113] M. Wolter, B. Bissig, P. Reinhard, S. Buecheler, and P. Jackson. Correcting for interference effects in the photoluminescence of Cu(In,Ga)Se₂ thin films. *Physica Status Solidi (C)*, 14(6):1600189, 2017. doi: 10.1002/pssc.201600189.

- [114] J.K. Larsen, S.-Y. Li, J.J. Scragg, Y. Ren, C. Hägglund, M.D. Heinemann, S. Kretzschmar, T. Unold, and C. Platzer-Björkman. Interference effects in photoluminescence spectra of CZTS and CIGS thin films. *Journal of Applied Physics*, 118(035307), 2015. doi: 10.1063/1.4926857.
- [115] R. Djemour, A. Redinger, M. Mousel, L. Gütay, and S. Siebentritt. Erratum: Multiple phases of Cu₂ZnSnSe₄ detected by room temperature photoluminescence. *Journal of Applied Physics*, 118(089902), 2015. doi: 10.1063/1.4927730.
- [116] T. Weber, H. Stolz, W. von der Osten, M. Heuken, and K. Heime. Fabry-Perot oscillations in epitaxial ZnSe layers. *Semiconductor Science and Technology*, 10(1113), 1995.
- [117] R. Ebner, B. Kubicek, G. Ujvari, S. Novalin, M. Rennhofer, and M. Halwachs. Optical characterization of different thin film module technologies. *International Journal of Photoenergy*, 2015(159458), 2015. ISSN 1687529X. doi: 10.1155/2015/159458.
- [118] A. Kolodziej. Staebler-Wronski effect in amorphous silicon and its alloys. *Opto-Electronics Review*, 12(1):21–23, 2004.
- [119] R. Biswas and B.C. Pan. Mechanisms of metastability in hydrogenated amorphous silicon. *Solar Energy Materials and Solar Cells*, 78(1-4):447–467, jul 2003. ISSN 09270248. doi: 10.1016/S0927-0248(02)00447-6.
- [120] M. Deceglie, T.J. Silverman, C. Deline, B. Marion, and S. Kurtz. Proposed CIGS stabilization and measurement procedure, National Renewable Energy Laboratory. 2013.
- [121] T.J. Silverman, U. Jahn, G. Friesen, M. Pravettoni, M. Apolloni, A. Louwen, WGJHM van Sark, M. Schweiger, G. Belluardo, J. Wagner, A. Tetzlaff, P. Ingenhoven, and D. Moser. Characterisation of Performance of Thin-film Photovoltaic Technologies. Technical report, International Energy Agency, 2014.
- [122] D. Weberndorfer. *Charakterisierung unterschiedlichster CIGS-Prototypenzellen*. Bachelorthesis, FH Joanneum, 2014.
- [123] T.J. Silverman, M.G. Deceglie, B. Marion, and S.R. Kurtz. Performance stabilization of CdTe PV modules using bias and light. *IEEE Journal of Photovoltaics*, 5(1):344–349, 2015. ISSN 21563381. doi: 10.1109/JPHOTOV.2014.2370252.
- [124] A. Urbaniak and M. Igalson. Creation and relaxation of light- and bias-induced metastabilities in Cu(In,Ga)Se₂. *Journal of Applied Physics*, 106(6):063720, 2009. ISSN 00218979. doi: 10.1063/1.3213339.

- [125] Solar Spectrum, 2018. URL <https://de.wikipedia.org/wiki/Datei:Solar-wirkungsgrad.jpg>. Date accessed 2020-05-10.